

## Chapter 1 Background

### 1.1 Introduction

Drug delivery is emerging as an important research area. At present, drug delivery technologies represent about US \$20 billion global market. Drug delivery industry is currently expanding at a rate of 15% per annum, with transdermal drug delivery expected to grow by more than 20%. Better understanding of the physicochemical properties of skin has tremendous potential in improving quality of healthcare in Australia and the whole world. Drug delivery through skin will give more efficient results in curing diseases, such as muscular pains. Examples of transdermal drug delivery products include the smoking quit patch, which are normally fixed on the upper arm of smokers and release the nicotinic drugs into the blood stream, thus, controlling the nicotine level in blood. Small molecular weight of the drugs used in these patches allows them to penetrate through skin and vascular membrane. The other examples of importance drug delivery technologies include: muscular pain-releasing patches and ointments; pore curing ointments; wrinkle erasing lotions, etc. These drug delivery technologies all include small molecules for penetrating transdermal easily. Therefore, particles especially as nanoparticles which are scaled on nanometres have a great potential to be the drug delivery vehicles. However, transdermal penetration of certain types of nanoparticles should be avoided. First all, they include nanoscale-size environmental toxins. Secondly, some nanoparticles are added to cosmetic care products to improve their properties, but intended to stay on the skin surface. One example includes sunscreen that contains either ZnO-nano or TiO<sub>2</sub>-nano, or both. Toxicity and cytotoxicity of these nanoparticles is not clear at this stage. It, therefore, warrants systemic research on transdermal penetrability of these particles of different sizes, shapes, surface coatings and charges.

Elucidation of transdermal delivery mechanisms calls for refinement of the knowledge on the structure and function of the main skin barrier, especially in the context of its permeability. Skin as the outmost layer of human body, is an anatomical barrier from pathogens and damage between the internal and external environment in bodily defence. At the same time, the skin permeability is highly selective, supporting intake of low-weight, biologically active molecules, such as peptides, used in cosmetic industry. Therefore, understanding of skin permeability and skin protection function becomes an important focus of the transdermal drug delivery research.

Optimisation of drug delivery and environmental protection enhancement strategies thus provide a strong motivation for the research. Since this problem is enormous in its scope,

advances in study of the skin permeability by using emerging optical imaging modalities in combination with novel and existing models for drug delivery vehicles and environmental toxins are reported. With advent of Fluorescence Confocal Scanning Microscopy (FCSM) and more recently Fluorescence Multiphoton Microscopy (FMM), it appears to be possible to image both endogenous and exogenous fluorophores, thus, visualising purpose-designed fluorophores/nanoparticles (exogenous fluorophores) in the three-dimensional (3D) morphological layout of skin, including live skin. Visualisation of exogenous fluorophore penetration in skin (particularly in *stratum corneum*), thus, represents an important focus of this study.

The main topics of this thesis are the following:

1. Investigation of nanoparticle transdermal penetrability, distribution in skin, and kinetics by way of direct imaging of both nanoparticles and morphological background of skin. Skin penetrability dependence on the skin biological pathway, nanoparticle size, skin type, and skin treatment will be investigated.
2. Feasibility studies of drug delivery kinetics in the major biological pathways modelled by fluorescent organic dye, using a FMM technique modality. In particular, determination of local diffusion coefficient, and, ultimately, acquisition of a diffusion coefficient map of the skin area, will provide a useful measure of the drug permeability in the skin.

FMM is an emerging optical imaging technique that has potential to address the need of simultaneous imaging of endogenous and exogenous fluorophores in skin, and hence provide information on nanoparticle and fluorescent molecule distribution in skin. The key subsystem of FMM is an ultrashort-pulse laser whose radiation is tightly focussed in a biological sample. Simultaneous absorption of two (or several) photons followed by fluorescence emission is called multiphoton fluorescence. Under typical conditions, the infrared laser excitation is filtered, so that the FMM signals in the visible spectral range result in high-contrast *en face* imaging, if the focal spot is scanned across the sample. This mechanism of FMM image formation entails the most valuable property of FMM, "optical sectioning", i.e. clearing a micron-thin image slice from the turbidity of the rest of the sample.

There are several modalities of FMM, which are incorporated into an imaging system that provide comprehensive functionality to the system. These include fluorescence lifetime imaging (FLIM) and fluorescence recovery after photobleaching (FRAP). FLIM is a powerful

tool that produces an image of the fluorescence decay rate, rather than fluorescence intensity image, as in conventional FMM. FLIM provides additional discrimination between fluorophores based on their fluorescence lifetimes. Also, such useful information-bearing processes as fluorescence quenching (as a result of fluorophore interaction with proteins, e.g. flavin fluorescence quenching in the flavoprotein (FAD) complex, and in a lipid matrix), Förster resonance energy transfer manifested by the fluorescence lifetime reduction, can be inferred and quantified using FLIM imaging modality. FRAP appeared to be instrumental for the determination of transdermal diffusion coefficients of various fluorophores. It employs a mechanism of recovery of fluorescence in a finite volume bleached by intense laser radiation. The recovery rate is governed by the fluorophore diffusion rate into the bleached volume, and hence can provide their diffusion coefficients locally.

Sub-Sections 1.2 - 1.4 are introductory to the skin structure and functions. The existing knowledge base of the drug delivery will be detailed in Sub-Section 1.5. In Sub-Section 1.6, the instruments and techniques employed in this project will be described.

## **1.2 Skin anatomy and functions**

Skin is the largest organ made up of multiple layers of epithelial tissues that guard underlying muscles and organs. As the interface with the surroundings, skin plays the most important role in protecting (the body) against pathogens. Its other main functions are insulation and temperature regulation, sensation, and synthesis of vitamin D and the protection of vitamin B foliate. Skin is composed of two major layers: epidermis and dermis with some appendages such as hair follicles and sweat ducts.

### **1.2.1 Epidermis**

Epidermis is the outermost layer of the skin. It forms the waterproof, protective wrap over the body's surface and is made up of five layers, which are *stratum corneum*, *stratum lucidum*, *stratum granulosum*, *stratum spinosum* and *stratum basale* (see Fig 1). The thickness of epidermis is smallest on eyelids which is 0.05 mm and biggest on palms and soles which is 1.5 mm.

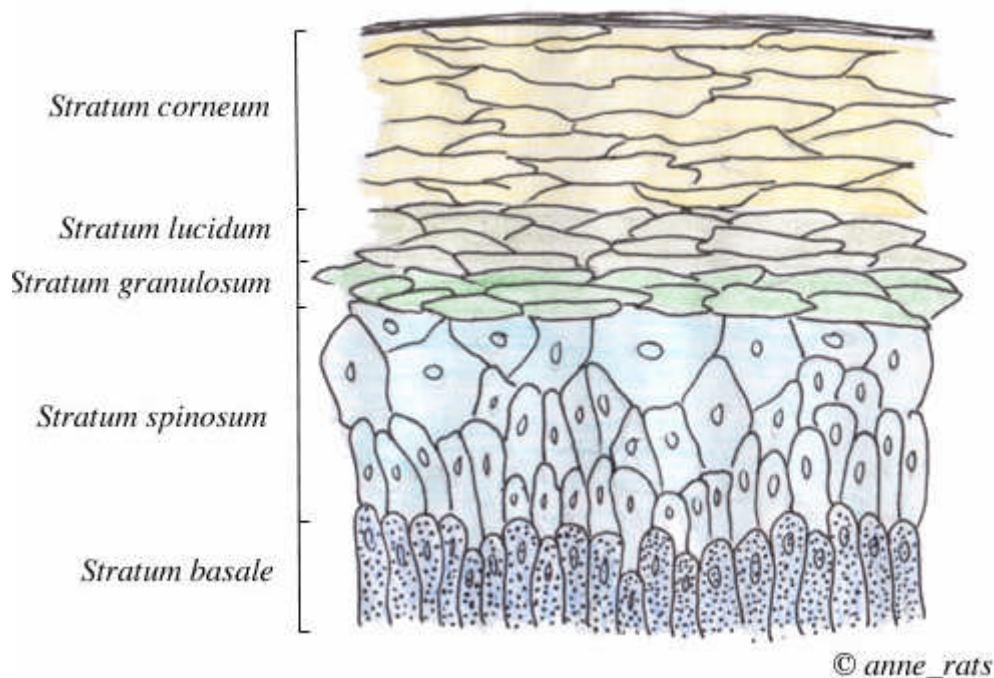


Fig 1. Epidermis Structure (<http://www.ratbehavior.org/images/Epidermis.jpg>)

The cells within epidermis are formed through mitosis at the innermost layers. They move up the strata changing shape and composition as they differentiate and become filled with keratin. They eventually reach the top layer called stratum corneum and become sloughed off, or desquamated. Stratum corneum consists of 10-15 layers of dead cells and varies in thickness from approximately 10-15  $\mu\text{m}$  in the dry state to 40  $\mu\text{m}$  when hydrated (Benson, 2005).

*Stratum corneum* is the outermost layer of the epidermis and also the outermost layer of skin. It is composed mainly of dead cells that lack nuclei but contain keratin, a protein that helps keep the skin hydrated by preventing water evaporation. It is considered as the main barrier for most drugs penetrating into deeper skin layers. The *stratum lucidum* is a thin, clear layer of dead skin cells in the epidermis such as that on the palms of the hands and the soles of the feet. The *stratum granulosum* lies between the *stratum spinosum* below and the *stratum lucidum* above. This layer typically contains 1 to 3 rows of flattened cells with many small basophilic granules in their cytoplasm. This is the highest layer in the epidermis where living cells are found. The *stratum spinosum* is a multi-layered arrangement of cuboidal cells that sits beneath the *stratum granulosum*. Adjacent cells are joined by desmosomes giving them the spiny appearance from which their name is derived. Their nuclei are often darkened, which is an early sign of cell death. Cells of the *stratum spinosum* actively synthesize intermediate filaments called cytokeratins which are composed of keratin. These intermediate filaments are anchored to the desmosomes joining adjacent cells to provide structural support,

helping the skin resist abrasion. The *stratum basale* is the layer of keratinocytes that lies at the base of the epidermis immediately above the dermis. It consists of a single layer of tall, simple columnar epithelial cells lying on a basement membrane. These cells undergo rapid cell division, mitosis to replenish the regular loss of skin by shedding from the surface. About 25% of the cells are melanocytes, which produce melanin which provides pigmentation for skin and hair.

### 1.2.2 Dermis

Dermis (see Fig 2) is the layer of skin beneath the epidermis that consists of connective tissue and cushions the body from stress and strain. The thickness of this layer is ranged from 0.3 mm on eyelids to 3.0 mm on the back. The dermis is tightly connected to the epidermis by a basement membrane. It also harbours many nerve endings that provide the sense of touch and heat. It contains hair follicles, sweat glands, sebaceous glands, apocrine glands and blood vessels. The blood vessels in the dermis provide nourishment and waste removal to its own cells as well as the *stratum basale* of the epidermis.

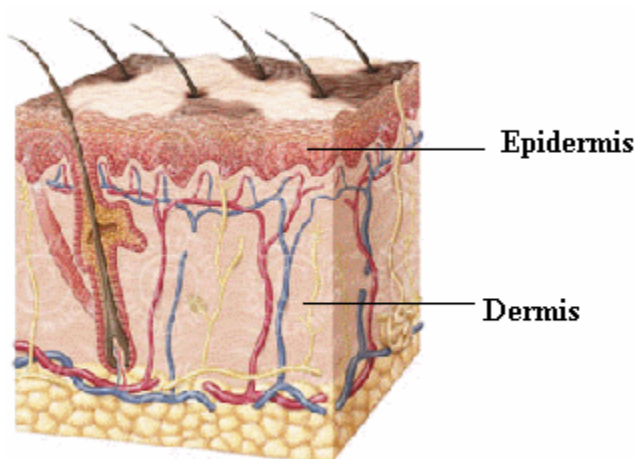


Fig 2. Dermis Structure (<http://drprabhattachandon.files.wordpress.com/2007/08/leucoderma1.gif>)

### 1.2.3 The appendages

Hair follicle (see Fig 3) is part of the skin that grows hair by packing old cells together. Hair follicle exists both in epidermis and dermis. The root of it lies in the deeper layer of the dermis which is illustrated in Fig 3. As shown in Fig 3, attached to the follicle is a sebaceous gland, a tiny sebum-producing gland found everywhere except on the palms, lips and soles of the feet. The thicker density of hair, the more sebaceous glands are found. An envelope wrapping around the hair follicle and thus it creates a channel from skin surface to the root of the hair follicle. This channel can act as a port to environmental material penetration to skin

down to the hair follicle root. After growing, the whole length of hair follicle can reach to 1 mm (Genina, 2002).

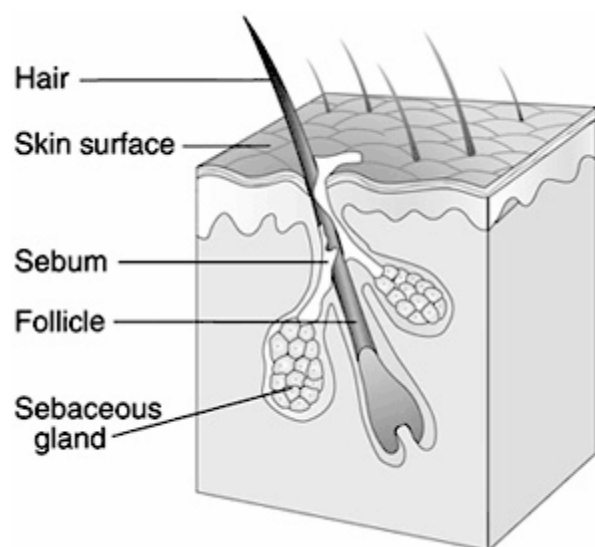


Fig 3. Hair structure

(<http://content.answers.com/main/content/wp/en-commons/thumb/0/07/250px-HairFollicle.png>)

### 1.3 Skin optics: skin autofluorescence and lifetime distributions

Skin is coloured. Although the main skin colouration comes from pigments, such as melanin and haemoglobin, there are several types of endogenous, i.e. intrinsic, fluorophores. Upon optical excitation, these fluorophores emit fluorescence, called skin autofluorescence. Examples of endogenous fluorophores mainly include nicotinamide adenine dinucleotide / nicotinamide adenine dinucleotide phosphate (NAD[P]H) and flavoproteins (FAD) (see Table 1). The NAD[P]H excitation wavelength is 325 nm, in the ultraviolet (UV) spectral range. Its fluorescence emission spectral range is 400 – 500 nm (see Fig 4). The FAD is excited at 450 nm, with emission in the spectral range of 500 to 600 nm (Masters, 1998; Harvey, 2000; Laiho, 2005). The other type of light interaction with tissue relates to the nonlinear optical phenomena that are induced by extremely high optical intensity. These phenomena will be explained and classified later in Sub-Section 1.6.2. Meanwhile, it is worthy to mention that such tissue as collagen, that is a major component of various animal tissues, including dermis, supports such type of non-linear optical interaction called second-harmonic generation (SHG), which manifests itself by generating light of precisely twice the excitation frequency, thus, rendering this collagenous tissue optically detectable (Laiho, 2005). Autofluorescence spectra and intensity depend on skin physiological conditions, age, sites, race and gender (Na, 2000; Na, 2001; Fu, 2001). Autofluorescence can be used as a source of

natural contrast in fluorescence microscopy for *in vivo* and *in vitro* imaging of human skin morphology (Masters, 1997), as can be seen in Fig 40 and Fig 42.

The endogenous fluorescence does not only provide useful source of skin morphology contrast, but also results in unwanted skin autofluorescence background, which needs to be suppressed in case of imaging of an exogenous, i.e. externally introduced, fluorophore of interest.

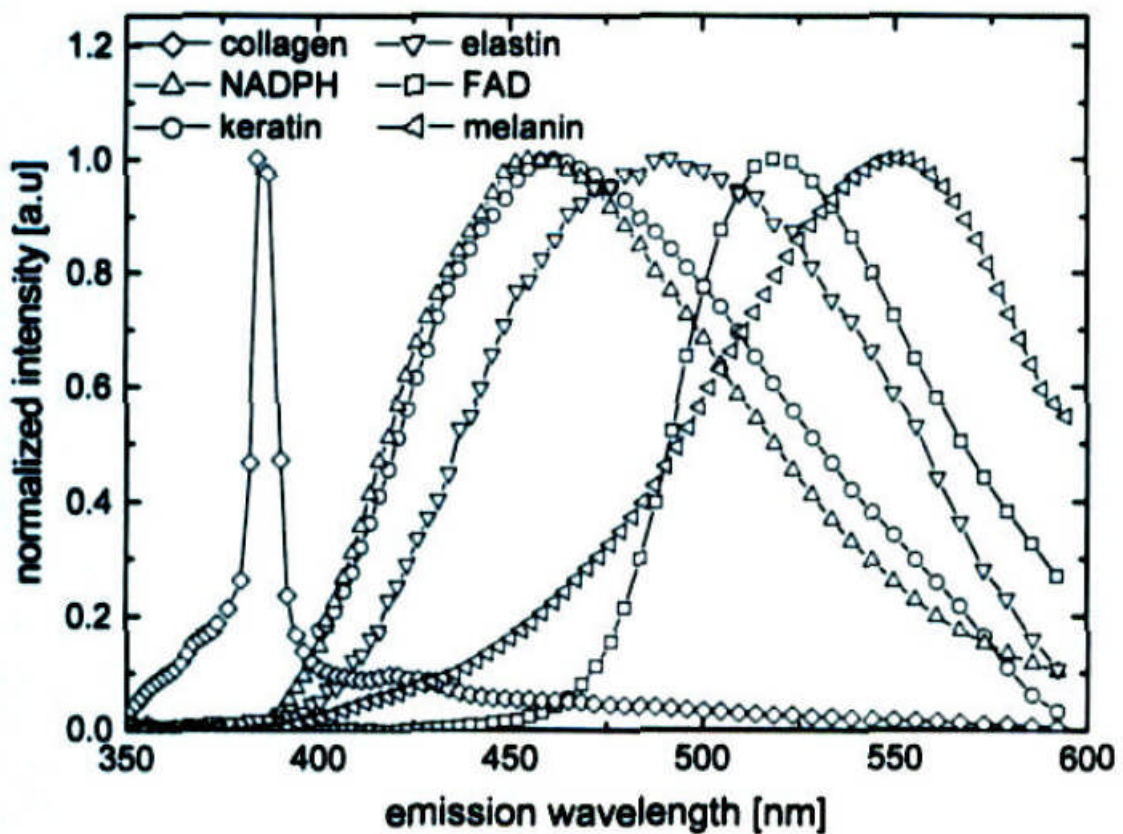


Fig 4. Normalized measured spectral emission of pure samples of keratin (circles), NAD[P]H (upright triangles), FAD (squared): Flavoproteins, collagen fibre (diamonds), elastin (inverted triangles), and melanin (left triangles) using 764 nm excitation wavelength (Palero, 2007)

Fluorophores are characterized by a fluorescence (luminescence) lifetime, usually denoted as  $\tau$ . The fluorescence lifetime refers to the average time a molecule stays in its electronic excited state before emitting a photon (more detailed account is given in Sub-Section 1.6.4). Apparently,  $\tau$  is unique to fluorescent species. This provides an additional discrimination parameter to distinguish two fluorophores, which have overlapping spectral emission bands. From the reference sources, the skin fluorophore decay is often fitted with a two component exponential decay model, considered with offset (see Fig 5, more details of fitting are in Sub-Section 1.6.4). The two component exponential decay is presented as:

$$F(t) = A_1 e^{-t/\tau_1} + A_2 e^{-t/\tau_2} \quad 1)$$

where  $\tau_1$  and  $\tau_2$  are decay times (König, 2006), and  $A_1, A_2$  are distributions of two lifetimes.

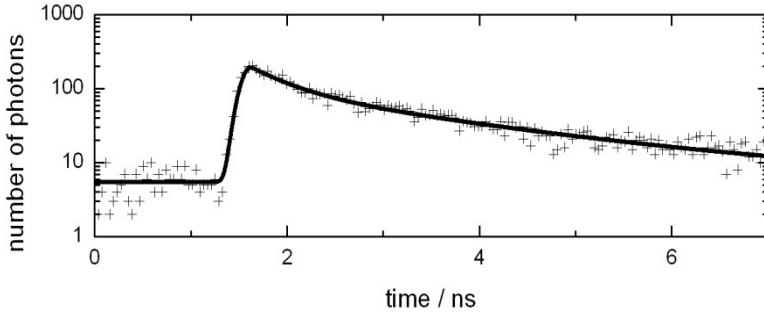


Fig 5. Experimental lifetime decay curve (crosses) fitted by a two-exponent decay curve model (solid line) (König, 1997; König, 2006)

As it has been found by König, keratin is the main endogenous fluorophore in *stratum corneum* (König, 2006).  $\tau$  of keratin determines fluorescence lifetime of *stratum corneum* measured to be 0.2 ns ( $\tau_1$ ) and 1.9 ns ( $\tau_2$ ). In *stratum spinosum*, NAD[P]H is a dominant fluorophore characterized by a double-exponential lifetime of parameters 0.4 ns ( $\tau_1$ ) and 2.3 ns ( $\tau_2$ ). In *stratum basale*, the value of lifetime is 0.3 ns ( $\tau_1$ ) and 2.2 ns ( $\tau_2$ ). In dermis, the fluorescence lifetime is predominantly due to collagen: 0.06 ns ( $\tau_1$ ) and 1.8 ns ( $\tau_2$ ), which is set by the extremely fast SHG process time constant, and typical collagen fluorescence lifetime (König, 2006). The exponential decay curves are shown in Fig 6.



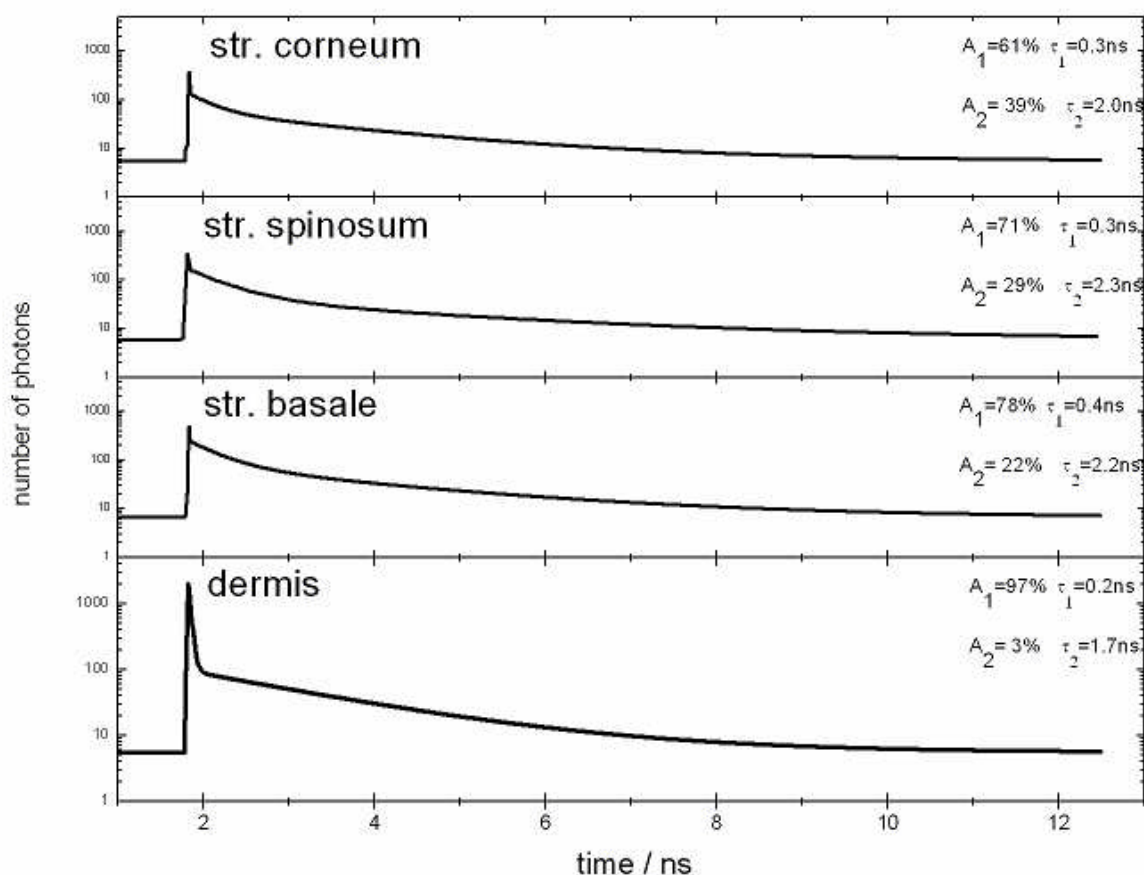


Fig 6. Decay curves acquired in the different layers in skin (König, 2006)

Excitation/emission bands and lifetime distributions of the main skin fluorophores are shown in Table 1:

**Table1. Emission bands and lifetime distribution (König, 2006)(Becker, 2006; König, 2003)**

Fluorophore	Excitation (nm)	Emission (nm)	Lifetime (ns)
NAD[P]H	290/340/350	440-470	0.3/2.3
Flavoproteins	370/450	430	5.2
Elastin	290-340	420-460	0.2-0.4/0.4-2.5
Collagen	300-340	420-460	0.2-2.5
Melanin	Ultraviolet (UV)/Visible, 466	430/440/545/520/555/575	0.2/1.9/7.9
Collagen (SHG)	750-850	375-425	<0.050
Keratin	~800	525	1.6

Organic fluorophores are prone to photobleaching. Photobleaching is a process of the photochemical destruction of a fluorophore: typically, a chemical reactivity of a fluorophore in excited state is increased dramatically, resulting in fluorophore oxidation, and hence losing its fluorescence property. Photobleaching has plagued the fluorescence microscopy for decades, as the imaging process is accompanied by a loss of participating fluorophores: with every imaging scan, a fluorescent image becomes dimmer. This is especially problematic in the time-lapse microscopy. The photobleached fluorophores, however, can be replenished by active fluorophores diffusing into the photobleached volume (PBV) from the vicinity. This diffusion process is described by a diffusion coefficient that is affected by various processes in skin, and also depends on the skin biological pathway.

#### **1.4 Skin permeability: skin biological pathways**

Ubiquitous distribution of endogenous fluorophores throughout epidermis and dermis, and also dermal collagen (that exhibits high contrast in SHG signal) enables fluorescence confocal and nonlinear optical imaging of skin *in vivo* and *in vitro* (see for example Fig 40 and Fig 42). At the same time, introduction of exogenous fluorophores in skin, e.g. by topical application, enables the visualisation of their localisation and distribution in skin using the same imaging techniques. Simultaneous imaging of the 3D skin layout and exogenous fluorophores, which serves to model drugs, drug delivery vehicles, or environmental pathogens, enables study of transdermal drug delivery and environmental impact on skin *in vivo* and *in vitro*. In this Sub-Section, the state-of-the-art of the skin permeability will be overviewed.

The epidermis skin barrier is the major factor of skin permeability, which can reduce overall rates of accumulation of chemical molecules applied on skin surface by several orders of magnitude. For example, most water-soluble, low-molecular-weight non-electrolytes applied to the skin surface could diffuse into the bloodstream approximately 1000 times more rapidly if the epidermis were diseased, damaged or removed. The major result of the early work on the skin found that the principal “barrier” function of the epidermis resides almost entirely in the *stratum corneum*, the thin coherent membrane of keratinized, epithelial cells that comprise the “dead” surface layer of the epidermis (Scheuplein and Blank, 1971). The permeability of water within *stratum corneum*, for example, is  $0.2\text{--}0.4\text{ mg cm}^{-2}\text{ hr}^{-1}$  at a temperature of  $30^{\circ}\text{C}$  measured both *in vivo* from a non-sweating region of the forearm or abdomen and *in vitro* from excised skin (Burch, 1946; Baker, 1967).

Although *stratum corneum* is the main barrier of diffusion, it is still considered as a major

permeation pathway (Benson, 2005). *Stratum corneum* is composed of 10-15 layers of corneocytes and varies in thickness from approximately 10-15  $\mu\text{m}$  in the dry state to 40  $\mu\text{m}$ , when hydrated (Benson, 2005). It is also called a bricks and mortar frame. The corneocytes are bricks, whereas the lipids are mortar (see Fig 7). Substance diffusion through the lipid bilayers or corneocytes is considered as intercellular and intracellular diffusion, respectively. Appendages such as hair follicles and sweat ducts pierce the skin from epidermis to dermis and can act in the role of diffusion shunts or easier diffusion pathways in parallel to the normal pathway directly through *stratum corneum* (Scheuplein and Blank, 1971). This pathway is called trans-appendageal pathway (see Fig 8). Therefore, there are three major pathways existing in skin: intercellular, intracellular and trans-appendageal pathways.

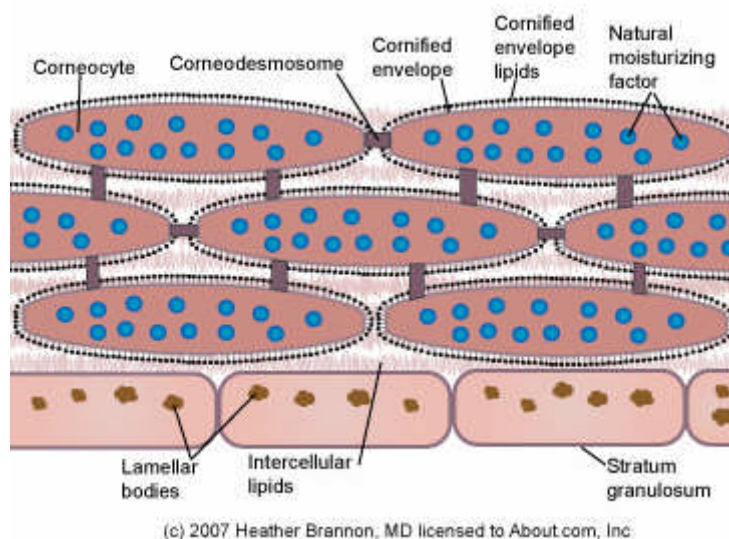


Fig 7. Simplified diagram of *stratum corneum*

(<http://www.razor-gator.com/SkinAcidsPhotos/Stratum-Corneum.htm>)

The gap between *stratum corneum* dead corneocytes in air-dried condition is 75 nm. The lipid matrix is composed of a mixture of lipids which arrange in head-head and tail-tail configuration. The distance existing between head to head is  $2.8 \pm 1.3$  nm, while is 12.8 nm between tail to tail, comprising a central fluid area (2.37 nm), and two adjacent areas (4.57 nm each) (Baroli, 2007). The keratin intermediate filaments appear as 7.8 nm wide electron-dense structures with a median filament centre-to-centre distance of 11 nm (Norlen and Al-Amoudi, 2004). These data suggest that, mechanistically, a nanoparticle sized larger than 13 nm does not fit into the lipid bilayers canal size. However, some drugs such as terpene can overcome this limitation due to the hydration levels of the lipid system increased by forming new aqueous channels (Narishetty, 2005). Substances of terpene are e.g. L-menthol, 1,8-cineole and limonene.

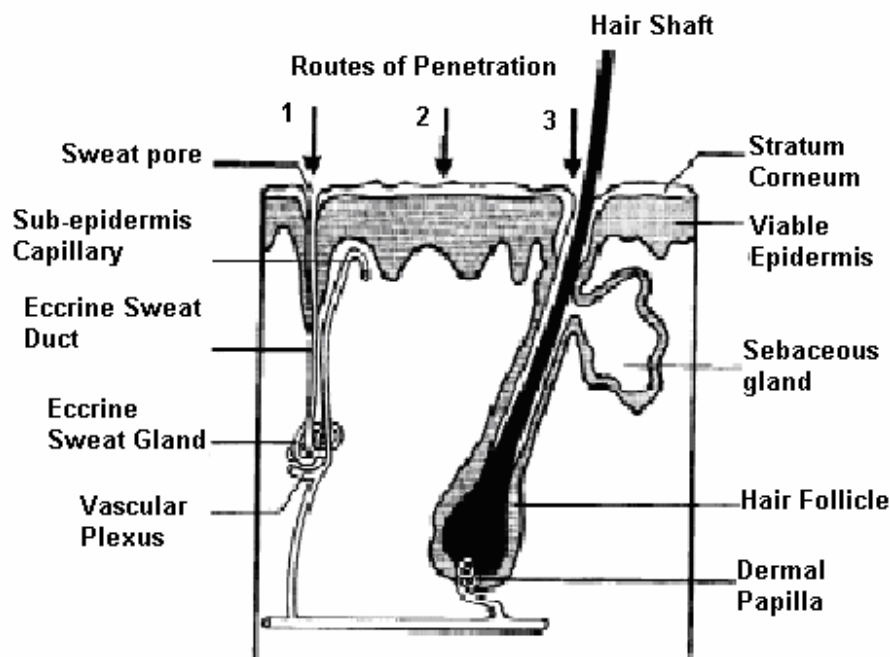


Fig 8. Simplified diagram of skin structure and macro-pathways of drug penetration: (1) via the sweat ducts; (2) across the continuous *stratum corneum* or (3) through the hair follicles with their associated sebaceous glands (Barry, 2001)

Fig 8 shows another two permeation channels for molecules and particles other than *stratum corneum*, which are sweat pores and hair shafts. They are both called trans-appendageal pathways. The diameter of pilosebaceous pores (hair follicle and its sebaceous gland) is 10 to 70  $\mu\text{m}$  (Lauer, 1996) and that of the sweat gland pores is 60 to 80  $\mu\text{m}$  (Baroli, 2007), as shown in Fig 8. These micron-size cavities provide alternative ports for molecules/nanoparticles penetration, although the effective area of these pores is small with respect to the skin surface area (0.1% of the total skin area) that limits dramatically their permeation capacity.

#### 1.4.1 The intercellular pathway

The intercellular lipid domain of *stratum corneum* is the main lipid pathway of drug molecules (Yoneto, 1996). They are composed of fatty carboxylic, ceramide, and cholesterol, and exist in the form of multi-bilayers (Johnson, 1996). Intercellular pathway is the common and main pathway for drugs permeation into skin since it overcomes the *stratum corneum* by passing between the corneocytes (Trommer and Neubert, 2006). Previous results showed that the hydrated intercellular keratin is the rate-limiting diffusion medium (Scheuplein and Blank, 1971). Importantly, it has been demonstrated that the diffusion coefficient through the skin

lipids is size-dependent (Johnson, 1996; Mitragotri, 1999; Bemporad, 2004). This size-dependency is bifunctional characterized by the strong size dependence for small solutes (< 300 Da represented by low-molecular weight species, e.g. salicylic and carboxylic acids) and weak size-dependence for solutes of molecular weight > 300 Da. For the small solutes, the diffusion coefficient ranged from  $10^{-5}$  to  $10^{-9}$  cm<sup>2</sup>/s, while for the large-molecular-weight solutes, it ranged from  $10^{-7}$  to  $10^{-9}$  cm<sup>2</sup>/s (Johnson, 1997). A majority of techniques to enhance permeation of drugs across the skin are focused on manipulation of solubility in the lipid domain or alteration of the ordered structure of this region (Benson, 2005).

#### **1.4.2 The intracellular pathway**

Intracellular pathway is the most straightforward pathway for substance penetration into skin, as it provides the shortest geometrical path to epidermis through the dry corneocytes and lipid bilayers. Nevertheless, this pathway is characterized by significant resistance due to its dual, hydrophilic and lipophilic, nature (Trommer and Neubert, 2006). Corneocytes are predominantly hydrophilic, whereas lipid bilayers are lipophilic. This is unfavourable for most substances, including drugs, as having a fixed value of lipo- and hydro-philicity (Benson, 2005). Although inefficient, the intracellular pathway cannot be completely ignored. In fact, in several cases, it plays an important role. For example, it has been demonstrated that intra-corneocyte diffusion took place for the hydrophobic and hydrophilic model drugs (Yu, 2003). It has been found that the corneocyte-phase transport played a major role for four permeating substances: water, ethanol, nicotinamide and testosterone, which presented a marked contrast to the commonly stated doctrine that the *stratum corneum* transport pathway was primarily intercellular (Wang, 2006).

#### **1.4.3 The trans-appendageal pathway**

Trans-appendageal pathway is another route for substance penetration, especially important in the framework of nanoparticle penetration through skin. The most important representative of this pathway is a hair follicle, as shown in Fig 8. Although the effective area of the trans-appendageal ports occupy only 0.1% of the total human skin area, they still play an important role as theoretical vertical pathways for percutaneous penetration (Trommer and Neubert, 2006). Indeed, Thune and colleagues have suggested that the hair follicle routes might be an alternative pathway for ZnO-nano bypassing the *stratum corneum* (Thune, 1988; Sznitowska, 2001). In several literature references, penetration of particles of various sizes through the hair follicles has been reported: 1. 300-400 nm diameter nanoparticles were forced into the hair follicles by the movement of the hairs *in vivo* and stored there for 10 days (Lademann, 2006);

2. 40 nm nanoparticles were preferentially absorbed in the skin *via* the hair follicles *in vivo* and *in vitro* in comparison with the 130 nm particle absorption (Shim, 2004); 3. 30 nm ZnO-nano and 10 nm cerium oxide were retained in the hair follicle opening and around the desquaming corneocytes (Roberts, 2006); 4. Size of microsphere optimal for penetration through the hair follicle was found to be 1.5  $\mu\text{m}$  with the maximum penetration depth  $>2300\ \mu\text{m}$ , well within the reticular dermis (Toll, 2004).

## **1.5 Skin permeability to nanoparticles and small molecules**

### **1.5.1 Particles penetration through the skin pathways**

From a common sense, skin should provide adequate protection against environmental assault, including toxins and pathogens. However, increasing evidence has been found that some micro- or nano- particles of certain size, shape and coating, can penetrate through the *stratum corneum*. The penetration depth and localisation for certain particles have been being hotly debated. In Sub-Section 1.4, the three main skin permeability pathways have been detailed: through intercellular, intracellular and trans-appendageal pathways. In order to investigate nanoparticle permeation, or penetration, through skin, nanoparticles under study must be detectable, either in integral form (in clusters, or as continuum distribution), or individually. A multitude of nanoparticles are detectable using variety of methods, including radioactive tracing, magnetic resonance imaging and spectroscopy methods, analytical chemistry methods, etc. Each method has its merits and limitations. In this work, optical, and in part, electron microscopy methods of investigation of nanoparticle penetration in skin will be focused on. The optical imaging techniques provide a subcellular-resolution, non-invasive alternative to all existing methods, combination of these properties being unique. Inexpensive implementations of the emerging optical imaging techniques result in their widespread use as nanoparticle imaging and characterisation methods of choice. These methods will be focused on in the following review. More specifically, an important subset of optical imaging techniques is fluorescence imaging for visualisation of nanoparticles on the crowded background of skin morphology and autofluorescence. Therefore, it becomes critical to introduce nanoparticles that possess suitable fluorescence/luminescence properties, and this will be presented in Sub-Section 1.5.1.2 and 1.5.1.3.

In particular, ZnO-nano and TiO<sub>2</sub>-nano, as two main nanomaterials in the commercial sunscreens, are very important in biomedicine. ZnO-nano appears to be visible using the FMM imaging technique. Therefore, the transdermal permeability and cytotoxicity of these two chemicals warrants thorough investigations. Qdots represent very attractive models for

the transdermal nanoparticle penetration study, as they are very bright and photo stable. Due to the most recent progress in their production and surface modification with functional groups, they are available commercially and hence beneficial for the study. More details of these particles will be discussed in Chapter 2. Skin permeability to micro- /nano- particles including ZnO-nano, TiO<sub>2</sub>-nano and Qdots, have been a focus of intensive studies.

#### **1.5.1.1 Microparticles and nanoparticles skin permeability**

The skin permeability to micro- and nano- particles depends on the particle size, shape, surface charge, and surface functional groups. It has been demonstrated that microparticles can penetrate through the porcine skin, but they hardly pass the human *stratum corneum* (Miyazaki, 2003; Mulholland, 2002; Gamer, 2006). One paper has reported 48- $\mu$ m polystyrene sphere delivery to the excised human epidermis (Mulholland, 2002). The vast majority of research groups have reported that the microparticles stayed on the surface of the skin or slipped into the hair follicle (Toll, 2004; Vogt, 2006). The tape-stripping method or/and washing methods were used to prove the human *stratum corneum* impenetrability to microparticles. However, Tickle has demonstrated that the physical enhancement methodology, such as sustained mechanical skin flexing, facilitated the microparticle (sized 0.5-1  $\mu$ m) penetration into the human epidermis, and, occasionally, dermis (Tinkle, 2003). The microparticle penetration depth has also been found to be a function of the particle density, size and impact velocity for diameters ranging from 0.89 to 53  $\mu$ m (Kendall, 2004). Nanoparticles smaller than 100 nm, such as airborne nanosized particles, had more probability to penetrate through human *stratum corneum* than microparticles and be localised in epidermis or dermis (Oberdorster, 2005). Once the nanoparticles were in dermis, they would localise in the regional lymph nodes (Stracke, 2006). Surface coating of particles also played a very important role in cytotoxicity and irritation potential in epidermis. Carboxyl-coated Qdots have been found stimulating release of the proinflammatory cytokines 1L-1Beta, IL-6 and IL-8 (Ryman-Rasmussen, 2007).

It is important to note that some chemicals can enhance the transdermal penetration of nanoparticles. Hydrophilic, fluorescent Qdots (20 nm) have been found to penetrate the human skin, treated with chemical enhancers: oleic acid, through the intercellular pathways (Dong, 2004). The pathways of Qdots sized under 50 nm in porcine skin have been investigated. In this study, three types of surface-functionalised Qdots have been examined: neutral, cationic, and anionic in solvents of moderate pH, that was realised by grafting PEG, amine, and carboxyl functional groups on their surface. It has found that neutral and cationic

ellipsoid Qdots were localized within the porcine epidermal layers by 8 hours. No penetration of anionic Qdots was evident in porcine skin until 24 hours (Ryman-Rasmussen, 2006).

#### **1.5.1.2 ZnO-nano and TiO<sub>2</sub>-nano penetration in skin**

ZnO-nano and TiO<sub>2</sub>-nano, absorb both UVA (400 nm - 320 nm) and UVB (320 nm - 290 nm) radiation and re-emits it as less damaging UVA or as visible light through photoluminescence (PL). Since their sizes are on the scale of nanometres, their penetration into the deeper skin layers through *stratum corneum* or through hair follicles cannot be ruled out, and their potential cytotoxic effects should be avoided. However, under what circumstances and how deep they penetrate skin remains unknown. Most recent studies have pointed out that these nanomaterials used in sunscreen posed no risk to human skin or human health (Hayden, 2005; Cross, 2007; Nohynek, 2007). However, if they penetrated into epidermis and exposed to cells, apoptosis would occur and cells became necrotic as the concentration is increased (Jeng and Swanson, 2006).

ZnO-nano (26-30 nm measured by TEM, see in Fig 9) material properties, including a direct wide bandgap (3.4 eV) electronic structure, and the high exciton energy of 60 meV (compared to that of 25 meV of cadmium selenide), are very attractive for a new generation of electro-optic devices, e.g. light-emitting diodes and lasers in the UV spectral range. The wide bandgap of ZnO-nano demands excitation at a wavelength of 320 nm in the UV spectral range, with principal emission at 385 nm. This excitation requirement is problematic for application of ZnO-nano in optical biomedical imaging. It has been recently found that the zinc oxide structure is efficiently excited via a nonlinear optical process of simultaneous absorption of two- or three-photons under illumination by an ultrashort-pulse laser (Dai, 2005). This shifts the ZnO-nano excitation band to the infrared (IR) range, where the ultrashort-pulse laser sources predominantly operate, falling into the so-called therapeutic window, 600 nm – 1400 nm. ZnO-nano PL lifetime has been reported as 322 ps for bulk state (Zhang, 2006). The range of lifetimes was from 375 ps to 260 ps due to the different crystal states such as 6Zn+O, 5Zn+O, Zn+O<sub>4</sub> (Brauer, 2007).

TiO<sub>2</sub>-nano (15 nm measured by TEM, see in Fig 9) is non-luminescent nanomaterial due to a wide electronic bandgap of 3.21 - 3.4 eV (Lei, 2005), difficult to excite with available light sources in the biological context, and low quantum yield. In order to visualise this nanomaterial under FMM, it needs to be labelled with a fluorescent molecule, such as pyrene. Pyrene excitation has been reported to be in the wavelength range of 300-400 nm (Bauer,



1982; Jin and Kusumoto, 2003), and emission is centred at 373 nm (Ipe, 2005; Honda, 2006; Lee, 2007). Note that excitation/emission spectra are similar to these of ZnO-nano.

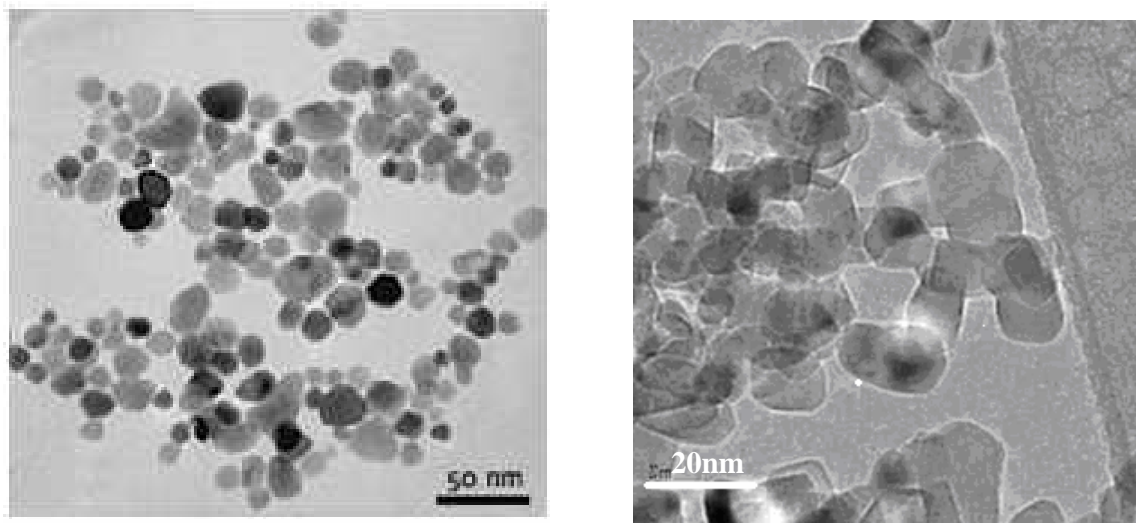


Fig 9. Transmission electron microscope (TEM) images of ZnO-nano (left) and TiO<sub>2</sub>-nano (right). (Nohynek, 2007 and [http://www.ntu.edu.sg/cwp/images/clip\\_image002.jpg](http://www.ntu.edu.sg/cwp/images/clip_image002.jpg))

#### 1.5.1.3 Quantum dots (Qdots)

Qdot represents a semiconductor nanocrystal of size so small that the Bohr radius of an electron orbital in the conduction band exceeds the nanocrystal physical size. It results in quantisation of the energy levels of the excited Qdot, and its atom-like fluorescence properties. Qdot fluorescence is typically bright, with a high, close to unity, quantum yield. In order to prevent trapping of an excited electron by the surface defects, the Qdot surface is coated with the so-called passivation shell. In order to avoid its high cytotoxicity, a Qdot is additionally polymer-capped. One of the most efficient fluorescent Qdot (14-35 nm, nowadays, available commercially, e.g. via Invitrogen) comprise a cadmium selenide core, and a zinc sulphide shell (CdSe/ZnS), as shown in Fig 10. In addition to a polymer coating, Qdot is surface-functionalised for biomedical applications. It has a PEG-coating, or its surface is grafted with carboxylic or amino groups. This organic coating makes it water soluble and prevents Qdots aggregation in salt-free solvents (Smith, 2006). These water-soluble Qdots are currently used for biomedical imaging in animals, amongst other things, permitting cell tracking and labelling tumour cells (McNeil, 2005). It has been demonstrated that a cellular uptake of the Qdots depended on their surface functional groups (Chang, 2006; Ryman-Rasmussen, 2007). There is no doubt that plane Qdots are toxic under normal circumstances (Duan and Nie, 2007; Ryman-Rasmussen, 2007).

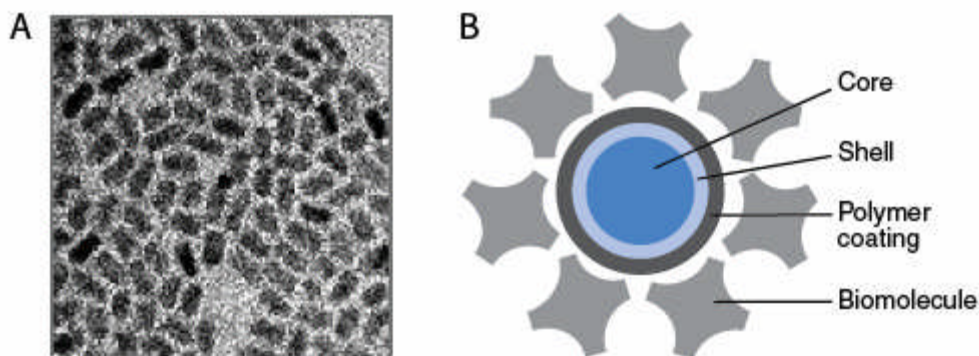


Fig 10: Structure of a Qdot nanocrystal. A. Qdot nanocrystals containing core and shell components only are shown in this TEM image (200,000 $\times$  magnifications). B. In this schematic of the overall structure of a Qdot nanocrystal conjugate, the layers represent distinct structural elements and are roughly to scale (Invitrogen)

#### 1.5.1.4 Physical and chemical enhancements

It has been found that transdermal nanoparticles penetration could be considerably enhanced in response to skin treatment, which is categorised into physical enhancement and chemical enhancement.

##### Physical enhancements

Physical enhancements mainly include mechanisms to transiently circumvent the normal barrier function of the *stratum corneum* and to allow the passage of macromolecules and nanoparticles. Although the mechanisms are different, these methods share the common aim to disrupt *stratum corneum* structure in order to create “holes” big enough for nanostructures to permeate (Thong, 2007). After exercising the skin, the gap between corneocytes and, maybe, lipid bilayers can be enlarged and thus the skin allows particles of the size larger than normally permeable passing through. For example, Tinkle has reported that particles as large as 0.5-1.0  $\mu\text{m}$  penetrated the exercised human skin *stratum corneum* and reached the epidermis, and occasionally dermis (Tinkle, 2003). This shows stretching and flexing is an effective and non-invasive method (compared with the micro-needle method) to improve particle penetration. Also, it raises a concern that daily life motion, such as wrist movements, could introduce some harmful particles into the skin, with a range of toxic consequences.

##### Chemical enhancements

Alteration of the skin lipid structure represents another enhancement strategy with the result of skin permeability temporarily increases. Usually, the structure of the lipid bilayers is remodified by chemical means, and thus the skin is rendered permeable to nanoparticles and

macromolecules, which cannot penetrate under the normal conditions. A number of chemicals have been introduced to act as chemical enhancers. These are oleic acid (Mak, 1990), laurocapram (Lopez-Cervantes, 2006), Aloe Vera (Cole and Heard, 2007), terpenes (Narishetty and Panchagnula, 2005) and even some components in commercial sunscreen such as octinoxate (Hayden, 2005).

### **1.5.2 Determination of dye diffusion coefficient**

As mentioned before, *stratum corneum* is the main barrier and rate limitation media in skin. Its barrier and/or permeability properties can be quantified by introducing a local diffusion coefficient,  $D$ . In order to determine the skin diffusion properties, the drug molecule or molecular/particulate environmental toxin can be modelled by a fluorescence dye of similar diffusion properties. Therefore, it is essential to understand the dye diffusion mechanism within the *stratum corneum* in order to understand local diffusion processes in skin to achieve better control over the diffusion efficiency of drugs, or suppression of the diffusion efficiency of toxins. As described in Sub-Section 1.4, the *stratum corneum* is characterised by two biological pathways: intercellular and intracellular pathways. From the previous study, it is evident that *stratum corneum* is more penetrable by water-soluble compounds (Scheuplein and Blank, 1971). It also has affinity for low-molecular-weight molecules, less than 500 Da (Johnson, 1996), which is an important parameter in the transdermal drug development research. Therefore, water-soluble and low-molecular-weight dye should be representative for skin diffusion study. Table 2 shows the effective diffusion volumes and diffusivity of potential pathways of low-molecular-weight components through skin. It shows that  $D$  is much greater within the trans-appendageal pathway, but the permeability efficiency is significantly offset by the relatively small effective area of these pathways, i.e. insignificant area occupied by the hair follicles and sweat ducts per unit area of the skin. Although, the diffusion through skin has been studied thoroughly (Johnson, 1996; Johnson, 1997; Mukhopadhyay, 2004; Mitragotri, 1999), it is challenging to determine the diffusion coefficient in a skin site of interest, i.e. locally, as opposed to its integral measurements.

**Table2. Effective diffusion volumes and diffusivity of potential pathways through *stratum corneum* for water or other low-molecular-weight non-electrolytes (These values represent reasonable average over the whole body surface) (Scheuplein and Blank, 1971)**

Diffusion Pathway	Number/cm <sup>2</sup>	Fractional Diffusion Volume	Diffusion Constant $D$ cm <sup>2</sup> /s
Hair follicle	40-70	$1 - 2 \times 10^{-3}$	$5 - 20 \times 10^{-8}$
Sweat ducts	200-250	$3 - 5 \times 10^{-4}$	$1 - 20 \times 10^{-6}$
Intercellular		0.01(dry) 0.05(wet)	
Intracellular		0.999(dry) 0.999(wet)	$1 - 10 \times 10^{-11}$ $5 - 10 \times 10^{-10}$

The values in Table 2 indicate that the value of  $D$  can reveal the biological pathways of selected chemicals. Under real circumstances, the substance diffusion does not take place via only the intercellular or intracellular pathway. Rather, it occurs via both biological pathways. The dye diffusion coefficient spatial map should provide a comprehensive picture of the contribution of each pathway to the integral diffusion through skin, and dominant contribution of the *stratum corneum* permeability. Determination of precise values of  $D$  for each pathway represents a very attractive research goal, and will likely to provide a significant impact in the drug delivery research and technology.

## 1.6 Experimental techniques and instruments

### 1.6.1 FCSM (fluorescence confocal scanning microscopy)

An optical microscope, often referred to as the "light microscope", is a type of microscope which uses visible light and a system of lenses to magnify images of microscopic samples. Optical microscopes are the oldest and simplest of the microscopes. Its imaging technology is indeed mature, and traced several thousand years to its first demonstration. A modern optical microscope is mundane in its architecture and operation, and yet, is capable of providing a wealth of information on the micro-world structure and functional details. Sample preparation procedure is straightforward compared with other techniques such as SEM, atomic force microscopy, scanning tunnelling microscopy, etc. The most widespread optical microscopy

modalities in biomedicine are a compound microscope, FCSM and emerging NLOM (see Sub-Section 1.6.2).

FCSM is an imaging technique for obtaining high-resolution optical images at the submicron-scale resolution. The key feature of confocal microscopy is its ability to produce in-focus images of thick samples, a process known as optical sectioning (Booth, 2002; Cox, 1982; Gan, 1992). Images are acquired point-by-point and formed using a computer, allowing 3D-reconstruction of topologically complex objects. The excitation and emission optical beams are separated by a dichroic mirror in the illumination/detection path, so that only a fluorescence signal is detected.

Out-of-focus fluorescence generated along the excitation beam path, as e.g. in epi-fluorescence microscopy (see Fig 11), may result in blurred imaging of the sample under study. In order to overcome this problem, FCSM provides an efficient means to reject out-of-focus fluorescence (Wilson, 1991; Kimura, 1993). It is realised by placing a pinhole in front of a detector (see Fig 11). The pinhole size is optically conjugated with a focal spot size, so that only fluorescence originated from this focal spot passes through the pinhole and detected by an optical detector, usually, photomultiplier tube (PMT) tube assembly. Significant portion of the out-of-plane fluorescence, as well as the reflected laser light is blocked by the pinhole. In FCSM, fluorescence signal is sampled by a sensitive optical detector, which converts the optical signal into an analogue electrical signal (Sheppard, 1991). This signal varies versus the scanning position in the sample, thus, forming a 2D-image. The analogue signal is periodically sampled and converted into pixels by an analogue-to digital converter housed in the scanning unit or the accompanying electronics cabinet. The image information is temporarily stored in an image frame buffer card in the computer and displayed on the monitor. In this way, the confocal image of a sample is acquired, point by point, from emission photon signals by the PMT and accompanying electronics. Since the off-focus plane fluorescence is rejected, it increases FCSM optical sectioning capability that improves image contrast dramatically, and allows 3D-imaging (Sheppard, 1992).

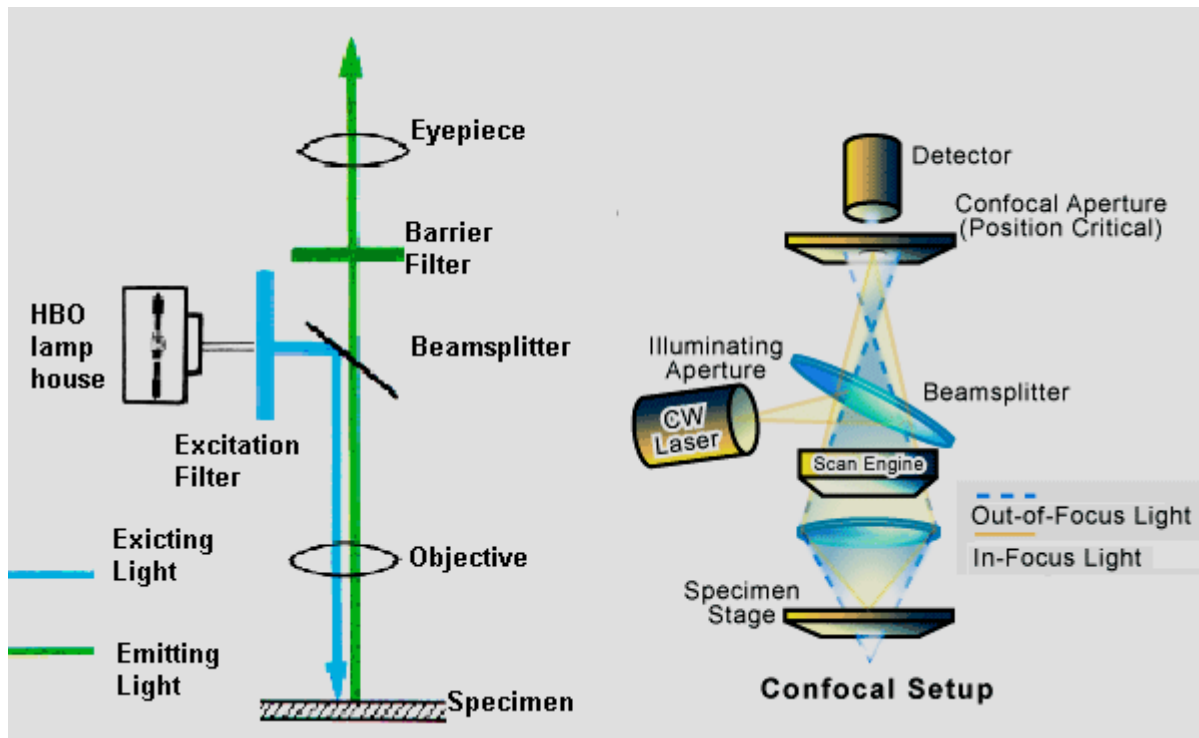


Fig 11. Epi-fluorescence microscopy and FCSM (<http://web.uvic.ca/ail/techniques/epi-fluor.jpg>)

### 1.6.2 NLOM (nonlinear optical microscopy)

The setup of a NLOM is similar to that of the FCSM. There are two main differences between these two microscopes. Firstly, NLOM operates in pinhole-free mode; secondly, it employs an ultrashort pulsed laser as the excitation source (Denk, 1997).

The ultrashort pulsed mode-locked titanium-sapphire laser operates in the near-IR spectral range (see Fig 12). The laser produces a high photon density (tens of kilowatts of peak power in a series of low-energy pulses that are approximately 10 nJ per pulse). The laser is tuned to a wavelength about twice that of the targeted absorption band of the fluorescent sample. An optical field of very high instantaneous intensity created by the femtosecond laser excitation and tight focussing stimulates simultaneous absorption of two or several photons in a sub-femto-litre volume at the focal point followed by emission of fluorescence that can be detected in the fluorescence microscopy detection path. Note that excitation occurs only in the focal volume and, thus, the excitation area is restricted to a femto-volume scale, which relaxes the requirement of a pinhole (as in FCSM) to achieve the optical sectioning effect. Out-of-focus photobleaching is also considerably reduced. In addition, light penetration in the sample is increased due to the reduced optical absorption and scattering efficiency in the near-IR range. Generally, the thickness of optical section is 2.5 to 3  $\mu\text{m}$ , which was confirmed by the experimental results in this study (see Sub-Section 4.2.2). This allows imaging of thick tissues (Helmchen, 2005), such as live human skin with considerably reduced photodamage

(Squirrell, 1999). Second harmonic generation (SHG) is another useful nonlinear optical phenomenon utilised in NLOM. Under high-intensity optical excitation, photon interaction with nonlinear material results in generation of photons of precisely twice the energy (twice the frequency, half the wavelength) of that of the excitation photons. This phenomenon generally takes place in non-centrosymmetric structures; tissue example of this is collagen.

An important merit of NLOM is that excitation of the UV-fluorophores occurs by IR light. This is very helpful for excitation and emission light separation. In addition, it is believed that the sensitivity of the system is increased, because the elimination of the pinhole allows a significant portion of the excited fluorescence to reach the detector, despite its wavefront distortions in the sample (Denk, 1997). Therefore, the signal-to-noise ratio (SNR), and, consequently, the image contrast, is improved. The comparison of two microscopes is in Table 3.

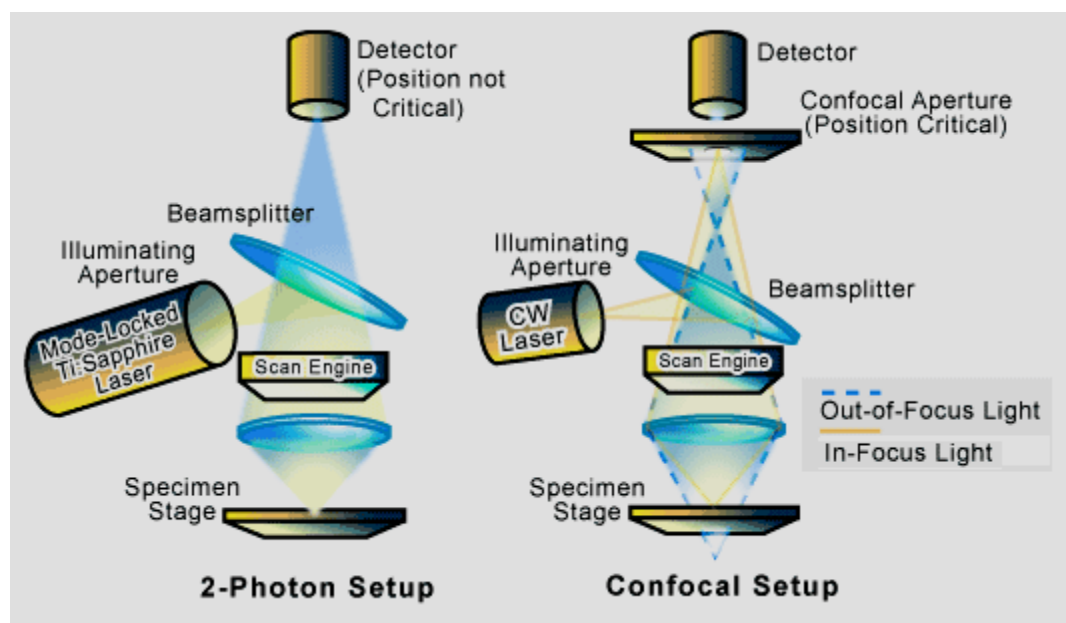


Fig 12. NLOM (left) and FCSM (right)  
(<http://www.scq.ubc.ca/wp-content/confocal.gif>)

Table 3. Comparison of FCSM and NLOM

	FCSM	NLOM
Excitation (nm)	UV or visible light	IR
Excited area	Excited fluorophores along the excitation beam path	Excited fluorophores in the focal plane (Sub-femto-litre volume)
Pinhole	Yes	No
Resolution	Submicron	Submicron
SNR	High	Low
Contrast	Low	High
Penetration Depth	100 $\mu\text{m}$ , average	200 $\mu\text{m}$ , average
Specimen Photodamage	High	Low
SHG	No	Yes

Due to the particular advantages of NLOM, deeper tissue penetration and reduced phototoxicity is attained. It is especially suitable for direct imaging of the nanoparticle and macromolecule penetration through the human skin and porcine skin *in vitro* and *in vivo* (Zheng, 2004; Stracke, 2006; Mulholland, 2002).

### 1.6.3 FRAP (fluorescence recovery after photo-bleaching)

FRAP is by far the most widely used method at the micron-scale resolution level for the dye diffusion study. It is compatible with the FCSM and NLOM systems, where its integration into these systems is straightforward. FRAP is based on the principal of observing the rate of recovery of fluorescence due to the movement of fluorescent markers into an area populated with the same markers. The markers are photobleached by an intense laser light locally. In FRAP, the focussed excitation beam of high intensity creates a volume of fluorophores at the focal spot that are photobleached, termed bleached volume. Scanning of a focussed spot in a controllable fashion produces a photobleached volume (PBV) of choice. On completion of the photobleaching process, fluorophores, e.g. fluorescent dyes, in the vicinity diffuse into the bleached volume and replenish the photobleached dye. As a result, the fluorescent intensity in the PBV is recovered in time (see Fig 13). Fluorescence Correlation Spectroscopy (FCS) is another technique suitable for experimental characterisation of fluorescent species (proteins, biomolecules, pharmaceuticals, etc.) and their motion dynamics in solutions. Using FCSM or NLOM, an excitation beam is focused in a sample and the measured fluorescence intensity fluctuation time evolution (due to diffusion, chemical reactions, aggregation, etc.) is analysed



using the time correlation signal processing toolkit. FCS is a fluorescent analogue to the dynamic light scattering, which uses coherent light scattering, instead of (incoherent) fluorescence time correlation analysis. The primary advantage of FRAP over FCS is the ease of interpreting qualitative experiments common in cell biology. Differences between cell lines, or regions in a cell, or before and after application of drugs, can often be characterised by simple inspection of time-lapse image series. Also, FCS experiments require a level of processing and are more sensitive to potentially confounding influences, including rotational diffusion, vibrations, photobleaching, dependence on illumination and fluorescence colour, inadequate statistics, etc. It is easier to change the measurement parameters in FRAP, which allows a better control.

FRAP has been successfully used to assess the translational mobility of various solutes in the cytoplasm, nuclei, and membranes. Besides, it has also been used to study the mobility of molecules in interstitial spaces of tissues and extracellular matrices such as cervical mucus and biofilms (Braeckmans, 2003). Recently, FRAP has been widely used in measuring the lateral diffusion coefficients in the *stratum corneum* (Yoneto, 1996). FRAP model describes a relation between the diffusion into a 2D- or 3D-bleached region and the fluorescence recovery was observed (Brown, 1999). In inhomogeneous tissues such as skin, the diffusion coefficient turned out to be complex, and depends on the environmental conditions. A method based on a fitting procedure of the intensity recovery after photo-bleaching with a two- or three-dimensional finite element analysis has been reported to determine  $D$  in the inhomogeneous tissue (Sniekers and van Donkelaar, 2005). Small bleached cross-sections (several  $\mu\text{m}^2$ ) of the PBV, termed bleached areas, are preferable for targeting at a single lipid (1  $\mu\text{m}$ ) or corneocyte (30  $\mu\text{m}$ ) (Johnson, 1997). Using FRAP, it is possible to target a 1- $\mu\text{m}^2$  area of the sample that is very important for intercellular and intracellular biological pathway permeability study.

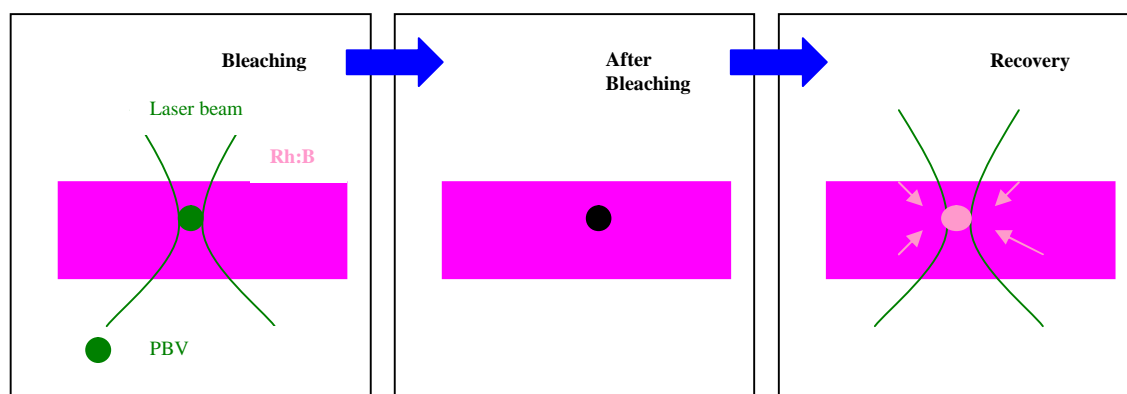


Fig 13. Illustration of fluorescence recovery after photo bleaching (FRAP). From left to right: A focussed laser beam bleaches a micron-size volume, representing as a green circle on a pink dye background, within the sample. After bleaching, the PBV becomes non-fluorescent (black) under fluorescence microscope. Fluorophores in the vicinity of PBV diffuse into it and replenish the bleached fluorophores

Multiphoton fluorescence photobleaching recovery is a technique for measuring the three-dimensional mobility of fluorescent molecules with a spatial resolution of a few micrometres. Laser light pulses of an ultrashort duration and high instantaneous intensity excite fluorescent molecules in an ellipsoidal focal volume, which results in photobleaching of a fraction of these fluorophores. Multiphoton excitation is intrinsically confined to the high-intensity focal volume of the excitation beam. Therefore, the bleached region is restricted to a known, three-dimensionally defined volume (Brown, 1999). This is very useful for targeted bleaching of lipids or corneocytes in *stratum corneum*.

In order to extract the useful information on the diffusion coefficient, a mathematic model is needed to fit the data acquired by using the FRAP method. This mathematic model should take into account the kinetic properties of the dye and also bleaching conditions, including a PBV, sampling time, and bleaching efficiency (i.e. percentage of the volume fluorophores bleached). Most of the published mathematic models are suitable for FCSM, and based on the Fick's law under certain constraints (Johnson, 1996; Braeckmans, 2003; Sniekers and van Donkelaar, 2005). Generalisation of these mathematic models to the case of FMM-based FRAP was accomplished by Dr Yuri Anissimov (Griffith University).

#### 1.6.4 FLIM (fluorescence lifetime imaging)

FLIM is a fluorescence lifetime imaging technique. When fluorophores are excited by laser light, they relax back to the electronic ground state, the process accompanied by emission of fluorescence. A time interval, at which the probability of the excited electronic state of the

fluorophore to the ground state is 1/2, is termed fluorescence decay lifetime,  $\tau$ . An ensemble of fluorophores will have a half of its population decayed at  $\tau$ . A decay curve is plotted as an evolution of the number of detected photons versus time, as shown in Fig 14.

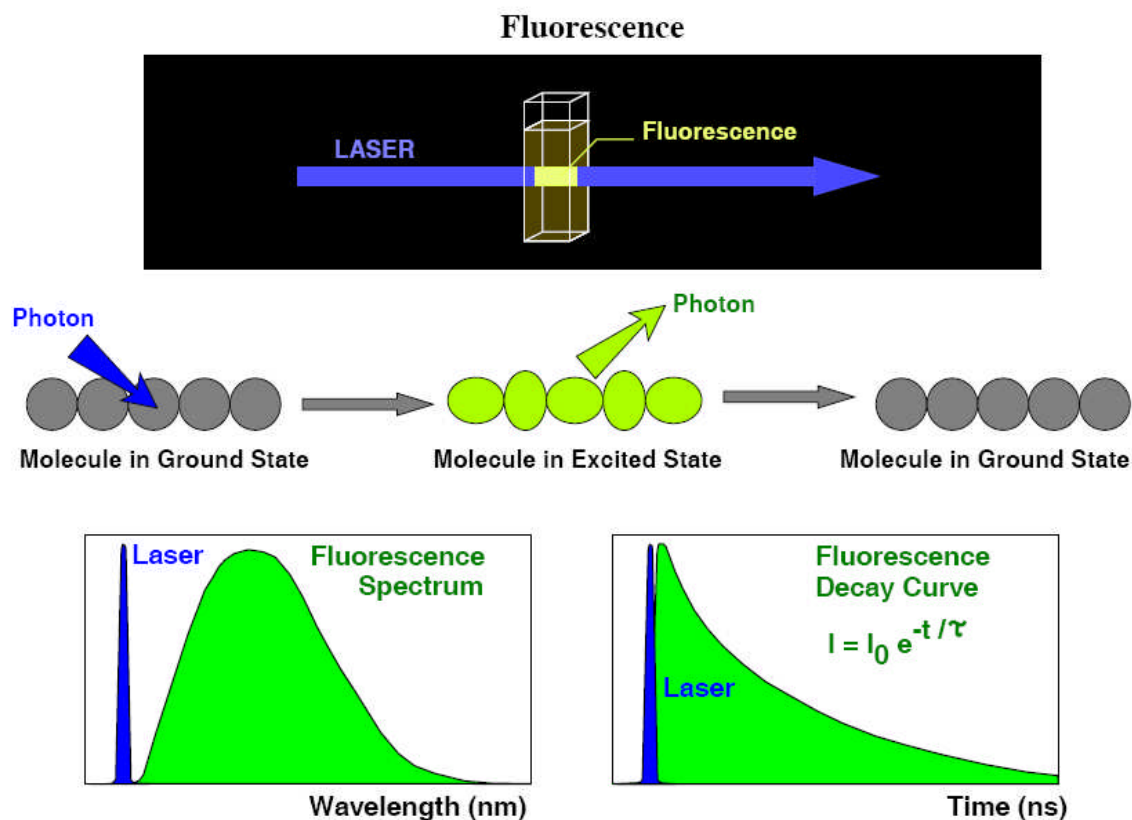


Fig 14. Illustration of FLIM (Becker, 2006): After laser excites the fluorophores, they drop back to the ground state from the excited state. The time of half of the molecules relax back to the ground state is termed lifetime

FLIM is an alternative method of discrimination of luminescent nanoparticles such as ZnO-nano on the skin autofluorescence background to enhance the fluorophore contrast. Since lifetime of ZnO-nano is much smaller ( $\sim 300$  ps) than that of the skin endogenous fluorophores (1-3 ns), it provides an additional discrimination of the PL nanoparticles from the skin autofluorescence background. It is very useful especially in the case that the fluorescent nanoparticles and the skin fluorophores have spectrally overlapping emission bands.

Normally, skin fluorophore decays are characterized by a two-component exponential decay, as mentioned in Sub-Section 1.3, which contains a fast decay time and slow decay time (see Fig 15).

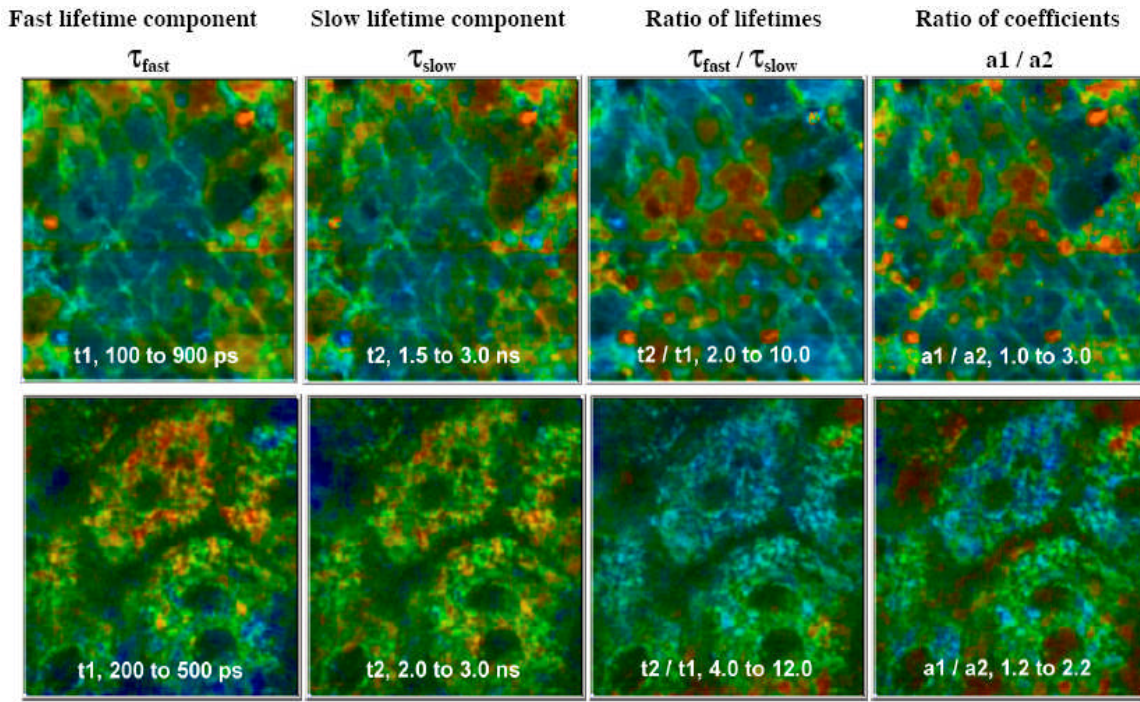


Fig 15. Skin lifetime imaging (Becker, 2006):  $t_1$  represents  $\tau_{fast}$  and  $t_2$  represents  $\tau_{slow}$ ;  $a_1$  is the percentage of  $\tau_{fast}$  and  $a_2$  is the percentage of  $\tau_{slow}$ ;  $t_1/t_2$  shows the ratio of two lifetime component values and  $a_1/a_2$  gives the information about which life component is dominant ( $a_1/a_2 > 1$ ,  $a_1$  is dominant;  $a_1/a_2 < 1$ ,  $a_2$  is dominant)

In the commercial FMM instrument (e.g. DermaInspect, JenLab, Germany), a FLIM detection and signal processing module is built in. It is based on the single-photon time correlation technique that relies on a high-speed PMT for rapid photon counting. The lifetime data fitting (number of photons verse time) is achieved by the attached software: SPCImage 2.8.

To get the curves shown in Fig 5 and Fig 6, the data is fitted by a mathematical convolution of the two component exponential decay function  $F(t)$  and the instrument response function  $R(t)$  in SPCImage 2.8.  $R(t)$  defines the overall time-resolution of the measurement system, FMM. It is built up by the pulse-width of the laser (which is negligible small for a femtosecond laser system), the electrical resolution of the TCSPS card and most importantly, the transit-time-spread of the detector. Considered with some ambient (room) light which together with the noise of the detector picked up by the detection systems, it is necessary to add a constant baseline or “offset” to the fitting function. This number has to be taken into account to avoid the artificial generation of a long-time component by the fitting process. The “offset”  $a_0$  can either be measured by an independent dark experiment or determined automatically by means of the photons which are in the time channels in front of the rising part of the fluorescence decay trace. Therefore, finally the fitting function is  $F(t) \otimes R(t) + a_0$ .

### **1.6.5 TEM (transmission electronic microscope) and SEM (scanning electronic microscope)**

Electron microscopy has a superior resolution than that of the light microscopy. That is because high-energy electrons have a smaller wavelength than photons. Ultimately achievable diffraction-limited microscope resolution is proportional to the wavelength of the source. In SEM and TEM, high-energy electrons in the beam are scattered or absorbed by a sample, respectively. The resultant electron beam modulated by the sample is detected and processed, thus, providing information on morphology and composition of the sample (Sanchez, 2005).

TEM is a scanning electron microscope imaging modality whereby a beam of electrons is focussed onto a sample, and their absorption/scattering is detected in transmission, rather than in reflection. The transmitted electrons are detected on a fluorescent screen or layer of photographic film, or an intensified CCD camera. TEM is used for biological applications that include tomographic reconstructions of small cells or thin sections of larger cells and 3D-reconstructions of individual molecules. Along with providing the Ångström-scale resolution image (allowing information on features on the scale of 0.1 nm to be obtained), it is useful for imaging microparticles and nanoparticles whose features are on the Armstrong-scale (Sinico, 2005).

SEM provides morphology and topography images as well as cross-section images of the skin, which allows study of skin before and after physical treatments, such as tape stripping. Also, it provides a large field of view and 3D-structure which is very useful for searching a site of interest, e.g. nanoparticle local distribution in skin. The resolution of this instrument is attainable at the scale of <10 nm (Tinkle, 2003; Kaufman, 2007). This makes SEM a useful research tool for imaging nanoparticle penetration. In contrast with TEM, SEM does not require nanometre-thin sample preparation, so that the choice of samples is much broader. It also has the function of creating electronic distinctive X-rays (EDS) that is capable of high-magnification sample imaging and their elemental composition analysis is in very small volumes (<0.01 wt%) (Sanchez, 2005). After the electron beam hits the sample, transferring of energy from the primary electron to the atoms of the sample generates new electrons or characteristic X-rays which are presented as dispersive peaks in spectrum. These x-ray energy dispersive peaks provide information on atomic species presented in the sampled volume, and also on their concentration. Using EDS, the skin contamination with inorganic nanomaterial can be analysed and material can be uniquely identified.



## **Chapter 2 Physical and optical properties of ZnO-nano, TiO<sub>2</sub> –nano and Qdots**

### **2.1 Introduction**

Nanomaterials including nanoemulsions, nanosomes, and nanoparticles are employed as active components (Dietz and Bahr, 2004; Nohynek, 2007) and delivery vehicles (Xu, 2006; Beduneau, 2007) in cosmetics and medicine. One example of a nanotechnology application is the widespread use of ZnO-nano and TiO<sub>2</sub>-nano as activating ingredients in skin care productions and sun-blocking creams, to reduce the effects of sebum in cosmetic applications, as a pigment, a piezoelectric, and an antiseptic agent. Their use as a whitening agent in cosmetics is well perceived by e.g. babies. In plain terms, they are good for soothing effects for skin irritations, antimicrobial properties. The upper size limit for ZnO-nano and TiO<sub>2</sub>-nano is dictated by the aesthetic marketing value of transparent sun-blocking creams. Transparency is achieved by reducing scattering efficiency of ZnO-nano, which are normally white and visible, by using a nanoparticle size of less than 30 nm, its transparency threshold (Cross, 2007). Qdots, as one type of the nanoparticles, have many biological applications, such as brain tissue labelling (Sznitowska, 2001), biomedical imaging in animals, amongst other things, permitting cell tracking and labelling tumour cells (McNeil, 2005).

The rapid development of nanotechnology has posed two important questions. Firstly, environmental impact of nanotechnology needs to be carefully assessed, wherein the safety of the nanotechnology-based pharmaceutical and cosmetic products needs to be revisited. Secondly, nanotechnology brings a new possibility of drug delivery using nanoparticle vehicles. The use of nanoparticles for transdermal drug delivery becomes an important and timely research topic. These questions converge into an investigative task to assess the ZnO-nano, TiO<sub>2</sub>-nano and Qdots transdermal penetrability. Optical properties of sunscreen nanoparticles play an important role in this study, especially considering the recent finding on ZnO-nano high visibility on skin autofluorescence background, which will be addressed in this Chapter.

It has been recently found that the zinc oxide structure is efficiently excited via a nonlinear optical process of simultaneous absorption of two- or three-photons under illumination by an ultrashort-pulse laser (Dai, 2005), which is FMM. This shifts the ZnO-nano excitation band to the infrared (IR) range, where the ultrashort-pulse laser sources predominantly operate, falling into the so-called therapeutic window, 600 nm – 1400 nm, as mentioned in the literature

review. TiO<sub>2</sub>-nano is low-quantum-yield nanomaterial that is transparent in the broad spectral range from the near-IR through to UVA, due to its indirect wide electronic bandgap of 3.21 - 3.4 eV (Lei, 2005). In order to visualise this nanomaterial under FMM, it needs to be labelled with a fluorescent dye, such as pyrene. Results of ZnO-nano and TiO<sub>2</sub>-nano *in vivo* and *in vitro* imaging in skin will be presented in this Chapter to show that FMM is an effective tool for imaging nanoparticle penetration in tissue. Qdots fluorescence is typically bright, with a high, close to unity, quantum yield and it is easy to be imaged under traditional FCSM. Results on the Qdots penetration through skin will be primarily presented in Chapter 3. Owing to its high resolution, SEM/EDS can provide accurate information on nanoparticle size distribution following nanoparticle topical application on skin, and also the localisation in deeper skin layers. This is very useful to confirm the size scale of the absorbed nanoparticles and their penetration in skin. The size determination results will be shown in this Chapter and more detailed results about nanoparticles distribution in skin will be addressed in Chapter 3. Due to these nanoparticles importance for this study, in the next sub-sections, a rather extensive review of their material, physical, and optical properties, followed by presentation of results of their transdermal penetration imaging using novel imaging techniques will be provided. Particular attention will be paid to metal oxide nanoparticles, such as ZnO-nano and TiO<sub>2</sub>-nano, due to their widespread using in cosmetic formulations (sunscreens), and their environmental impact concerns recently raised in the broad scientific and public communities.

## **2.2 Nanoparticles: ZnO-nano, TiO<sub>2</sub>-nano, and Qdots**

### **2.2.1 Physical properties**

#### **2.2.1.1 Basic material property**

##### **ZnO-nano**

Zinc oxide is a natural source pigmented mineral, quarry mined and further refined to a fluffy white powder. Zinc oxide has a hexagonal wurtzite crystal structure, with lattice parameters  $a = 0.3296$  and  $c = 0.52065$  nm. This structure is simply described as a number of alternating planes composed of tetrahedrally coordinated O<sup>2-</sup> and Zn<sup>2+</sup> ions, stacked alternately along the c-axis (see Fig 16). The lack of a centre of symmetry in wurtzite results in strong piezoelectric and pyroelectric properties. ZnO-nano wurtzite crystal has the so-called polar surfaces, primarily represented by the basal plane. The oppositely charged ions produce positively charged Zn<sup>+</sup> (0001) and negatively charged O<sup>-</sup> (000 $\bar{1}$ ) surfaces, resulting in a normal dipole moment and spontaneous polarization along the c-axis. This property determines a broad range of nanoparticle morphologies. ZnO-nano is transparent to visible light and can be made highly conductive by doping. Due to this material versatility, its production allows a diverse



group of growth morphologies, such as nanocombs, nanorings, nanohelices/nanosprings, nanobelts, nanowires and nanocages, with the linear size  $> 3$  nm (Cheng, 2006; Dunford, 1997; Wang, 2006). Nanobelts represent one of the peculiar nanostructures attainable with ZnO-nano. Nanobelts are nanowires that have a well-defined geometrical shape and side surfaces. Each nanobelt has a uniform width along its entire length and the typical widths of the nanobelts are in the range of 50 to 300 nm and thicknesses are 10 to 30 nm (Pan, 2001). Study of one-dimensional nanomaterials has become a leading edge in nanotechnology. With reduction in size, novel electrical, mechanical, chemical and optical properties are introduced, which are largely believed to be the result of surface and quantum confinement effects. Referring to the example of the ZnO-nano nanobelts, the dramatic width reduction from 200 to 6 nm, resulted in a dramatic increase of the electronic bandgap structure (Wang, 2006).

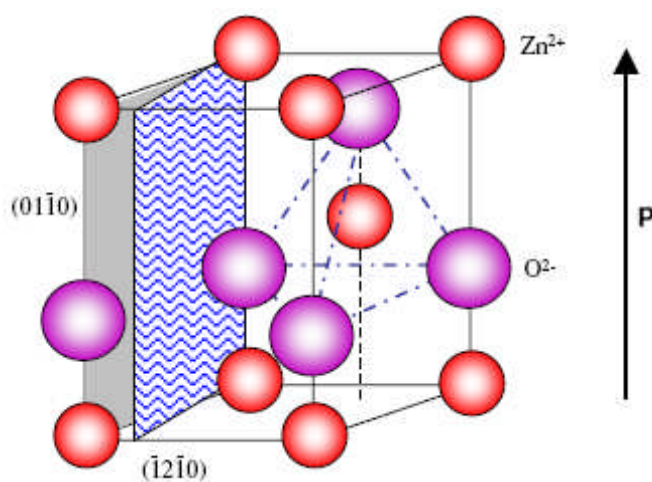


Fig 16. Schematic diagrams of: the wurtzite structure model of ZnO-nano (the tetrahedral coordination of Zn–O is shown) (Wang, 2006)

### **TiO<sub>2</sub>-nano**

TiO<sub>2</sub>-nano bulk crystal exists in two main crystal phases: anatase or rutile featuring octahedral Ti sites, as shown in Fig 17. This bulk crystal structure is retained until the crystal size is reduced to 2 nm, where significant lattice distortions transform octahedral Ti. The distortions in the TiO<sub>2</sub>-nano lattice were mainly located on the surface of the nanoparticles and were responsible for binding with other small molecules. For equally sized nanoparticles, anatase was thermodynamically stable for sizes  $< 11$  nm; brookite (another crystal phase) was stable for sizes between 11 and 35 nm; and rutile was stable for sizes  $> 35$  nm (Zhang, 2006), the latter being the most stable at high temperatures.

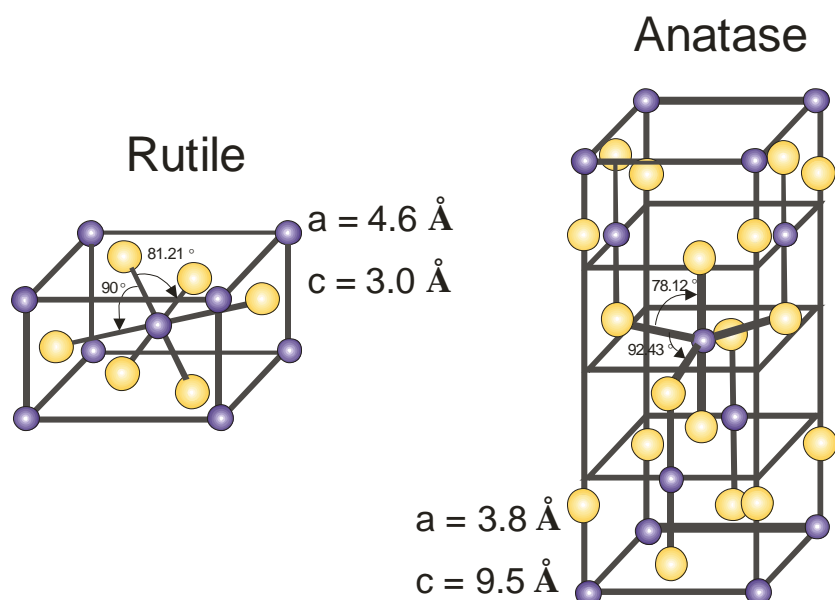


Fig 17. The rutile/anatase TiO<sub>2</sub>—nano crystal structures (Linsebigler, 1995)

### Qdots

Qdot nanocrystals are nanometre-scale (roughly protein-sized) atom clusters comprising a core, shell, and coating (see Fig 18). The core is made up of a few hundred to a few thousand atoms of a semiconductor material (often cadmium mixed with selenium or tellurium: Cd core). A semiconductor shell (typically zinc sulphide: ZnS) surrounds and stabilizes the core, improving both the optical and physical properties of the material. An amphiphilic polymer coating then encases this core and shell, providing a water-soluble surface that Qdots nanocrystals can be differentially modified to meet specific assay requirements. This amphiphilic inner coating is covalently modified with a functionalized polyethylene glycol (PEG) outer coating, grafted with carboxylic acid groups or amine groups. In aqueous solution Qdots with a Cd core can produce free radicals upon UV irradiation, depending on their constitutive material. However, ZnS shell can prevent free radical generation and thus keep coating intact and prevent any leaking or contact between the metallic core/shell structure and the environment. Therefore, the surface modification, (the coating) would probably be responsible for any toxic effect observed (Ipe, 2005).

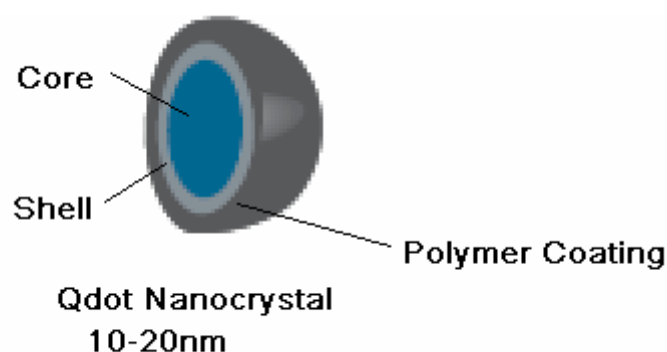


Fig 18. Qdots nanocrystal structure (Invitrogen)

### 2.2.1.2 Crystal electronic structure

Qdots, ZnO-nano and TiO<sub>2</sub>-nano are all semiconductors. Semiconductor electronic structure represents a filled valence band, empty conduction band, and void region (called bandgap), which extends from the top of the filled valence band to bottom of the vacant conduction band (see Fig 19). The absorption of a photon, with the energy in excess of that of the bandgap width, separates charges in the semiconductor crystal in a form of an electron in conduction band, and a hole in the valence band. After nanoparticle absorbs impinging photons with energies equal to or higher than its band gap,  $E_b$  electrons are excited from the valence band into the unoccupied conduction band, leading to excited electrons in the conduction band and positive holes in the valence band. These charge carriers can recombine, non-radioactively or radioactively (dissipating the input energy as heat), or get trapped and react with electron donors or acceptors adsorbed on the surface of the photocatalyst. The electron can recombine with the hole in the bulk or on the surface, emitting the excess of energy as a photon; or via dissipating the energy excess into heat, mediated by phonons. Electron-hole recombination is 90% complete within 10 ns, whereas 10% of the trapped holes mediate photocatalytic chemistry of TiO<sub>2</sub>-nano (Serpone, 1995). Alternatively, the electron or the hole can be trapped in the bulk of surface crystal defect sites. These trapping sites are characterised by energy states that are typically situated below the conduction band (shallow defects), as a variety of crystal oxygen defects in TiO<sub>2</sub>-nano, or above the valence band (deep defects), as a dominant oxygen defect in ZnO-nano. Once trapped, they form excitonic states, with a possibility to eventually recombine, the process is characterised by a lifetime ranging from picoseconds, typically nanoseconds.

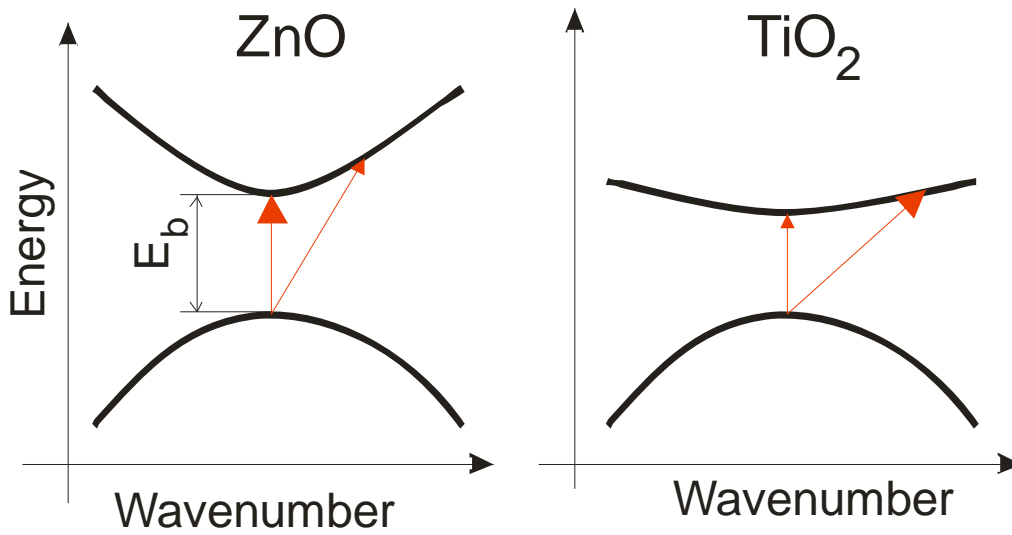


Fig 19. Energy diagrams of ZnO-nano and TiO<sub>2</sub>-nano. Direct transitions are allowed in ZnO-nano, as represented by a large arrow head that designates a principle excitation channel. Direct transitions are forbidden in TiO<sub>2</sub>-nano. In order to break this selection rule, a transition “valence – conduction band” must be accompanied by a phonon (surface polariton) that carries an excess of momentum. This principle excitation channel in TiO<sub>2</sub>-nano is shown by an oblique large-head arrow

### 2.2.1.3 Bandgap configuration

Qdots are new functional materials whose main optical properties are governed by the quantum-mechanical confinement effect. For Qdots, the size of the bandgap is controlled simply by adjusting the size of the dot. Both TiO<sub>2</sub>-nano and ZnO-nano are broad bandgap semiconductors, with the bandgap width of 3.0 eV and 3.37 eV at room temperature, respectively. The interband transition is allowed in ZnO-nano (direct) and symmetry-forbidden in TiO<sub>2</sub>-nano (indirect), which represents the principle difference between these materials (see Fig 19). In contrast to TiO<sub>2</sub>-nano, the ZnO-nano bandgap transitions are direct because the momentum that the electron obtains from the light wave is small in comparison with  $\pi\eta/a$ , where  $a$  is the lattice constant,  $\eta$  is the Plank’s constant. ZnO-nano properties are very close to those of widely recognized semiconductor GaN, with the band gap close to that of GaN (3.39 eV). At the same time, ZnO-nano exciton binding energy (60 meV) is twice larger than that of GaN (28 meV), and far exceeds the thermal energy at room temperature. This affords lowering of the lasing threshold placing zinc oxide in the list of very attractive materials for UV laser applications. In bulk TiO<sub>2</sub>-nano, the absorption is weak across the bandgap (3.0 eV), thus rendering TiO<sub>2</sub>-nano crystal transparent in visible (see Fig 20). Its indirect interband transition demands an additional photon momentum into the system for the absorption to occur, as schematically shown in Fig 19. The possibility of indirect electron transitions there can result in the essential enhancement of light absorption. This means that

considerable enhancement of the absorption can be observed in small nanocrystals, where the share of the interface atoms is sufficiently large. This interface mechanism of light absorption should be most pronounced in  $\text{TiO}_2$ -nano. The interface absorption becomes the main mechanism of light absorption for the crystallites that are smaller than 20 nm. It has been shown that a surface polariton can carry the momentum excess necessary for the interband transition to take place, as shown in Fig 20 by a solid line (squares). Since the conduction band is very shallow in  $\text{TiO}_2$ -nano, it possesses a high density of electrons states, thus affording high absorption probability at photon energy greater than  $E_b$ , as long as the momentum conservation is satisfied (Braginsky and Shklover, 1999). This model explains high absorption efficiency of  $\text{ZnO}$ -nano in the UVA range (340 – 400 nm), whereas the  $\text{TiO}_2$ -nano absorption spectrum is shifted to UVB (320 nm - 290 nm) spectral range, despite the fact  $E_b(\text{TiO}_2\text{-nano}) < E_b(\text{ZnO-nano})$ , as shown in Fig 20.

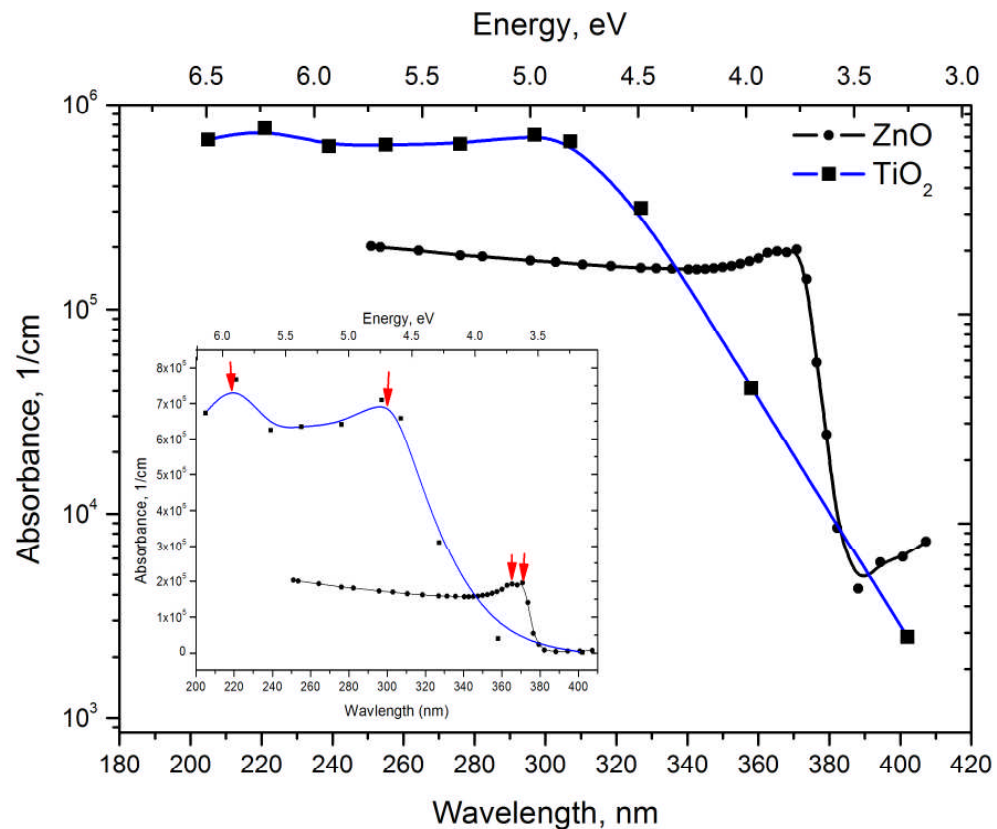


Fig 20. Absorption coefficient of bulk  $\text{ZnO}$ -nano and  $\text{TiO}_2$ -nano at room temperature, plotted in log scale (linear scale, Inset). Data for  $\text{ZnO}$ -nano and  $\text{TiO}_2$ -nano are adopted from (Muth, 1999), and (Palik, 1985; Vos and Krusemeyer, 1977). For  $\text{TiO}_2$ -nano, a single data point at 326 nm (3.81 eV) has been experimentally confirmed by Silva (Silva, 2004). Note the two excitonic bands are marked by arrows in each absorption curve (Inset)

ZnO-nano emission typically occurs in three major spectral bands centred at 385 nm (UV), 530 nm (green), and 590 nm (orange). The orange emission is broadband, and is due to oxygen interstitials defects, which disappear after high-temperature annealing in air (Lin, 2005). Although the origin of the green broadband emission is not well understood, it is commonly believed to originate from oxygen vacancy defects. These defects may be situated on the surface of a ZnO-nano, and hence amenable to surface treatment by capping with polymer (Dong, 2005). Although it has been demonstrated that the surface capping resulted in considerable suppression of the broadband emission in green (accompanied by the UV emission enhancement) several other capping-free ZnO-nano synthetic routes have been reported to yield similar results (Lin, 2005; Demir, 2006). The data for the decay of the UV emission suggest, on the other hand, that its lifetime is less than 100 ps and probably even less than 50 ps (rise time of the photomultiplier employed in this study) in the sol phase (Banhemann, 1987). The green and orange defects exhibit much longer PL lifetime,  $\tau$ . For example, the green defect of ZnO-nano in the aqueous suspension showed that 84% of the intensity decays with a characteristic time of 14 ns and the remainder with  $\tau = 140$  ns (Banhemann, 1987). As accepted in the literature, the narrowband UV emission at 385 nm is unlikely to be due to the direct band gap transition, as the Stock's shift between the absorption and emission bands is too large. It is hypothesized and corroborated experimentally that the UV emission is due to deep donors associated with the oxygen vacancies. A PL-induced electron populates this vacancy followed immediately by its recombination with an available hole (exciton recombination) accompanied by an UV-photon emission. These donors are localized and their population density in the nanocrystal is high leading to dramatic enhancement of the quantum confinement effect and enhanced UV emission.

As the size of a semiconductor nanoparticle falls below the Bohr radius of the first excitation state or becomes comparable to the de Broglie wavelength of the charge carriers, the charge carriers begin to behave quantum mechanically and the charge confinement leads to a series of discrete electronic states. One manifestation of the quantum confinement effect is the band gap energy increase, which results in a blue shift of the PL spectral peak. For example, a small blue shift of the PL spectral peak was observed for TiO<sub>2</sub>-nano sized ~2 nm, the size comparable with the Bohr radius of TiO<sub>2</sub>-nano (1.5 nm) (Li, 2004). A blue shift of 0.15 eV relative to the bulk anatase TiO<sub>2</sub>-nano (3.2 eV) was observed by Pa, reporting the PL of TiO<sub>2</sub>-nano mean-sized 4.7 nm (Pan, 2005). Generally, the TiO<sub>2</sub>-nano quantum confinement effects were difficult to observe due to the indirect interband transition resulting in weak PL signals.

#### 2.2.1.4 Biototoxicity

Both TiO<sub>2</sub>-nano and ZnO-nano are aggressive in degrading organic species in solutions. This catalytic property was known for long time, and was used, for example, for disinfection. Since the discovery of TiO<sub>2</sub>-catalysed photolysis of water (Fujishima and Honda, 1972), applications of TiO<sub>2</sub>-nano in aqueous media clean up have become widespread, surpassing performance of the organic clean up compounds, e.g. chlorophorm, benzene, toluene – all possible clean-up routes like microbial degradation, direct photo degradation or even hydrolysis are painfully slow on these compounds. As discussed earlier in this review, TiO<sub>2</sub>-nano generates high-energy surface-trapped electrons and holes following absorption of a substantial amount of UV radiation. The trapped holes directly oxidize adsorbate molecules, or react with surface hydroxyl groups to produce hydroxyl radicals which are strong oxidizing agents (Draper and Fox, 1990). In aqueous media, surface-trapped holes lead to the production of reactive oxygen species, including superoxide anion radicals, hydrogen peroxide, free hydroxyl radicals, and singlet oxygen. Ti-associated surface defects exhibit not only the acid-base properties of most metal oxides, but also oxidation-reduction reactivities. The deoxygenation of alcohols, carboxylic acids, ketons and aldehydes has been observed (Linsebigler, 1995). This is particularly true for the adsorption of oxygen-containing organic molecules which commonly undergo dehydration, dehydrogenation, deoxygenation, and self-disproportionation reactions. Among the two materials, the photostability issue of ZnO-nano makes TiO<sub>2</sub>-nano more preferable agent for practical applications. For example, the toxicity of the treated solution was reduced only in the presence of TiO<sub>2</sub>-nano, while ZnO-nano suspensions appear to increase the toxicity due to photo-dissolution of ZnO-nano releasing zinc in the treated solution (Evgenidou, 2007). At the same time, Hariharan argued that the ZnO-nano served as a better catalytic system compared to bulk ZnO-nano and commercially available Degussa TiO<sub>2</sub>-nano in achieving degradation of the added contaminants (Hariharan, 2006).

The aggressive surface chemical reactivity also leads to toxic and cytotoxic effects. The reactive oxygen species can cause substantial damage to DNA (Buzea, 2007). Overall, illumination seemed to enhance the antibacterial activity of TiO<sub>2</sub>-nano but not ZnO-nano or SiO<sub>2</sub> (Adams 2006). The greater inhibition in the presence of light supports the notion that the antibacterial activity of TiO<sub>2</sub>-nano was related to photocatalytic ROS production. At the same time, a controversial subject is the toxicity of TiO<sub>2</sub>-nano in cosmetic formulations. Reports regarding the toxicity of TiO<sub>2</sub>-nano in the absence of UV radiation are contradictory. Nanoparticles were seen to have no inflammatory effect or genotoxicity in rats when

introduced by instillation (Rehn, 2003). However, several other studies reported that TiO<sub>2</sub>-nano caused chronic pulmonary inflammation in rats again by instillation (Oberdorster, 2005), and *in vitro* had a proinflammatory effect in cultured human endothelial cells (Eisinger, 1986). Similar results have been reported from mammalian cytotoxicity studies, where TiO<sub>2</sub>-nano exerted oxidative stress in the dark under non-photocatalytic conditions. In order to mitigate potential toxic risks of sunscreen nanoparticles, ZnO-nano and TiO<sub>2</sub>-nano are passivated with silica (SiO<sub>2</sub>), alumina (Al<sub>2</sub>O<sub>3</sub>), or polymer coating, enabling the compound nanoparticles to be used in formulations containing charged organic moieties. One example of such polymer surface treatment is comprised of a star-graft siloxane copolymer containing looped structures (Brotzman, 2000).

It has been demonstrated that a cellular uptake of the Qdots depended on their surface functional groups (Chang, 2006; Ryman-Rasmussen, 2007). There is no doubt that plane Qdots are toxic under normal circumstances (Duan and Nie, 2007; Ryman-Rasmussen, 2007). It has been reported that exposure of skin to commercially available Qdots, differing in core/shell shape, hydrodynamic size, and surface coatings resulted in the penetration of the intact stratum corneum barrier with localization of Qdots in the underlying epidermal and dermal layers as early as 8 hours after topical application. This indicated that skin is a potential route of exposure to Qdots (Ryman-Rasmussen, 2006).

### **2.2.2 Optical properties**

ZnO-nano demonstrates superior protection compared to TiO<sub>2</sub>-nano in the UV spectrum between 340 and 380 nm (Pinnell, 2000). It is obvious in hindsight by examining Fig 20 that shows a rapid onset of absorption of ZnO-nano at 380 nm, where the TiO<sub>2</sub>-nano absorption onset is at 380 nm and reaches its full efficiency at 310 nm. Qdots are extremely efficient fluorescent materials. Contrary to organic fluorescent dyes, Qdots absorption band is broad extending well into the UV range, in addition to a characteristic size-dependent narrow-band absorption peak, which often occurs in the visible range.

### **ZnO-nano**

Material illumination with a femto-second laser radiation results in enormous instantaneous intensity in the femto-liter focal volume that elicits the material nonlinear optical response. Two-photon excited fluorescence (TPEF) is one manifestation of this nonlinear process. The fluorescence emission is localized exclusively within the focal volume resulting in the inherent “optical sectioning” property of FMM (König, 2006).



ZnO-nano has been found to be efficiently excited via a nonlinear optical process of simultaneous absorption of two- or three-photons under illumination by an ultrashort-pulse laser (Dai, 2005) (see Fig 21). Infrared range excitation is now used to excite ZnO-nano via simultaneous absorption of two photons, as a result of the non-linear process, which is 600 nm – 1400 nm instead of UV spectral range, wherein the imaging penetration depth in tissue of ~200  $\mu\text{m}$  is attainable. It is due to the markedly reduced absorption of the major tissue constituents, including proteins, haemoglobin, and melanin in the UV/visible spectral range, and the water transparency window. Also, the scattering efficiency of skin tissue is reduced at longer wavelengths.

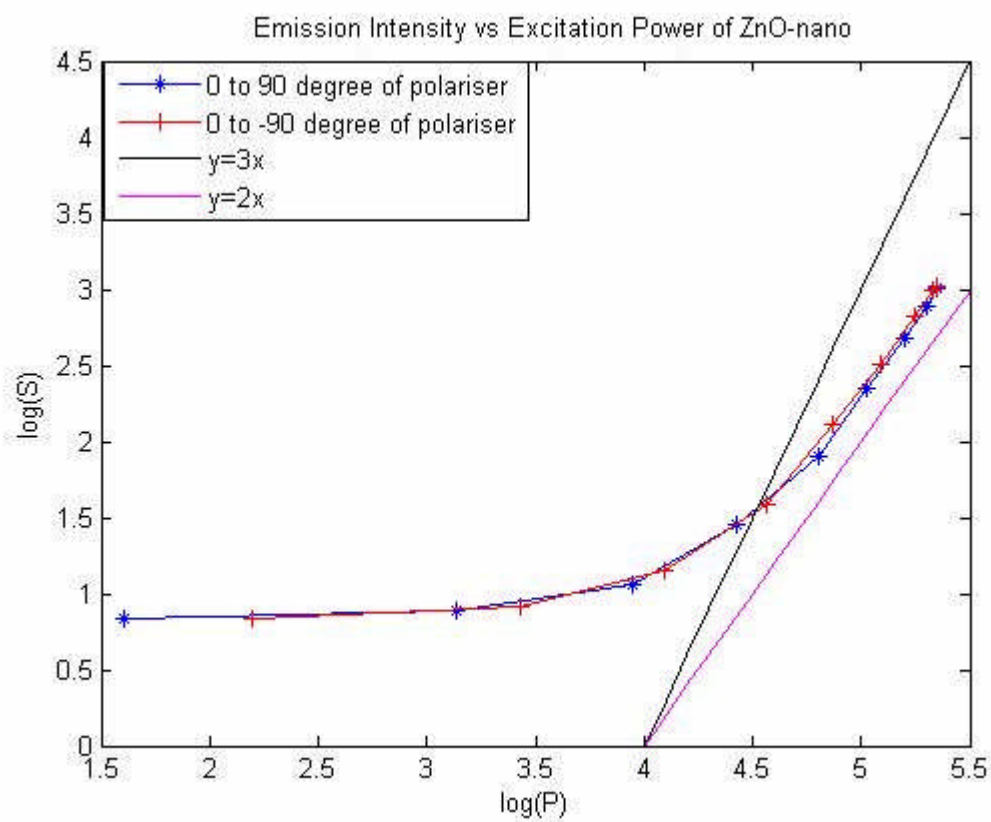


Fig 21. Emission intensity vs excitation power of ZnO-nano by FMM: Excitation wavelength 800nm; log(S), the logarithm of emission intensity; log (P), the logarithm of excitation power

As shown in Fig 21, the excitation power was changed by a polariser. The power increased as the angle of polariser changed from 0 degree to 90 degree clockwise or 0 degree to negative 90 degree anticlockwise. These two sets of data were acquired to make a confirmation. The curve of logarithm showed the potential of two- or three-photon absorption (Emission intensity=Excitation power<sup>2 or 3</sup>; log(Emission intensity)=2 or 3 \* log(Excitation power)) by comparing the shape of this curve to a “y=2x” or “y=3x” line. The results showed that ZnO-nano was efficiently excited by 800-nm and more like two-photon absorption.

## **TiO<sub>2</sub>-nano**

Optical imaging of TiO<sub>2</sub>-nano in skin is difficult, and requires either more efficient excitation sources, e.g. x-ray source (Nohynek, 2007), that largely precludes *in vivo* measurements; or labelling TiO<sub>2</sub>-nano with an optically bright agent. It has been resorted to explore the second approach by labelling SiO<sub>2</sub>-capped TiO<sub>2</sub>-nano with fluorescent organic dye, pyrene (WA 18698, Fluka).

## **Qdots**

Qdot nanocrystals are extremely efficient materials for generating fluorescence. Their intrinsic brightness is often many times that observed for traditional organic fluorophores, and their photostability is many orders of magnitude greater than that of organic dye fluorophores. These extraordinary fluorescence properties can be attributed to the unique fluorescence mechanism of semiconductor materials. Unlike organic fluorophores, Qdot nanocrystals fluoresce through the formation of excitons, or Coulomb-correlated electron–hole pairs, upon absorption of a photon of light. Importantly, these excitons are quantum-confined within the nanocrystal whose size is comparable with the Bohr's radius. Compared with the excited state of a fluorophore, this exciton typically exhibits a much longer lifetime (up to ~200 nanoseconds), a property that can be advantageous in certain types of time gated detection studies.

### **2.2.3 Summary of ZnO-nano, TiO<sub>2</sub> -nano, and Qdots optical/spectroscopic properties**

As mentioned in Sub-Section 1.6.2, a femtosecond pulsed laser in FMM is tuned to a wavelength twice that of the targeted absorption wavelength of the fluorophores for excitation. Therefore, the fluorophores can be excited by twice the wavelength of their excitation band in the single-photon excitation scheme. As mentioned in Sub-Section 1.5.1.2, TiO<sub>2</sub>-nano was labelled with a fluorescence dye, pyrene, with excitation range 300 – 400 nm. Its two-photon excitation wavelength is < 800 nm, in FMM.

Tabulated data on the relevant optical/spectroscopic properties of the nanoparticles used in the imaging and characterisation experiments are summarised in Table 4.

**Table 4. Nanoparticles used in experiments**

	Size, nm	Surface functional group	PL excitation band (Two-photon excitation band /two-photon cross section), nm/GM	PL emission band, nm	Supplier
<b>ZnO-nano</b>	26-30		310-360 (700-920/12)	377(experimental measurement) 395, 492 (Dai, 2005)	Advanced Nano Technology
<b>TiO<sub>2</sub>-nano/ pyrene</b>	14		300-400 (720-800)	373	Kemira
<b>Qdots</b>	14-35	Carboxylic; Amine; PEG	488, UV	565	Invitrogen

## 2.3 Optical and electronic techniques

### 2.3.1 FMM setup

Three instruments were used in this study: 1. originally, an in-house built instrument on a platform of the FCSM (Fluo, Olympus) was used to carry out preliminary experiments and Qdots characterisation. This instrument was located in Physics, University of Queensland (UQ), supervised by Prof Halina Rubinsztein-Dunlop, and allowed considerable flexibility in its reconfiguration. 2. A FMM based on Zeiss 510 (Zeiss, Germany) system was recognised to allow greater flexibility in handling a broad range of samples. It was located in the Australian Institute of Bioengineering and Nanotechnology (AIBN), UQ, supervised by Prof Mark Kendal. This instrument featured a lateral resolution of 200 nm. It was most useful for *in vitro* imaging. 3. The unique *in vivo* imaging capabilities, also with *in vitro* imaging capabilities were enabled by the FMM (DermaInspect, JenLab, Germany) located in School of Medicine, UQ, Princess Alexander Hospital, supervised by Prof Michael Roberts. This system also featured four high-speed PMTs and Time-correlated single-photon counting module (TCSPC) (Becker and Hickl, Berlin, Germany), allowing extra-capabilities of FLIM. The DermaInspect and Zeiss 510 system were both operated in combination with Mai Tai XF-1 ultrafast pulsed laser with tuning range of 710 to 920 nm. The shortest pulse width (<100 fs) was achieved at

80-MHz repetition rate resulting in the high instantaneous peak power ( $\sim 100 \text{ GW/cm}^2$ ) at the focal spot. The available average laser power was 1.1 W at a peak wavelength of 800 nm. The Zeiss 510 system also had 488nm Argon-ion laser which was used for FCSM settings and Qdots imaging.

In this study, the excitation wavelength of the femtosecond laser was chosen to be 740 nm, as providing a reasonable trade off in attainable resolution (that depends on a wavelength) and imaging penetration depths (that increases with the wavelength in the “therapeutic spectral window”). ZnO-nano was found to be efficiently excited at this wavelength.

A typical experimental configuration employed in the DermaInspect and Zeiss 510 FMM imaging system is diagrammatically shown in Fig 22. In the simplest case scenario, the multiphoton excited fluorescence was collected after passing a dichroic mirror short-pass 700 nm, i.e. light of  $\lambda < 700 \text{ nm}$  is passed through the dichroic mirror, whereas light of  $\lambda > 700 \text{ nm}$  is reflected) and an interference broadband pass filter: BG 39 (UQG Optics Ltd.), which allows light of the spectral band of 300 – 700 nm passing through. The integral fluorescence signal, including the broadband skin autofluorescence and ZnO-nano and TiO<sub>2</sub>-nano/pyrene emission signals are transmitted and registered. This filter’s main function is blocking the excitation light at 740 nm (see Fig 22).

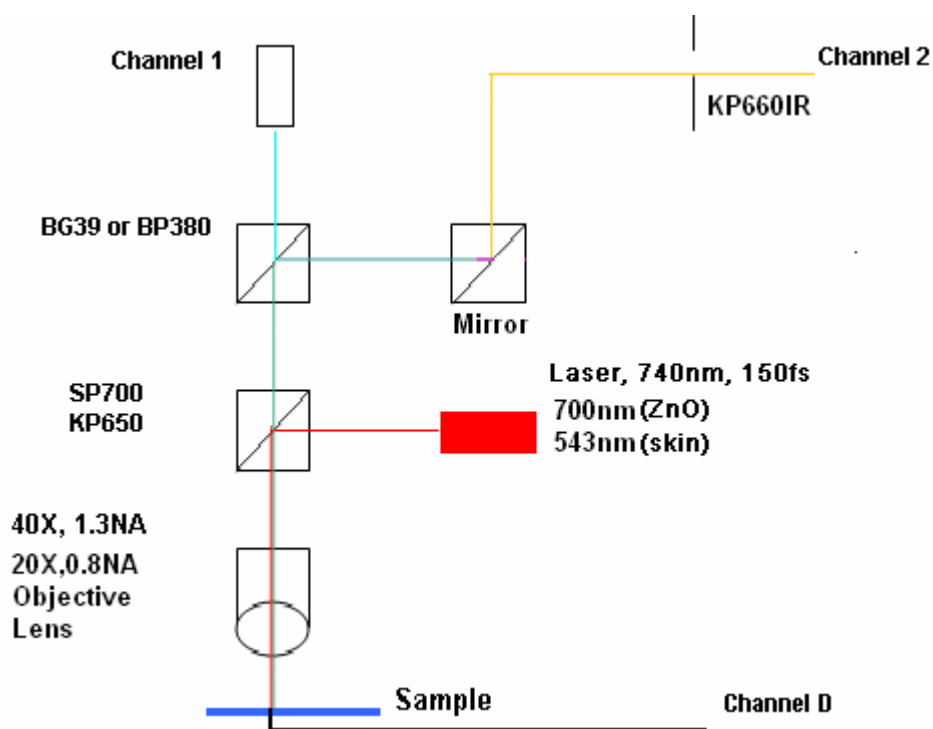


Fig 22. DermalInspect FMM imaging system diagram, with spectral filters configured for ZnO-nano and TiO<sub>2</sub>-nano *in vitro* and *in vivo* study. Channel 1 was for *in vivo* and *in vitro* FMM (DermalInspect); channels 2 and D were for *in vitro* FMM (Zeiss 510); Channel D (below the sample) was used to collect the transmission light from the thin skin sample slices. Channel 2 was used to detect the ZnO-nano fluorescence. 40X, 1.3NA oil immersion objective lens was used in *in vivo* and *in vitro* FMM imaging (DermalInspect) and a 20X, 1.0NA dry objective lens was used for *in vitro* FMM imaging (Zeiss 510).

*In vivo* imaging configuration: Laser radiation from an ultrashort-pulse (femtosecond) laser source at 740 nm was used as the excitation radiation; SP700, a dichroic mirror, which reflects towards the sample light at a wavelength longer than 700 nm. Fluorescence signal in UV/visible spectral range, i.e. < 700 nm, is passed through this dichroic mirror towards an optical detector (not shown); BG39, blue glass filter, transmission 300 - 700 nm; BP380, bandpass filter, transmission, 370 – 390 nm.

*In vitro* imaging configuration: 700 nm (ZnO), ZnO-nano was excited by 700 nm with 4% of the total power 3310 mW, 132 mW; 543 nm (skin), skin was excited with a helium-neon laser at 543-nm with 5% of the total power 1 mW, 0.05 mW; KP650, short-wavelength pass dichroic mirror, cutoff 650 nm; KP660IR, short-wavelength pass cutoff 660 nm

Since the emission peaks of ZnO-nano and pyrene are at 377 nm and 373 nm, respectively, the same filter centred at 380 nm of bandwidth 20 nm was used to filter the ZnO-nano or TiO<sub>2</sub>-nano/pyrene signals from the broadband skin autofluorescence background.

In DermaInspect FMM imaging system, a single high-sensitivity detection channel was used. In order to acquire images in different spectral bands, a set of preselected filters was used for each image acquisition run. The acquired sets of images were overlapped at the post processing stage by using the Matlab commercial software. In Appendix I, more details of the image processing is provided, including Matlab codes. The laser power at the focus was adjusted to obtain an optimum intensity image at each layer of the skin with the maximum power level of 50 mW, which represented the maximum permissible exposure limit set by the Laser Safety Standards (König, 2006).

The Zeiss 510 FMM imaging system was used for cross-sectional imaging of fixed human skin samples treated topically with the ZnO-nano formulation prior to their fixation. These samples were imaged in the framework of nanoparticle transdermal penetration study using the skin models treated with the chemical enhancers detailed in Sub-Section 1.5.1.4. This FMM system provided a convenient alternative to the DermaInspect system, as it permitted greater flexibility for handling samples, and especially searching areas of interest that was critical to the skin models treated with chemical enhancers. In the experiment, the skin samples were fixed implying their treatment with aggressive chemicals, such as formaldehyde. As a result, the significant fraction of the autofluorescence was lost due to the degradation of NAD[P]H, the main contributor to the multiphoton-induced fluorescence. Therefore, a 543-nm helium-neon laser line was used in transmission configuration of FCSM to acquire cross-sectional images of the fixed thin skin samples. In other words, the skin morphology image was an FCSM image, where the effect of confocality was not employed. Since the skin morphology was visible in transmission, the use of a 740 nm ultrashort-pulse laser radiation employed for acquisition of the skin autofluorescence signal was not required. The ultrashort-pulse laser excitation was wavelength-tuned to 700 nm to achieve a greater efficiency for ZnO-nano two- or three- photon excitation.

### **2.3.2 FCSM setup**

In order to validate the results of Qdots penetrability in porcine skin obtained by Ryman-Rasmussen (Ryman-Rasmussen, 2006), a series of experiments were performed. Firstly, the effects of different surface functional groups on the transdermal behaviours of Qdots were examined. The *in vitro* imaging experiments were carried out using the FCSM system that was an integral part of the Zeiss510 imaging system. An argon-ion laser line of 488 nm was chosen for the Qdots excitation. A bandpass filter with the wavelength transmission band of 560-615 nm was chosen to collect the Qdots emission light. Two FCSMs were used

throughout this project. Both of them were of the same model Zeiss 510. At the initial stage of the project, a system available at the Centre for Advanced Laser Microscopy (CALM), UQ was employed. The second system was an integral part of the system located in AIBN, UQ (see Fig 23). Different objective lenses and filters (see corresponding Fig captions) for collecting skin autofluorescence were used.

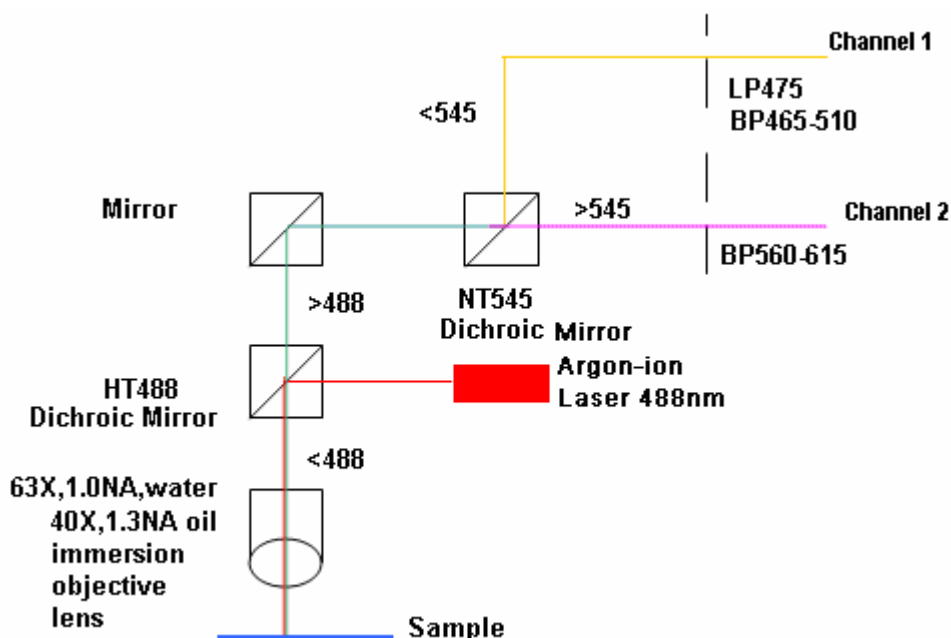


Fig 23. FCSM schematic diagram of CALM and AIBN: 40X, 1.3NA oil-immersion objective lens and LP475 were used in FCSM in CALM; 63X, 1.0NA water-immersion objective lens and BP465-510 were used in FCSM in AIBN. HT 488, dichroic mirror, wavelength cutoff 488 nm: pass  $\lambda > 488$  nm, reflect  $\lambda < 488$  nm; NT545, second dichroic mirror wavelength cutoff 545 nm; LP475, long pass filter, cutoff 475 nm; BP465-510, bandpass filter, transmission 465 to 510 nm; BP560-615, bandpass filter, transmission 560 to 615 nm. Channels 1 and 2 are designed for collection of the skin autofluorescence and Qdot signals, respectively. Argon-ion laser power, 20mW

### 2.3.3 SEM/ EDS setup

In order to perform cross-comparison of FCSM skin images, and further characterise sample atomic species content, two SEM systems were employed: JSM-6300F (Jeol, United Kingdom) and Philips XL30 (Philips, Holland), which had Energy Dispersive Spectroscopy (EDS) function.

Typical operating parameters for JSM-6300F were: working distance 15 mm (10 mm); voltage 5-8 kV; aperture 4 (A parameter which confines the electron beam. The smaller the aperture, the less electron flux reaching the sample, the less charging and damaging, at the expense of signal-to-noise ratio); electron spot size (on the sample) 5 (a parameter, which

measures confinement of the electron beam, and ultimately determines the SEM spatial resolution).

Typical operating parameters for Philips XL30 were: working distance 11.3 mm; voltage 20 kV; aperture 4; spot size 5 or 6. The brightness and contrast was adjusted for each image.

#### **2.3.4 FLIM setup**

FLIM is a powerful tool for producing a map of the fluorescence decay rates of the fluorescent sample. It is often overlaid with the sample morphology image. In similarity to the fluorophore delineation using fluorescence spectral bands in the spectral domain, delineation can also take place in the fluorescence lifetime domain. FLIM has been employed to determine lifetimes of the nanoparticles and skin endogenous fluorophores with resolution of 125 ps (1/80MHz). This was useful when the emission bands of nanoparticles and skin fluorophores were nearly overlapped that made spectral separation inefficient. Lifetime of ZnO-nano is on the scale of ps (Zhang, 2006; Brauer, 2007), while that of the skin fluorophores is on the scale of ns (Hanson, 2002). Also, the skin fluorophore lifetime varies for different skin pH (Hanson, 2002) that is often a manifestation of the tissue diseased state. Hence, FLIM measurement provides a useful discrimination method capable of recognising diseased and normal tissues. Using the FMM imaging capability, one can acquire lifetimes at each pixel, and, eventually, obtain a image 'map' pixel-by-pixel of a fluorophore-containing sample, that is colour-coded. The area of acquisition is 128\*128 pixels.

In FMM-FLIM imaging experiments, two wavelength settings were used, both for the skin autofluorescence and ZnO-nano: 740 nm and 800 nm for skin samples; and 710 nm and 800 nm for ZnO-nano. At 800 nm, the Mai Tai laser power was set to the highest value. This wavelength was used to check whether higher power could give more photon counts. The 710-nm ultrashort pulse laser excitation was used only for the ZnO-nano sample to improve a SNR due to the more efficient excitation at a shorter wavelength. The 740-nm ultrashort pulse laser excitation was used a short-wavelength trade-off for imaging both skin layout and ZnO-nano distribution. In all experiments, the maximum laser power was set to 50 mW. The typical image frame rate was 13.4 seconds per frame. The total integration photon-counting time was 10 s. In the DermaInspect system, four FLIM channels spectrally partitioned into preselected spectral bands were employed, as shown in Fig 24.



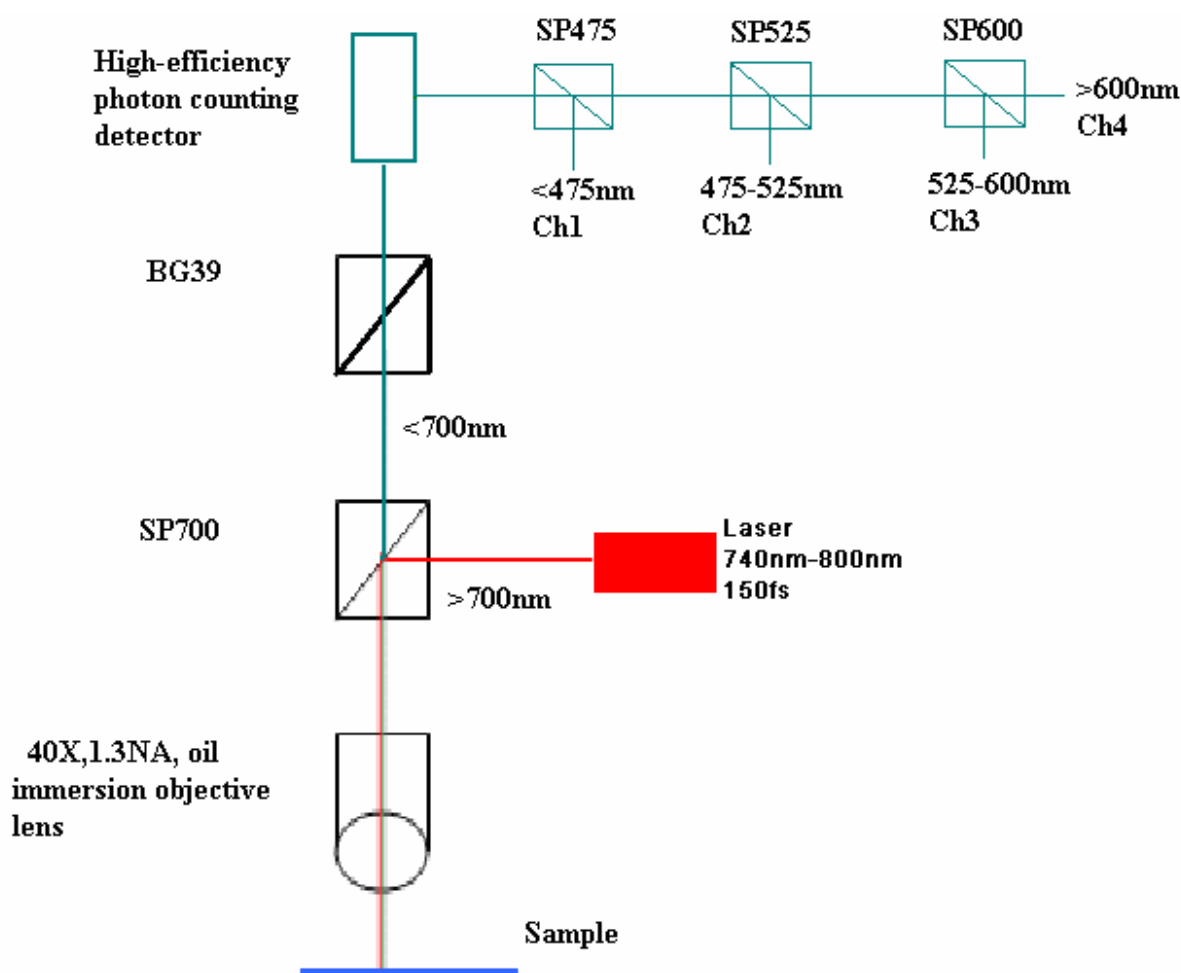


Fig 24. FLIM DermalInspect microscope setting: BG39, blue glass filter, transmission, 300 to 700 nm; SP700, dichroic mirror, cutoff 700 nm;  $\lambda > 700$  nm, light of a wavelength longer than 700 nm;  $\lambda < 700$  nm, light of a wavelength shorter than 700 nm; SP475, shortpass filter, cutoff of 475 nm; SP525, short-pass, cutoff 525 nm; SP600, short-pass filter, cutoff, 600 nm

## 2.4 Sample preparation procedure and methods

### 2.4.1 ZnO-nano SEM size determination

Dr Lewinns' private formula (60% w/w) (Advanced Nanotechnology Ltd., WA, Australia) comprised ZnO particles sized 26 – 30 nm with preservatives of phenoxyethanol (0.3% w/w) and hydroxybenzoates (0.3% w/w) suspended in caprylic capric triglycerides (CCT) (Cross, 2007). These nanoparticles were fabricated by using the mechano-chemical processing technology based on dry milling that induced chemical reactions through ball-powder collisions resulting in nanoparticles formation within a salt matrix. Particle size was determined by the chemistry of the reactant mixture, milling and heat treatment conditions.

ZnO-CCT solution was applied on the skin sample, and incubated for 2 hours. This nanoparticle-treated skin sample was fixed in 2.5% glutaraldehyde solution, a requirement of

the SEM facilities. The fixed skin was cut into small cubical shaped blocks approximately 1 cm<sup>3</sup>, followed by snap freezing with a specially made copper press that has been dipped in liquid nitrogen for 5 minutes. Whilst in the press, the sample was further dipped in liquid nitrogen and then freeze dried. The small freeze dried skin sample were mounted on the SEM and imaged. Before imaging, the sample was platinum coated with 70 nm. Conductive paint was applied to the aluminium stub holder.

#### **2.4.2 ZnO-nano emission spectrum acquisition**

The excitation and emission bands of ZnO-nano were determined by a fluorometer (Fluoromax 4, Jobin Yvonne). ZnO-CCT solution was diluted to nine different concentrations from 0.24% w/w to 0.0015% w/w by CCT solution. For each concentration, the detection of the emission spectrum using 320 nm and 350 nm excitation wavelength was done.

#### **2.4.3 Qdot SEM size determination**

Independent Qdot samples were prepared, as follows: Firstly, a drop of the Qdot carboxyl-pH9 1- $\mu$ M suspension was placed on a silicon wafer. Secondly, the silicon wafer was fixed on a metal stud designed specifically for the SEM imaging. Thirdly, the stud was put in a container sealed by a foil paper, and heated at  $>70^{\circ}$  C for 20 minutes. The following morning, the samples were coated with 20-nm platinum film, followed by imaging using the SEM instrument (JSM6300F).

#### **2.4.4 Qdot emission spectrum acquisition**

Commercially available Qdots from Invitrogen have been procured. They were characterized by an emission band at 565 nm. Three kinds of Qdots had three surface functional coatings: PEG (trademark, Qtracker®), non-targeted Qdots at 2  $\mu$ M concentration in pH8.3 sodium borate buffer; carboxylic Qdots sold as 565 ITK<sup>TM</sup> carboxyl Qdots at 8  $\mu$ M concentration in a pH9 sodium borate buffer; amino-Qdots sold as 565 ITK<sup>TM</sup> amine Qdots at 8  $\mu$ M concentration in a pH8.3 sodium borate buffer. Their hydrodynamic diameters in buffer solution are respectively, 35 nm (PEG), 14 nm (COOH) and 15 nm (NH<sub>2</sub>) (Ryman-Rasmussen, 2006). All Qdots were vortexed before being diluted into a working concentration of 1  $\mu$ M in a borate buffer at the original pH or at pH7, immediately before the experimental use.

The Qdots solution needed to be prepared in a diluted 1- $\mu$ M-concentration before the experiment. It was necessary to confirm that the dilution did not induce nanoparticle aggregation. In the aggregated state, the Qdot energy band changes resulting in the absorption peak shift. The absorption peaks of the diluted and original solutions were measured using a spectrometer (Spectramax M5, Molecular Devices).

#### **2.4.5 ZnO-nano MPM imaging**

In order to optimize the spectral filter configuration in the detection arms, a preliminary imaging experiment using two samples was conducted (Fig 31). Sample 1 represented Dr Lewinns' cosmetic formulation diluted to a concentration of 0.005% w/w and spun-coated on a glass slide to form nanoparticles and clusters. Sample 2 was a skin patch prepared with top application of the same 0.005% w/w ZnO-nano formulation as sample 1. The skin, for this *in vitro* study, was excised abdominal obtained after plastic surgery.

For *in vivo* experiments, an area of 50 cm<sup>2</sup> of skin was selected on the forearm, cheek, shoulder, or feet of the subject and cleaned with ethanol. Approximately, 0.3 g of commercial Dr Lewinns' sun-blocking special formulation was applied evenly to the selected area of the human subjects and rubbed in for 5 minutes. Subsequently, the treated area was non-invasively imaged using the FMM imaging system.

All experiment conducted on human subject were done with approval of Princess Alexandra Hospital Research Committee (Approval No. 097/090, administrated by the University of Queensland Human Ethics Committee). Each subject gave their written consent.

#### **2.4.6 TiO<sub>2</sub>-nano MPM imaging**

Pyrene is soluble in mineral oil. 1% pyrene in mineral oil solution was mixed with TiO<sub>2</sub>-nano in powder state in a glass tube. After they were mixed thoroughly, the glass tube was put vertically overnight. The next day, a top fraction of the solution was collected, and the residue was kept in air until it became paste. This fluorescent TiO<sub>2</sub>-nano/pyrene paste was applied directly on human skin *in vitro*. The skin, for this *in vitro* study, was excised abdominal obtained after plastic surgery.

Excised skin sample images were acquired 15 minutes, 8 hours, and 24 hours following TiO<sub>2</sub>-nano/pyrene formulation topical application. The skin sample was incubated in a 35°C water bath for 8 hours and 24 hours.

## 2.5 Results

### 2.5.1 ZnO-nano SEM size determination

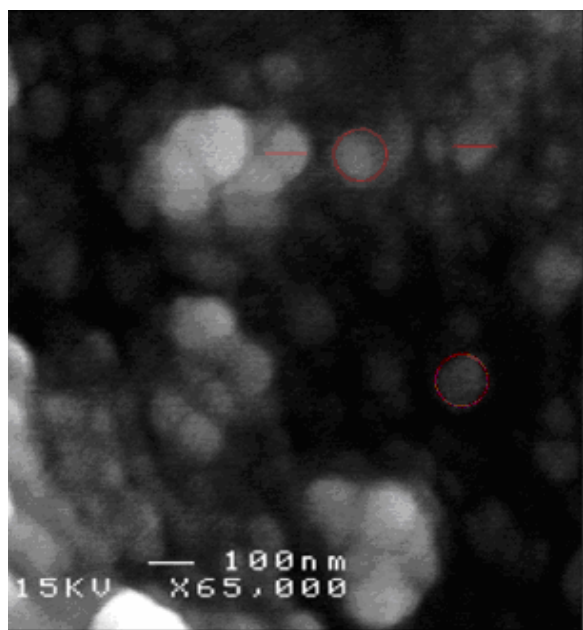


Fig 25. Validation of ZnO-nano size on human skin (30-nm ZnO-nano are coated with 70-nm platinum for imaging). The independent ZnO-nano was pointed out as a red circle in the image

The findings presented in Fig 25 were used to confirm that the mean size for the ZnO-nano was 30 nm. As shown in the image, the ZnO-nano on the skin after platinum coating for 10 minutes is 100 nm. Taking into account the platinum thickness of 70 nm, the core size was determined to be 30 nm.

### 2.5.2 ZnO-nano emission spectrum determination

The results showed that ZnO-nano is characterized by a wide excitation band, centred at a wavelength of 320 nm, and emission band at 377 nm (see Fig 26). Different concentrations of ZnO –CCT solutions have been characterised using the fluorometer, with essentially similar results (see Fig 27). As shown in Fig 27, a slight emission spectral shift to blue at high concentration is due to scattering and self-absorption effect, noted that absorption coefficient of ZnO-nano is roughly  $2 \times 10^5 \text{ cm}^{-1}$ . The higher the concentration is, the more possibility of self-absorption happening and thus the emission light of low wavelength is absorbed by ZnO-

nano itself and emitted at a longer wavelength. As the concentration increases, more ZnO-nano exists in the solution and thus more opportunities of photon-emitting happen when excited. Therefore, more photons can be detected at the same emission wavelength compared with low concentration. This induces a spectrum broadening phenomenon and also emitting intensity increasing. The following results have similarities with the reported data (Monticone, 1998).

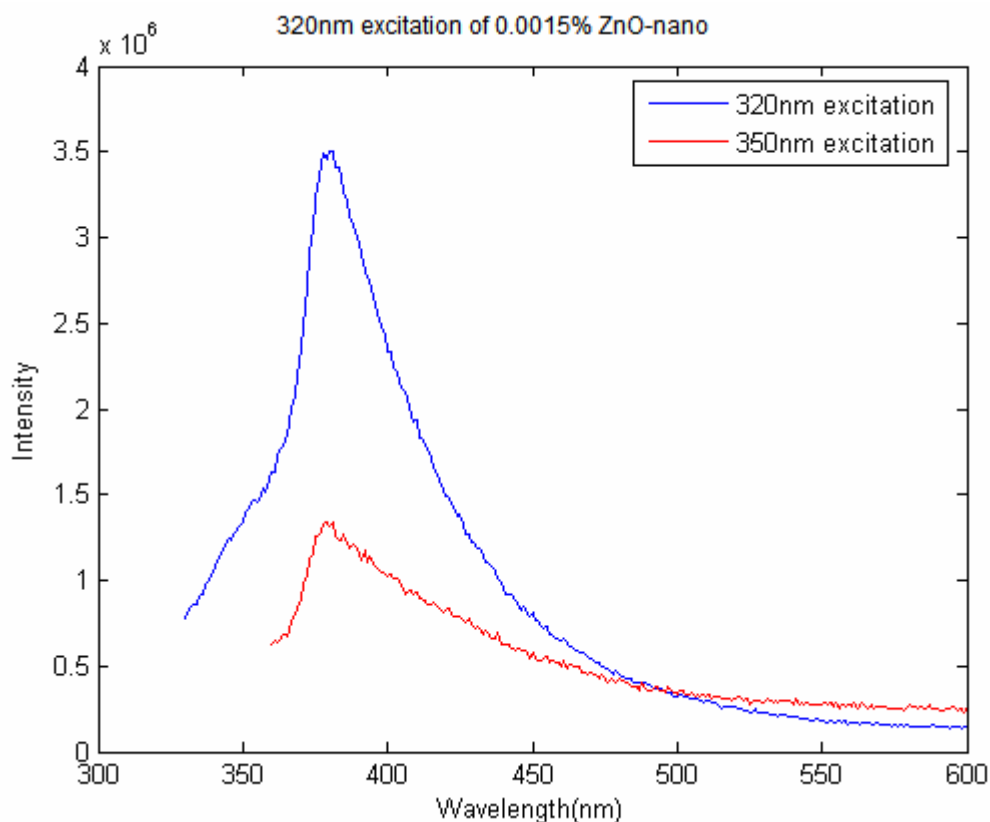


Fig 26. ZnO-nano emission spectrum acquired at different excitation wavelengths. The percentage of ZnO-nano suspending in CCT solution is 0.0015% w/w

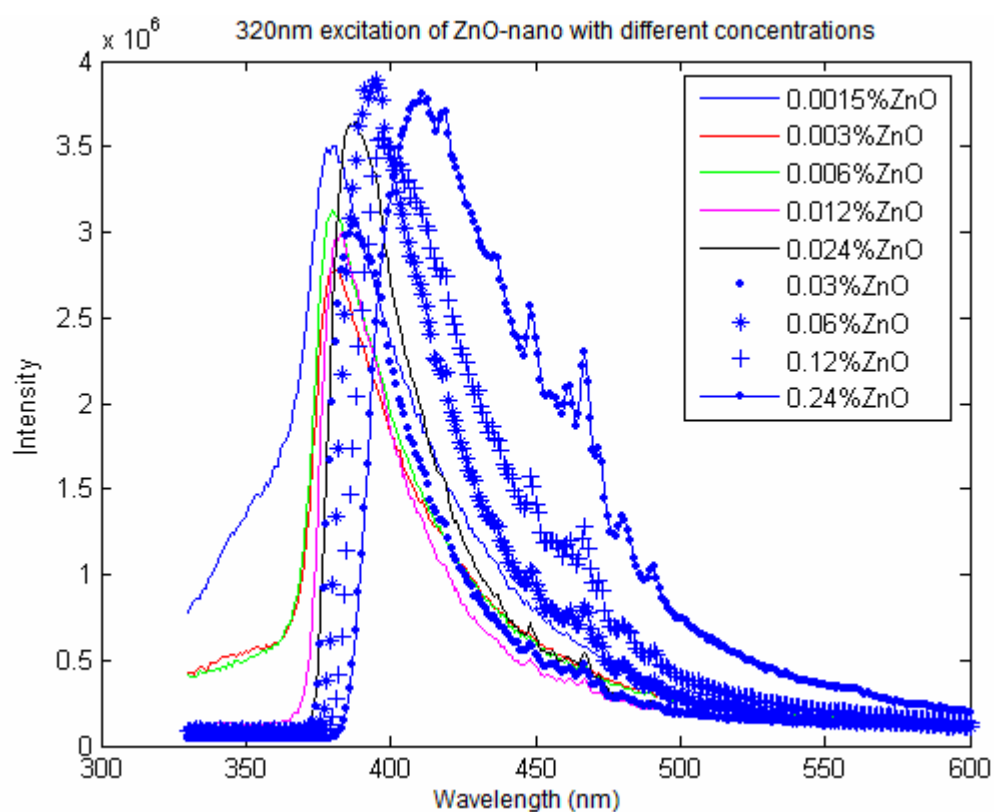


Fig 27. Emission spectra ZnO-nano in CCT at different concentrations; 0.0015% ZnO: the percentage of ZnO-nano suspending in CCT solution is 0.0015% w/w. Note the slight increase of the intensity and the spectrum width as the concentration increase in spite of several abnormal ones, which are 0.0015% and 0.06%.

### 2.5.3 Qdots SEM size determination

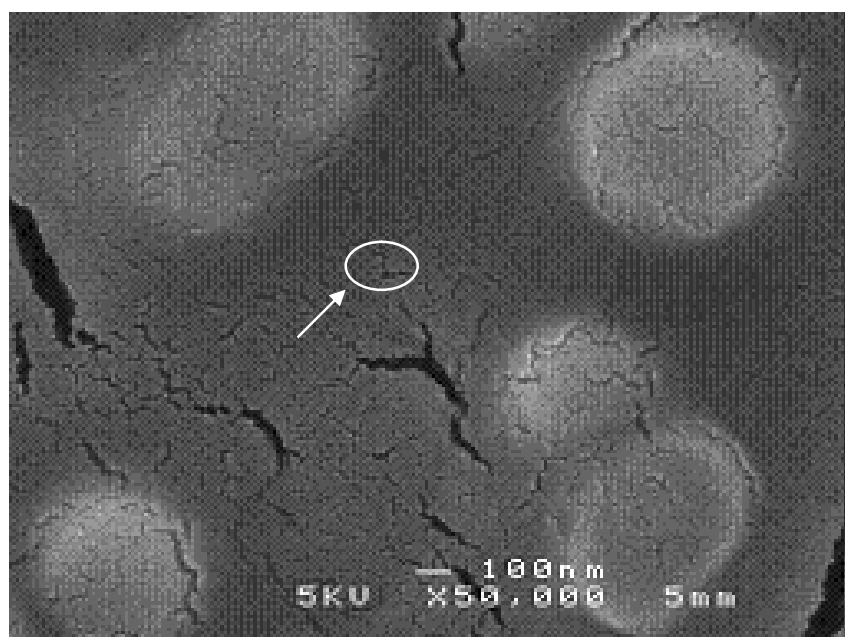


Fig 28. SEM image of Qdots appeared as bright spots (positive contrast), as shown in a white oval pointed by an arrow

From the image, slight aggregation of Qdots can be seen as a result of evaporative condensation of the Qdots in the solvent. The size of the small aggregated group was around 150 nm. The evaporation of the solution is unavoidable and, thus, a random distribution of individual (white oval pointed by an arrow), and aggregated Qdots (several 100-nm bright patterns) ranged in size from 14 to 200 nm.

#### 2.5.4 Qdot emission spectrum acquisition

The measurement results showed that the absorption peak of the four diluted Qdots solutions (amine pH8.3, amine pH7, Carboxylic pH9, and Carboxylic pH7) remained at the same wavelength of 552 nm (see Fig 29), which was the same as original Qdots concentrations and pHs (see Fig 30). From this result, it indicated that the dilution in different pH solutions did not cause aggregation of the Qdots.

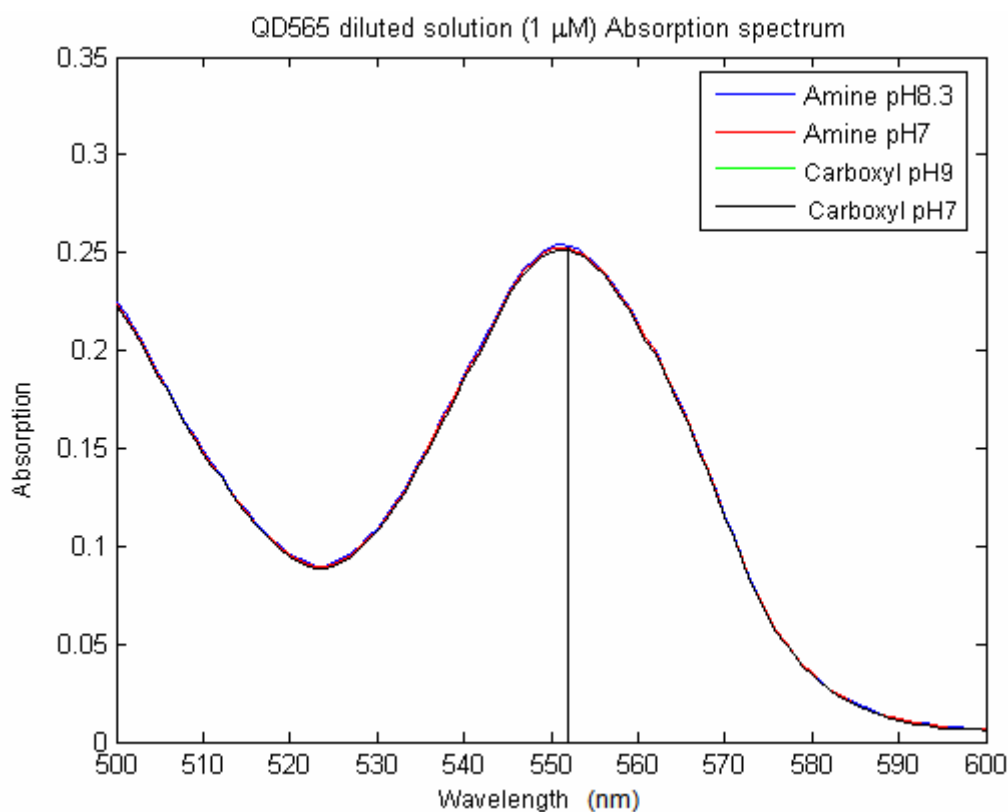


Fig 29. Absorption spectrum of the diluted suspension of Qdots

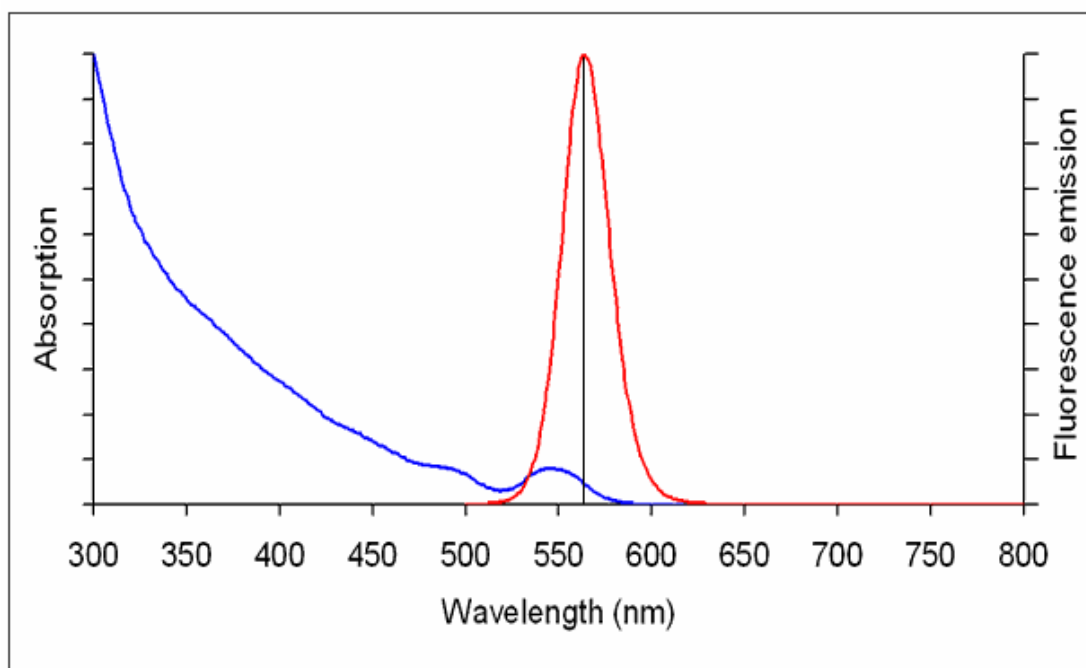


Fig 30. Absorption spectrum of Qdots (original concentration) featuring an absorption peak at 552 nm. (<http://probes.invitrogen.com/servlets/spectra?fileid=QDOTSSA>)

### 2.5.5 ZnO-nano MPM imaging

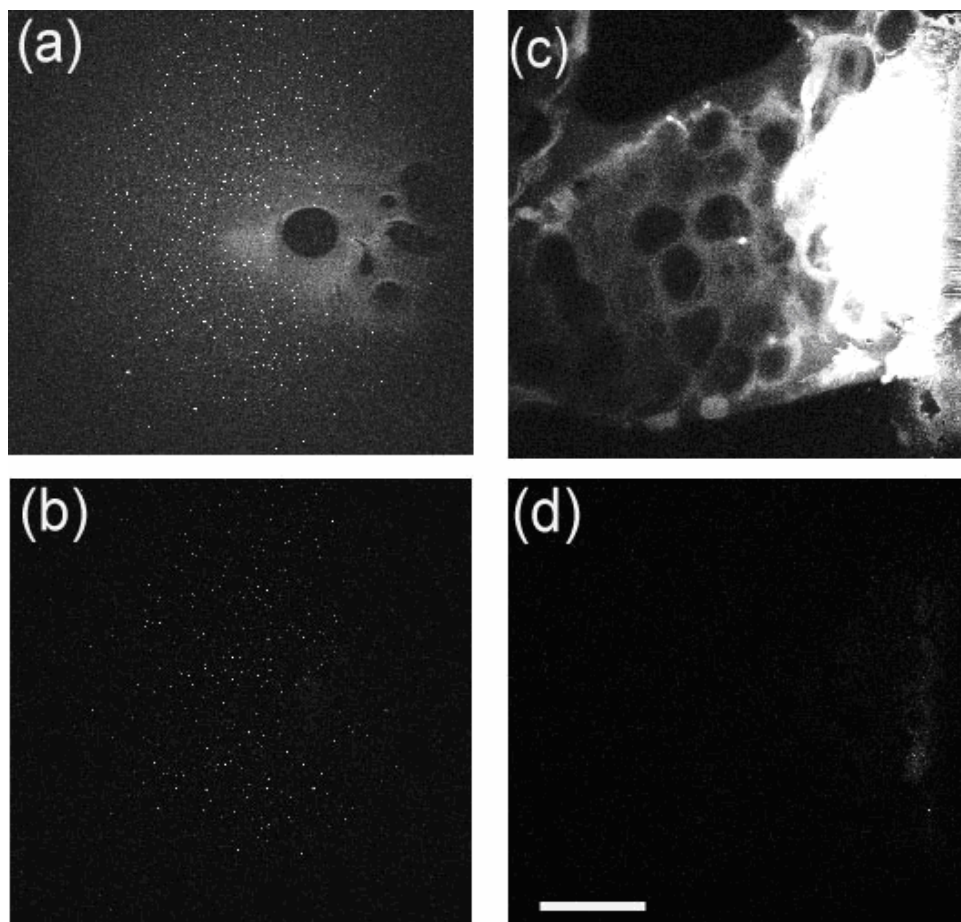


Fig 31. FMM images: (a)-(b), ZnO-nano (scattered bright dots) the capric/caprilic oil film cast on a glass slide; (c)-(d), excised skin patch. Epidermal cellular architecture is clearly observable in (c).



Images (a), (c) and (b), (d) are detected using the broadband BG39: 300 to 700nm transmission (Channel 1) and narrowband BP380: 370 to 390nm transmission (Channel 2) spectral filters, respectively. Scale bar 50  $\mu\text{m}$

The results of FMM imaging of these samples are presented in Fig 31. Panels on the left- and right- hand-side columns show images of Sample 1 and Sample 2, respectively. Top and bottom images were obtained using the broadband (BG39) and UV narrowband (BP380) filters, respectively. Suppression of autofluorescence from CCT solvent, visible as structured layout (Fig 31 (a)), is evident by comparing panels in Fig 31 (a) and (b). Likewise, the strong skin autofluorescence (Fig 31 (c)) is efficiently filtered by the UV narrowband filter (Fig 31 (d)). The excised skin sample was deprived of NAD[P]H resulting in reduced autofluorescence intensity, probably, dominated by FAD fluorescence (Palero, 2007). It is noted that although the broadband emission in the visible spectrum of ZnO-nano has been reported previously (Lin, 2005), it was not observed in this study due to ZnO-nano high crystal quality (Cheng, 2005), where it has been presented that the broadband emission of ZnO-nano was dependent on annealing the crystal defects.

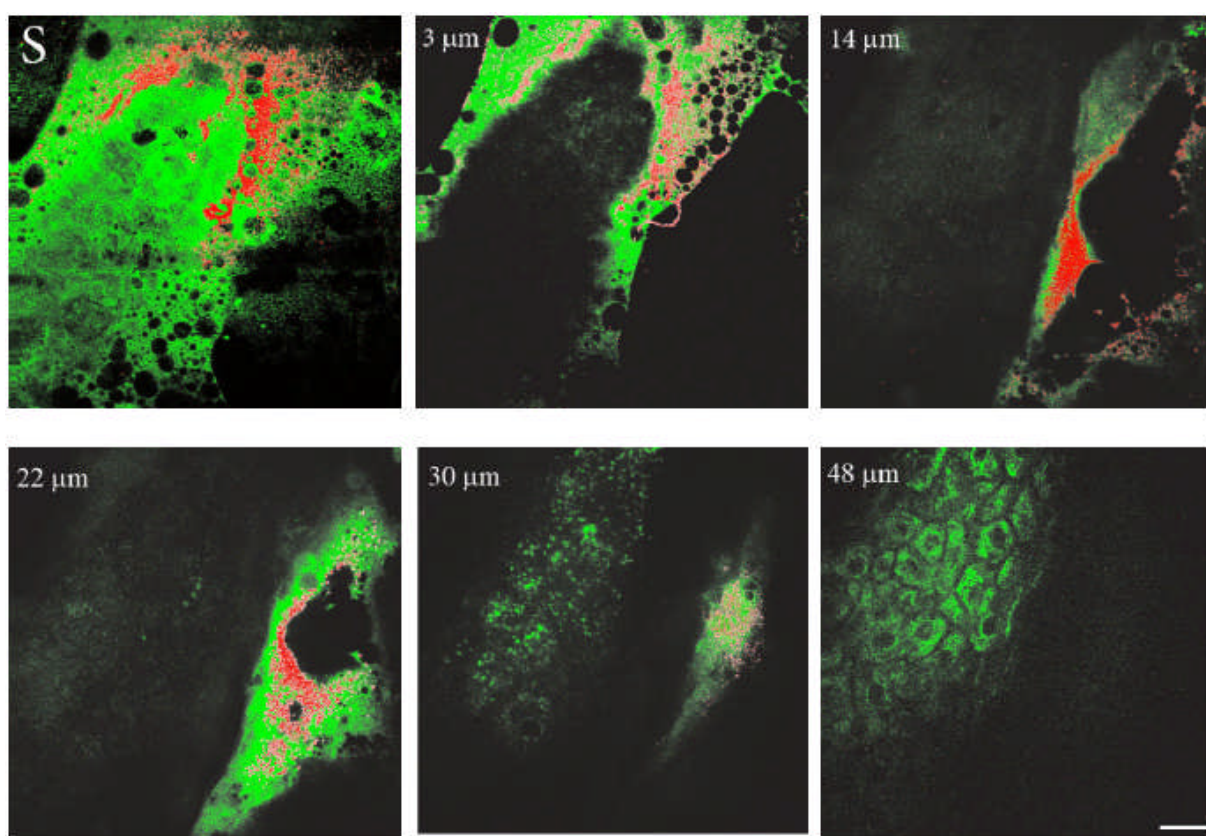


Fig 32. Overlaid FMM images of human skin *in vivo* (colour-coded green) and ZnO-nano distribution (colour-coded red) 4 hours after its topical application. *En face* optical sections of the skin are displayed from top left to bottom right at depths 0, 3, 14, 22, 30, and 48  $\mu\text{m}$  from the skin surface

designed S, 3  $\mu\text{m}$ , 14  $\mu\text{m}$ , 22  $\mu\text{m}$ , 30  $\mu\text{m}$ , and 48  $\mu\text{m}$ , respectively. Note ZnO localization in *stratum corneum* and in skin folds. No presence of nanoparticles in the *stratum granulosum* layer (ellipsoidal cells with dark nuclei) is observable. Scale bar 20  $\mu\text{m}$

First, *in vivo* imaging experiments of human skin treated with the zinc oxide commercial formulation were carried out, and the results are presented in Fig 32. Overlaid FMM images of human skin *in vivo* and ZnO-nano distribution, 4 hours after its topical application, are colour-coded green and red, respectively. *En face* optical sections of the skin are displayed from top left to bottom right at depths 0, 3, 14, 22, 30, and 48  $\mu\text{m}$  from the skin surface designated S, 3  $\mu\text{m}$ , 14  $\mu\text{m}$ , 22  $\mu\text{m}$ , 30  $\mu\text{m}$ , and 48  $\mu\text{m}$ , respectively. The depth read out was corrected for the confocal parameter, calculated as  $d_z = (z - z_0) \cdot n$ , where  $(z - z_0)$  denotes a difference between the axial position read out at a depth and top surface settings, and  $n$  denotes the mean refractive index of tissue, which was set to a mean value of 1.4 (Tuchin, 2000). ZnO-nano patterns are clearly observable on the skin auto fluorescence background, and especially pronounced on the topmost layers of the skin. Fine morphological details of unstained skin are clearly observable, *e.g.* cell structure in *stratum granulosum* (Fig 32, bottom left panel), with dark nuclei and granulated pattern in the cell cytoplasm, presumably, originated from NAD[P]H accumulated in mitochondria.

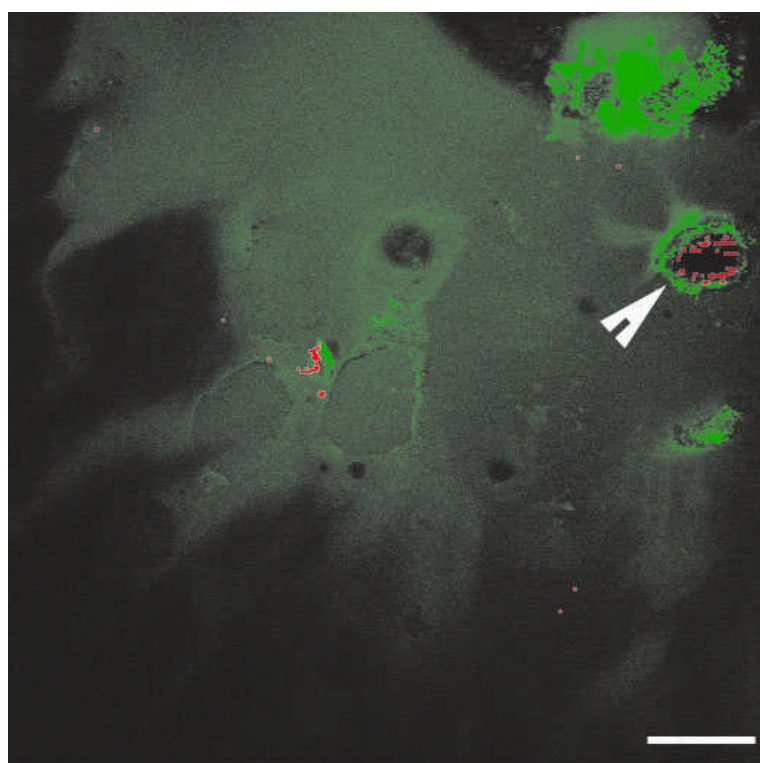


Fig 33. Overlaid FMM images of the freshly (2 hours) excised human skin *in vitro* (colour-coded green) and ZnO-nano distribution (colour-coded red) 4 hours after its topical application. An arrow points the

hair follicle canal, where a hair follicle shaft is not visible. ZnO formulation is localized around the hair follicle. Scale bar 20  $\mu\text{m}$

Fig 33 shows a FMM cross-sectional image of the freshly (2 hours) excised human skin topically treated with the sunscreen formulation. Using FMM, it is possible to investigate alternative pathways of nanoparticle penetration, which are represented by the hair follicle canal. Since the hair follicle shaft can extend at a considerable depth in skin, 50  $\mu\text{m}$  or greater, it can potentially represent an entry port of toxic material directly into the viable epidermis. A prominent ZnO signal is noticeable at the perimeter of the hair follicle (white arrow). The hair shaft is not visible in the image.

#### 2.5.6 TiO<sub>2</sub>-nano MPM imaging

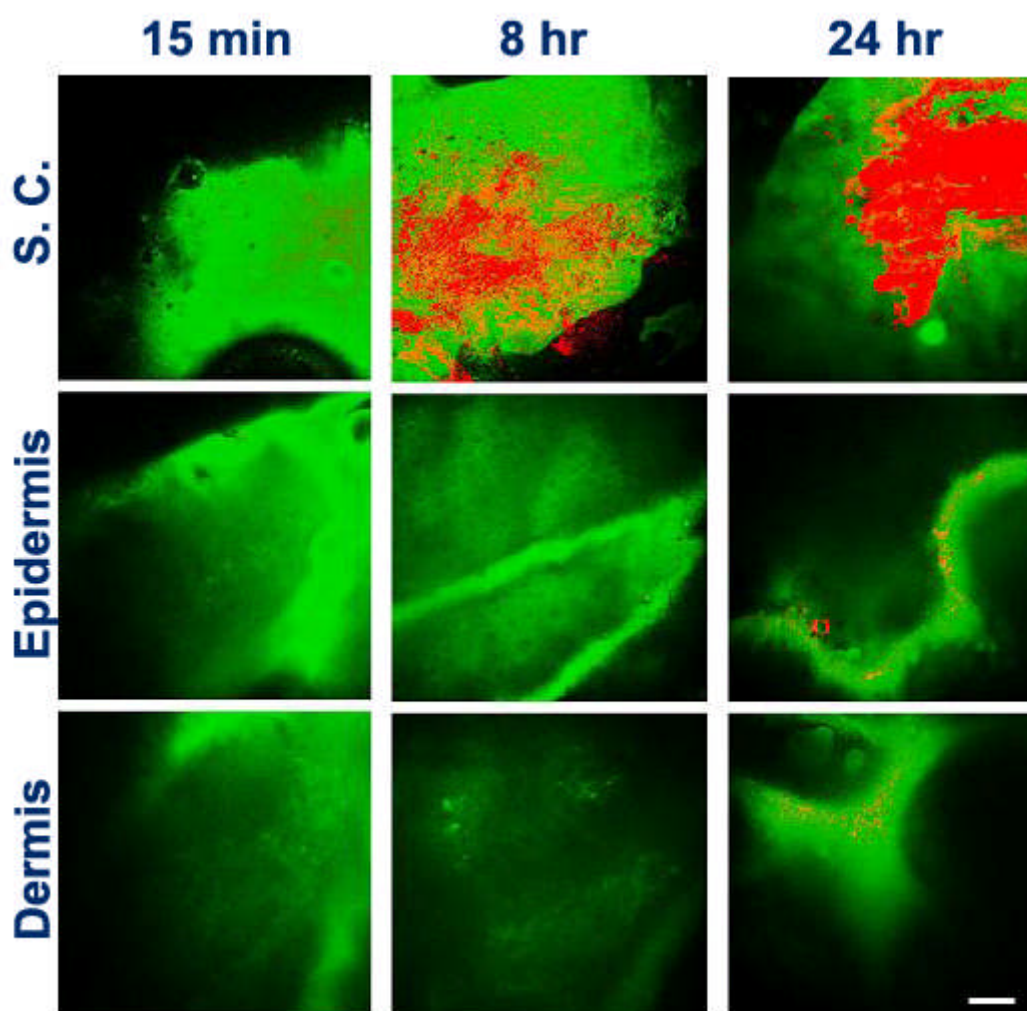


Fig 34. Overlaid MPM images of TiO<sub>2</sub>-nano pyrene (colour-coded red) distribution in excised human skin (colour-coded green). Rows: S.C., *stratum corneum*; Epidermis, viable epidermis, 30  $\mu\text{m}$  under the skin surface; Dermis, dermis, 80  $\mu\text{m}$  under the skin surface. Columns: 15 minutes, 8 hours, 24 hours, excised skin sample images acquired 15 minutes following TiO<sub>2</sub>-nano/pyrene formulation

topical application, following 8 hours, 24 hours incubation in a 35°C water bath. Traces of red indicate the formulation presence in skin folds, which is clearly localised. Scale bar 20  $\mu\text{m}$

Fig 34 shows the results of MPM imaging of  $\text{TiO}_2$ -nano in skin, where the excised skin sample was flexed following the topical application of the  $\text{TiO}_2$ -nano/pyrene paste. Skin flexing represents a physical enhancement approach whose efficiency has been demonstrated for NP transdermal penetration by Tinkle (Tinkle, 2003). In the case, however, both untreated and physically enhanced (flexed) skin samples showed negative results, i.e.  $\text{SiO}_2$ -capped  $\text{TiO}_2$ -nano/pyrene composite nanoparticles, size-ranged 15-20 nm, stayed on *stratum corneum*, or localised in skin folds, dermaglyphs, or in hair follicle roots, but not passed to the viable epidermis layer of skin.

## 2.6 Discussion

The size of ZnO-nano and Qdots were further determined by SEM and proved to be not change after changing concentration or pH or application on skin. The emission spectrum of ZnO-nano in Dr Lewinns' private formula (60% w/w) had the similar results as previous reported data, which was 377 nm (measured) to 385 nm (reported).

MPM setup has been proved to be an effective method for *in vivo* and *in vitro* ZnO-nano and  $\text{TiO}_2$ -nano/pyrene skin imaging. The ZnO-nano nonlinear optical contrast on the cell auto fluorescence background is remarkable and surprising (Zvyagin, 2008). There are several factors contributing to this contrast: 1. PL of ZnO-nano is considerably enhanced. 2. The principle PL band is spectrally situated in the “quite” spectral zone, i.e. spectral range of reduced skin autofluorescence.

Firstly, Guo have reported that the third-order nonlinear susceptibility,  $\chi_{\text{ZnO}}^{(3)}$  of ZnO-nano sized  $d = 4$  nm is almost 500-fold of that of bulk ZnO (Dong, 2005). It is accepted that this enhancement is due to quantum confinement effects. It refers to the earlier discussion in Sub-Section 2.2.1.3, with a notion that it is deep-level localised excitonic electronic structure of ZnO that is responsible for these effects, in contrast to the quantum confinement effects due to the nanocrystal size approaching the Bohr radius (1.8 nm). The systematic study of  $\chi_{\text{ZnO}}^{(3)}$  versus ZnO-nano size in the size range of 6 – 18 nm has revealed  $\chi_{\text{ZnO}}^{(3)}$  quadratic size dependence, with  $\chi_{\text{ZnO}}^{(3)}$  measured to be  $9.0 \times 10^{-10}$  esu (expressed in cgs system of units) at  $d = 18$  nm,  $\lambda = 532$  nm (Irimpan, 2008).

In order to evaluate attainable contrast of ZnO-nano on the autofluorescence background of skin, the two-photon excitation fluorescence signal from ZnO-nano with that of the endogenous fluorophores typical to skin were compared. Two-photon absorption cross-section of ZnO-nano,  $\sigma_{ZnO}^{(2ph)}$ , which is governed by a third-order nonlinear process (Sutherland, 1996), can be found by using the third-order nonlinear susceptibility,  $\chi_{ZnO}^{(3)}$  of ZnO reported in the literature:

$$\sigma_{ZnO}^{(2ph)} = \frac{2\eta\omega^2}{3Nn_0^2c^2\varepsilon_0} \text{Im} \chi_{ZnO}^{(3)} \quad (2)$$

Where  $\eta$  stands for the Plank's constant,  $\omega = 2\pi c / \lambda$  is the optical angular frequency;  $N$  denotes nanoparticle concentration recalculated from the molar concentration of  $10^{-4}$  M, reported in Ref (Dong, 2005);  $n_0$  is the refractive index of ZnO at  $\lambda = 532$  nm that amounts to 2.0;  $c$  – speed of light;  $\varepsilon_0 = 8.854 \times 10^{-12}$  F/m is the dielectric permeability constant.  $\chi_{ZnO}^{(3)}$  is converted from  $9.0 \times 10^{-9}$  esu in the cgs system of units to  $\chi_{ZnO}^{(3)} \cong 1.3 \times 10^{-17} \text{ m}^2 / \text{V}^2$  in the SI system of units. Substitution of these values to Equation 2) yields

$$\sigma_{ZnO}^{(2ph)} \cong 1.2 \times 10^{-49} \text{ m}^4 \text{ s} / \text{photon} \cdot \text{particle} \equiv 12 \text{ GM} \quad (3)$$

for an 18-nm ZnO-nano at  $\lambda = 532$  nm, where a convention of  $1 \text{ GM} \equiv 10^{-50} \text{ m}^4 \text{ s} / \text{photon} \cdot \text{molecule}$  for two-photon absorption cross-section was used. In order to evaluate a fluorescent signal from the sample, it is important to determine nanoparticle action cross-section  $\sigma_{ZnO}^{(TPEF)}$ , which is defined as a product of the absorption cross-section and quantum yield  $\Phi$ .  $\Phi$  represents a number of fluorescence photons emitted per one absorbed photon (per two photons in TPEF). According to the literature reports, the ZnO quantum yield varies depending on the crystal and surface quality, with a typical value of  $\phi = 0.02$  (Schubnell, 1997). The two-photon action cross-section is evaluated to be:  $\sigma_{ZnO}^{(TPEF)} = 0.26 \text{ GM}$  for an 18-nm particle typical for the experimental conditions. This value is much less compared to that of water-soluble Qdots,  $\sim 5 \times 10^4$  GM (Larson 2003), c.f. exogenous (externally introduced) fluorophores, such as fluorescein,  $\sim 50$  GM. At the same time,  $\sigma_{ZnO}^{(TPEF)}$  is favourably comparable to that of the dominant skin endogenous fluorophores, including reduced NAD[P]H, FAD, and retinol, whose  $\sigma_{fluor}^{(TPEF)}$  does not exceed 0.1 GM at 700 nm (Larson, 2003).

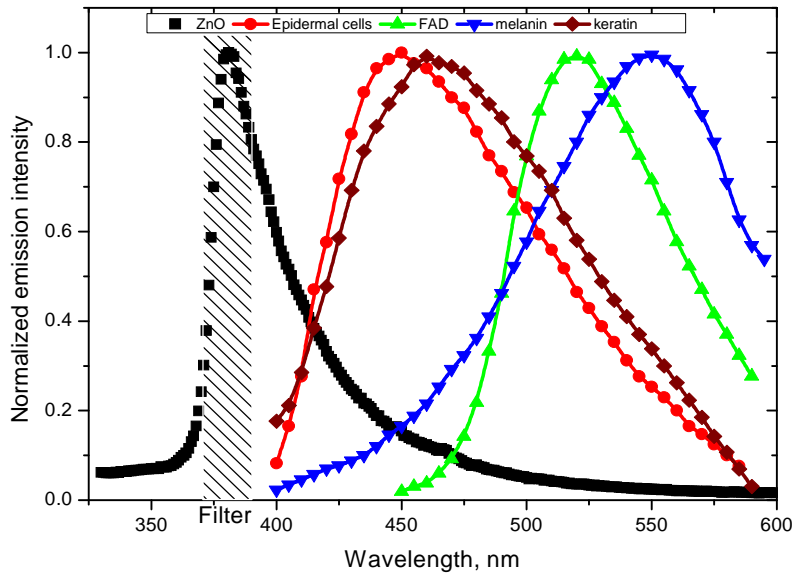
Secondly, in the context of FMM imaging, the visibility of ZnO-nano material on the skin autofluorescence background is determined by its TPEF cross-section relative to that of endogenous fluorophores, its relative concentration, and its fluorescence emission spectral overlap with the dominant skin fluorophores. Skin autofluorescence has been investigated, both *in vivo* and *in vitro* (Kollias, 1998). The skin autofluorescence spectrum has been reported in the literature to feature three major component bands revealed centred at 450 nm, 520 nm, and 625 nm upon excitation in the wavelength range of 340 nm – 380 nm. The first two spectral bands corresponded to 75% and 25% of the total spectrum intensity, respectively (Alvarez-Roman, 2004). These two peaks in the skin autofluorescence spectrum correspond to the fluorescence emission peaks of the endogenous skin fluorophores that include collagen, elastin, NAD[P]H, and FAD (Kollias, 1998), whereas the peak at 625 nm corresponds to porphyrins. Skin autofluorescence background excited as a result of the nonlinear optical processes, is somewhat different. It is spectrally separated into an intense second-harmonic generation signal from collagen, which occurs at a precisely half the laser excitation wavelength (UV range), a narrow emission band from 400 nm to 430 nm, and a broadband emission from 430 nm to 600 nm (see Fig 35) (Palero, 2007). In live skin, the autofluorescence spectrum in epidermis is dominated by NAD[P]H, as this co-enzyme is involved in cellular energy metabolism. Vitamin derivatives, such as flavins (FAD), also have a noticeable contribution to the autofluorescence spectrum of epidermis *in vivo*. In the excised epidermis, NAD[P]H contribution is markedly reduced due to degradation of the metabolic cycles, resulting to the reduced autofluorescence level and its spectral red shift due to keratin and to some extent flavin components.

It is important to note that the ZnO-nano UV absorption band is advantageous to enable spectral discrimination of its emission signal from the most endogenous fluorophores of skin, including NAD[P]H, riboflavin, folic acid, retinol, all having emission bands in visible. At the same time, the emission band of pyridoxine falls into that of ZnO-nano (Larson, 2003), and demands attention in certain imaging scenarios. However, for the nanoparticle transdermal penetration study, confined to the *stratum corneum* and viable epidermis, such collagen-related molecules as pyridoxine, pose little problem, since they are predominantly present in dermis. Neither the second harmonic generation signal from collagen (see Fig 35 (b)) presented a problem due to its predominant location in dermis.

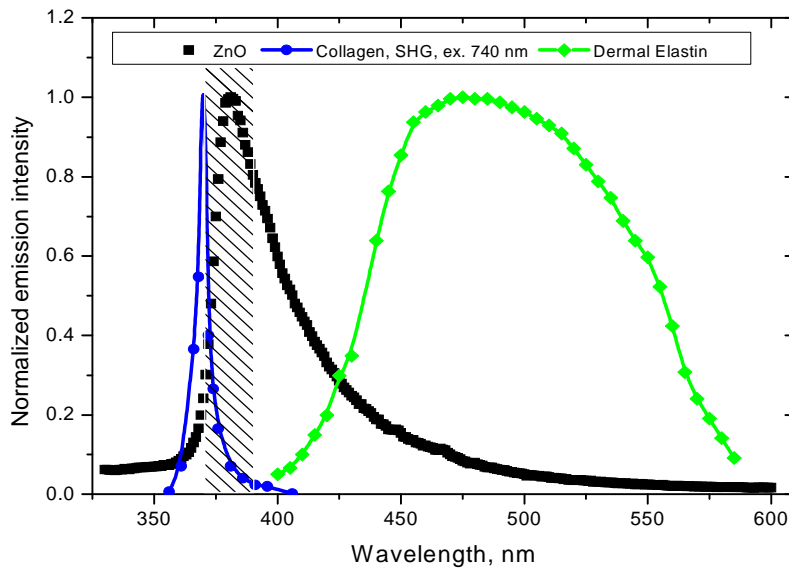
The femtosecond laser excitation wavelength of 740 nm used in the experiments is suboptimal for the excitation of ZnO-nano TPEF, as the ZnO-nano bandgap width of 3.4 eV



( $\lambda = 350$  nm) requires two-photon excitation at a fundamental wavelength of 700 nm. At the same time,  $\sigma_{\text{ZnO}}^{(2ph)}$  dependence versus  $\lambda$  falls off gradually from 350 to 380 nm, where  $\sigma_{\text{ZnO}}^{(2ph)}(\lambda = 740\text{nm}) \cong 0.4\sigma_{\text{ZnO}}^{(2ph)}(\lambda = 700\text{nm})$  (Irimpan, 2008). At the same time, Irimpan has noted a steep increase of  $\text{Im}\chi_{\text{ZnO}}^{(3)}$  versus the laser intensity (Irimpan, 2008). Therefore, the evaluation of  $\sigma_{\text{ZnO}}^{(2ph)}$  (see Equation 3)) needs to be treated only as a rough estimation. It is worth mentioning, unlike in case of free excitons, characterized by  $\sigma^{(2ph)} \propto d^3, \sigma_{\text{ZnO}}^{(2ph)} \propto d^2$ , in the size range  $d = 6 - 18$  nm, revealing the bound exciton nature of ZnO-nano.  $\sigma_{\text{ZnO}}^{(2ph)}$  is also sensitive to the crystal/surface quality. The preliminary data on the nonlinear optical signal intensity versus input power suggests that three-photon nonlinear optical absorption makes a slight addition contribution to the excitation of ZnO-nano (Dai, 2005). Although  $\text{Im}\chi_{\text{ZnO}}^{(3)}$  has been recently measured, no data on the three-photon absorption cross-section of ZnO-nano has been reported to the best of the knowledge.



(a)



(b)

Fig 35. Emission spectrum of ZnO-nano at an excitation wavelength of 320 nm (scatter plot, squares) superimposed on TPEF spectra of:

- (a) Epidermal cells (circles), similar to a spectrum of NAD[P]H; FAD (triangles); melanin (inverted triangles); keratin (diamonds), adopted from Ref (Palero, 2007).
- (b) Elastin (diamonds), similar to collagen, adopted from Ref (Palero, 2007); and SHG spectrum of collagen calculated at a 740-nm fundamental wavelength.

A dashed area designates FWHM of the bandpass filter BP380 used to discriminate ZnO-nano PL signal against the skin autofluorescence

## 2.7 Conclusion

In this Chapter, the physical and optical properties of semiconductor nanoparticles: ZnO-nano, TiO<sub>2</sub>-nano, and Qdots were reviewed and reported, that were envisaged to be useful for study of nanoparticles transdermal penetration *in vivo* and *in vitro*. The high two-photon cross-section value of ZnO-nano in combination with its UV emission band in the “quiet” spectral range of the skin autofluorescence make it a very attractive nanoprobe candidate for the direct imaging using MPM. Skin penetrability to nanoparticles *in vivo* and *in vitro*, can be studied using the nanoparticles presented in this Chapter. Detailed study of the nanoparticle penetration in skin is presented in Chapter 3.



## Chapter 3 Nanoparticle penetration into *stratum corneum* and hair follicles

### 3.1 Introduction

Many modern cosmetic or sunscreen products contain nano-sized components. Transdermal delivery and cosmetic research suggests that vesicle materials may penetrate the *stratum corneum* of intact human skin, but not living skin. Depending on the physical/chemical properties of the ingredient and the formulation, nano-sized formulations may enhance or reduce skin penetration, albeit at a limited rate (Nohynek, 2007). ZnO-nano and TiO<sub>2</sub>-nano are efficient UV light absorbers, and as such, are two main components in the commercial sunscreen products. Whether these nanoparticles are small enough that are rendered penetrable through *stratum corneum* is still hotly debated. Nevertheless, if they penetrate into the viable epidermis or in dermis, cytotoxicity can occur due to free radical generations (likely, hydroxyl radicals through oxidation). Also, it can cause adverse effects in isolated cell experiments (Dunford, 1997; Jeng, 2006). Therefore, these nanoparticles transdermal penetrability deserves particular attention. As an illustration, the studies of Alvarez-Roman showed no penetration through excised human skin (Alvarez-Roman, 2004). In contrast, Ryman-Rasmussen (Ryman-Rasmussen, 2006) show extensive penetration of neutral, positively charged and negative, charged Qdots through porcine skin.

Conventional SEM, TEM and Franz cell penetration involve indirect or/and destructive sampling of skin that limits the experimental methods to *in vitro* observations. Optical microscopy of nanoparticle distribution in skin *in vivo* is precluded due to high scattering efficiency of the superficial layers of skin, especially human skin. FCSM and FMM have enabled production of clear sub-surface images of skin at depths down to ~100 µm at the micrometer resolution by way of “optical sectioning” thin layers of the specimen. The skin morphology contrast is derived from the skin autofluorescence, although often requires additional staining. Visibility of nanoparticles depends on their fluorescent properties that limits their choice to the following materials: micro- and nano-beads impregnated with fluorescence dye molecules; photoluminescent nanomaterials; Qdots structures (Larson, 2003); and emerging nanocrystals with colour centres (Chang, 2006; Lee, 2008). Fabrication of nano-beads impregnated with fluorescent dye is difficult and they are prone to photobleaching. Qdots are cytotoxic, thus, posing hazard for *in vivo* applications on humans. Thus, they only can be used in *in vitro* studies. ZnO-nano represents a promising nanomaterial that is widespread, inexpensive, and has proven to be suitable for cosmetic care and pharmacy. Its

production is straightforward, yielding nanoparticle of various sizes and shapes, starting from 3 nm and larger (Cheng, 2006; Lin, 2005).

In this study, three types of nanoparticles to investigate the skin permeability will be employed: metal oxide nanoparticles, including ZnO-nano (the main focus), TiO<sub>2</sub>-nano, which are allowed to use in medical research – they are regarded safe and accepted in cosmetic care and pharmacy; and Qdots. The investigation of Qdots with three functional surface coatings to assess different skin penetration scenarios will be reported. Study of these Qdots can reveal the influence of surface coating on particle penetration. Furthermore, it will provide important information on drug formulation for transdermal delivery. *In vitro* study was carried out on human skin and porcine skin using three types of particles. *In vivo* study was carried out on human skin using only ZnO-nano. TiO<sub>2</sub>-nano was pyrene coated and would not have been approved for *in vivo* human testing as it was prepared in house in the lab. There is no safety formulation of the Qdots used in this study, which can be applied on living human skin. Physical enhancement and chemical enhancement were both used to enhance the penetration of nanoparticles through *stratum corneum*. FMM was employed as a principle imaging tool for *in vivo* and *in vitro* study. FCSM was also used in *in vitro* study. SEM was used for ultrahigh-resolution imaging of nanoparticles. The experiments using FLIM will be reported.

## **3.2 Sample preparation: procedures and methods**

### **3.2.1 Skin sample preparation for *in vivo* study**

0.3 g of the sunscreen product (Dr Lewinns' special formula, Advanced Nanotechnology, Western Australia) was applied evenly to the selected area of forearms, which was the only experimental site on living skin of four subjects. The sunscreen was rubbed in for 5 minutes. The treated area was imaged using the DermaInspect imaging system.

In order to study dynamics of nanoparticle penetration in skin, images were taken during three imaging sessions: immediately, 4 hours, and 24 hours after the sunscreen topical application. The 24-hour imaging session was followed by the skin washing using a soft soap, when taking a shower, as a part of the normal daily routine. The participating person was allowed to move the arm as per usual, followed the first imaging, session. The participating subjects were, as follows: an Asian female of Chinese nationality, aged below 30; two Caucasian males, aged 30 - 40, an Indian male, aged 40 - 50. All experiment conducted on human subjects were carried out with the approval of Princess Alexandra Hospital Research Committee (Approval

no. 097/090, administrated by the University of Queensland Human Ethics Committee), with the subject written consents.

### **3.2.2 Skin sample preparation for *in vitro* study**

#### ***ZnO-nano and TiO<sub>2</sub>-nano***

10  $\mu$ L 60% w/w zinc oxide dispersed in CCT, or 0.02-g TiO<sub>2</sub>-nano/pyrene paste as described in Sub-Section 2.4.6, was applied on the excised skin patch.

Human and porcine skin samples were investigated. As for the human skin sample, the skin patch was excised from the human abdomen, as a result of the liposuction surgery procedure (female, 33 years old, excised 12<sup>th</sup> June 2007). As for the porcine skin sample, 20-mm radius, 5-8 mm-thin patches of skin were cut from the dorsal part of the animal for preparing samples (female 25-30 kg, 16 to 20 weeks, excised 8<sup>th</sup> October, 2007). The skin patches were placed in Franz cells whose edges were covered with silicone vacuum grease, and the receptor compartment was filled with pH7.4 PBS buffer, in order to keep the skin moisturised. They were kept at 35°C in a water bath for 8 or 24 hours.

#### ***Qdots***

A 40- $\mu$ L drop of Qdots (Qdots, Invitrogen) at 1- $\mu$ M concentration, (2 to 9- fold dilutions in of the supplied Qdots solutions) was applied to a 1.33-cm<sup>2</sup> skin area, following the protocol described by Ryman-Rasmussen (Ryman-Rasmussen, 2006). The authors reported the following sample preparation: A 40- $\mu$ L drop of Qdots at 1- $\mu$ M concentration was applied to 0.64-cm<sup>2</sup> of skin and remained during the course of a working day or overnight. A molar concentration per unit area of 30-pM per cm<sup>2</sup> remained on the skin for 8 or 24 hours. Three surface coating of Qdots were investigated: amine, PEG and carboxylic. The reported protocol was followed for each Qdots coating. Two 1- $\mu$ M suspensions kept in solution of two pH-values were prepared: pH7 (communicated by the provider); original pH of the Qdots (pH8.3 for amine- and PEG- surface derivatisation, and pH9 for carboxylic surface derivatisation). Amine and PEG Qdots original suspensions were diluted in pH8.3 buffer, which was mixed by 10-mL of 50 mM sodium borate (molecule weight 381.37, AF608115, Ajax Finechem); and 14-mL of 150 mM boric acid (molecule weight 61.83, AF601053, Ajax Finechem), to obtain 1- $\mu$ M Qdots pH8.3 amine and PEG solutions. Amine pH7 1- $\mu$ M suspension was diluted in 150 mM boric acid only. PEG pH7 1- $\mu$ M suspension was diluted in pH8.3 buffer and 1- $\mu$ M HCl. Carboxylic pH9 1- $\mu$ M suspension was diluted in 50-mM sodium borate, and pH7 1- $\mu$ M solution was diluted in 50-mM sodium borate and 1- $\mu$ M HCl.

The patches of skin were sandwiched by glass horizontal static Franz diffusion cells whose edges were covered with silicone vacuum grease, and the receptor compartment was filled with pH7.4 PBS in order to keep the skin moisturized. On the day of the experiment, the skin was cut into circular pieces by using a 20-mm diameter metal punch, in order to fit them into the Franz cells, leaving 1.33-cm<sup>2</sup> exposed areas, where the Qdots solution was applied. The top and beak of the Franz cells were blocked with a parafilm to avoid evaporation of the Qdots solvent. The cells were put in a water bath at temperature of 35 °C to mimic the human skin temperature, for 8 or 24 hours. In order to test the barrier function of the *stratum corneum*, tape-stripped skin samples with the *stratum corneum* layer removed were prepared. The intact skin was stripped 20 to 30 times by a medical tape prior to application of the Qdots suspensions.

### **3.2.3 Skin sample preparation for physically enhanced nanoparticle penetration in skin *in vivo* experiments**

In order to investigate effects of physical enhancement (skin flexing and stretching) on the skin permeability to nanoparticles, dorsal and ventral side of the human volunteer wrist skin (South-American male, aged 40 to 50) was treated with the ZnO-nano sunscreen (Dr Lewinns' private formula). Sunscreen of 0.01-g was applied on 4-cm<sup>2</sup> square area, which is 2.5-mg/cm<sup>2</sup>. The subject moved his wrist with flexibility typical for his daily life activity, for 60 minutes, followed by 5 seconds massage of the cream to the skin by a massage machine. An average number of stretching and flexing was evaluated to be 15 times per minute.

### **3.2.4 Skin sample preparation for physically enhanced nanoparticle penetration in skin *in vitro* experiments**

10 µL 60 % (w/w) ZnO-nano dispersed in CCT or 0.02 g TiO<sub>2</sub>-nano/pyrene paste was applied on the excised skin patch. Both human and porcine skin samples were investigated. Human and porcine skin samples were prepared in the same way as described in Sub-Section 3.2. The skin treated topically with ZnO-nano or TiO<sub>2</sub>-nano formulations was mounted on the stretching machine (see Fig 36) to exercise before inserted in Franz cells. The skin was flexed for 60 minutes at a frequency of 1 Hz at 60 degree. The treated skins samples were inserted into Franz cells whose edges were covered with silicone vacuum grease, and the receptor compartment was filled with pH7.4 PBS buffer in order to keep the skin moisturized. They were kept at 35 °C water bath for 8 hours or 24 hours.

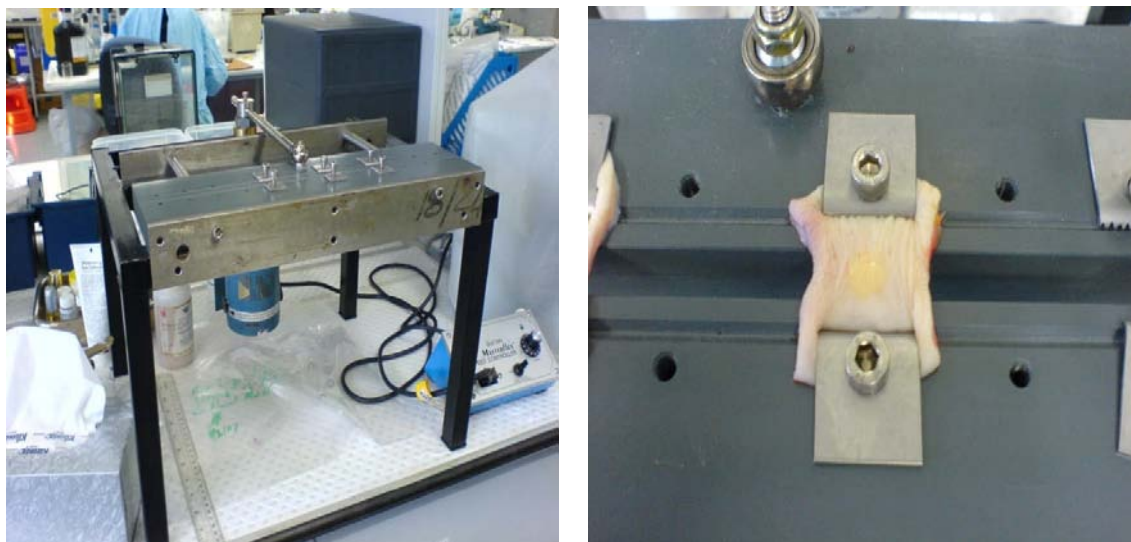


Fig 36. Top panel, a photograph of the stretching and flexing device designed and built in-house; bottom panel, the skin patch is mounted on the stretching and flexing device. A coloured spot on top of the treated skin (Qdot suspension) is observable

### 3.2.5 Skin sample preparation for chemically enhanced nanoparticle penetration in skin *in vitro* experiments

#### *Chemicals*

Four chemical enhancers were used to check the penetration enhancements. They belong either to the terpene group (Menthol, Limonene, 1,8-cineol eucalyptol) or the group of commercial sunscreen ingredients (salicylic, carboxylic). It was aimed to test a hypothesis that the terpene-group chemicals change the lipid bilayers structure and hence enhance the skin penetrability. The positive result of this test might indicate that the sunscreen ingredient enhances skin penetrability. These four chemicals were: Menthol, 5-ethyl-2-1-methylethyl cyclohexanol (M-2258, Lot 55H1032, Sigma), 50-mg dissolved in 1000 mg 20% ethanol: 80% distilled water; 1,8-cineol eucalyptol ( $C_{10}H_{18}O$ , 154.75 Da, 100 ml, boiling point 175-179 °C, density 0.924 g/cm<sup>3</sup>, Fluka), diluted down from 100% to 5% in ethanol; Limonene (136.24 Da, 100 ml, boiling point 175.5-176 °C, density 0.840 g/cm<sup>3</sup>, Aldrich), diluted to 5% in ethanol; Salicylic carboxylic, 2-ethylhexyl ester ( $C_{15}H_{22}O_3$ , 250.33 Da, 25-ml), diluted down to 5% in ethanol.

300-μL of the investigated chemical enhancer was applied to eight samples prior to application of Qdots and ZnO-nano. Four of them were in 35<sup>0</sup> C water bath for 8 hours and the other four were in water bath for 24 hours.

## ***Skin***

Female, aged 43, abdomen, excised 19<sup>th</sup> October 2007, and used for the menthol-enhancement and negative control experiments.

Female, aged 45, abdomen, excised on 21<sup>th</sup> November 2007, and used for 1, 8-cineol enhancement experiments.

Female, aged 43, abdomen, excised on 21<sup>th</sup> November 2007, and used for limonene and salicylic carboxylic enhancement experiments

Eight hours after the samples were in water bath, four of them were taken out of the Franz cell, wrapped with a wet gauge and put in a refrigerator overnight at temperature 4 °C. Next day, they were sent together with the other four samples which were in water bath for 24 hours, for the special treatment. The whole process was described in the following.

### ***Sample preparation procedure***

- 1) A 1.33-cm<sup>2</sup> patch of skin was cut from the excised skin sample.
- 2) 300 µL chemical enhancer solution was applied on the surface of the skin and kept in air for 1 hour
- 3) 40 µL Qdot solution was applied on top of the skin.
- 4) The skin was inserted in a Franz cell with pH7.4 buffer at the bottom. The upper part of the cell was sealed with a parafilm.
- 5) After an 8-hour or 24-hour treatment in a 35 °C water bath, the skin was removed and cut into small squares sized 0.5 cm<sup>2</sup>.
- 6) The skin sample was placed in 2% paraformaldehyde/0.1M phosphate buffer, pH7.4 w/5% sucrose at room temperature to fix for 60 minutes.
- 7) The fixed skin was rinsed three times (10 minutes per rinse) by 0.1M phosphate buffer w/5% sucrose at room temperature (step 8 to step 10, the container was put on a 100 times per minute rotator after changing solutions).
- 8) The skin was rinsed in 2:1 of 5% sucrose: 20% sucrose in 0.1M phosphate buffer at room temperature for 30 minutes.
- 9) The skin was rinsed in 1:1 of 5% sucrose: 20% sucrose in 0.1M phosphate buffer at room temperature for 30 minutes.
- 10) The skin was rinsed in 1:2 of 5% sucrose: 20% sucrose in 0.1M phosphate buffer at room temperature for 30 minutes.

- 11) The skin sample was kept in 20% sucrose in 0.1M phosphate buffer solution on the rotator in a cold room overnight.
- 12) Next day, the skin was freeze-dried in OCT with dry ice and 99% 2-methylbutane (Lab-scan).
- 13) The skin was cut into 8- $\mu$ m-thick cross section slices at -18 °C by Microm HM550, and put them on microscope glass slides.
- 14) Mounting media (Dakocytomation Fluorescent Mounting Medium) was applied on top of the skin slice and it was sandwiched between the glass slide and cover slip.
- 15) The sample was left at room temperature for several minutes.
- 16) The sample was finally ready for imaging using FCSM

### **3.2.6 Skin sample preparation for SEM experiments**

In order to obtain high-resolution images of skin and to validate the results of FMM imaging experiments, SEM imaging was carried out. The sample preparation represented a cumbersome and time-consuming part of this research. It was carried out using two protocols: traditional procedure based on the biomicrowave method, and the freeze-dry procedure. According to the observations, the freeze-dry technique appeared superior to that of the biomicrowave method, judging from the more detailed skin morphology information. Also, the nanoparticle loss was markedly reduced compared to that of the biomicrowave method. These methods are detailed separately in the following paragraphs.

#### ***Biomicrowave***

The Qdot-treated skin sample was prepared, as follows. Three pieces of intact skin obtained from the female abdomen (full thickness skin) were kept in a water bath after the application of 1- $\mu$ M Qdots suspensions for 8 or 24 hours in Franz cells. They were placed into the glutaraldehyde solution (5-mL glutaraldehyde, with 20-mL 0.1-M sodium cacodylate). After several hours, they were washed three times by 0.1-M sodium cacodylate, and each time placed into 80-W biomicrowave oven (AIBN, UQ) for 40 seconds. Subsequently, the samples were washed with 50% to 100% ethanol aqueous solutions. The concentration of the ethanol was increased by 10% each time to wash the sample and every time the sample was treated in 250-W biomicrowave for 1 minute after the wash. Finally, the processed skin samples were placed into a container with hexamethyldisilazane for 1 minute in the 250-W biomicrowave oven and kept outside overnight until complete vaporisation of the liquid hexamethyldisilazane. The tape-stripped samples were prepared by tape-stripping the skin samples 10 - 20 times followed by their fixation in glutaraldehyde solution.

The resultant samples were coated with 20-nm platinum film and imaged by JSM 6300F (Jeol, United Kingdom).

However, after several attempts, several disadvantages of this protocol have been found.

1. The sample was coated with 20-nm platinum and thus did not have high conductivity. Therefore, there was a lot of charging during imaging and resulted in blur images.
2. The sample was prepared in a way that easily to induce aggregation and thus it was hard to detect single Qdots on the skin surface.
3. The sample was processed several times by different chemicals and this may damage the cell structure and skin morphology. Also, more artefacts can be brought in.

### ***Freeze-dry***

After 8 hours or 24 hours being in the water bath, the skin was taken out and put in 2.5% glutaraldehyde for several days. The fixed skin was cut into 1-cm<sup>3</sup> cubical blocks, followed by snapped-freezing with a purpose-built copper press that had been dipped in liquid nitrogen for 5 minutes. The samples were further dipped whilst in the press in liquid nitrogen and then freeze dried. The small freeze-dried skin samples were mounted on the SEM, and imaged.

Prior to imaging, all the samples were vacuum-coated with 20 – 50-nm carbon film. Conductive paint was applied to the aluminium stub holder. In this way, nanoparticles or Qdots of greater electron density than that of carbon were visible as bright spots on the black skin background in the back-scattering imaging configuration.

### **3.2.7 Skin sample preparation for FLIM experiments**

One 1×1-cm<sup>2</sup> skin patch from the female abdomen epidermis was cut from the excised patch and placed on a glass slide. 10-μL 60% ZnO-nano in CCT solution was applied topically on the intact skin or independently on the slide. The sample was covered by a microscope cover slip of 170-μm thickness and sealed by nail polish. FLIM experiment was carried out immediately after sealing.

## **3.3 Results**

### **3.3.1 FMM imaging of the porcine skin *in vitro***

#### ***ZnO-nano***

FMM imaging of porcine skin *in vitro* was carried out, and the results are shown in Fig 37.



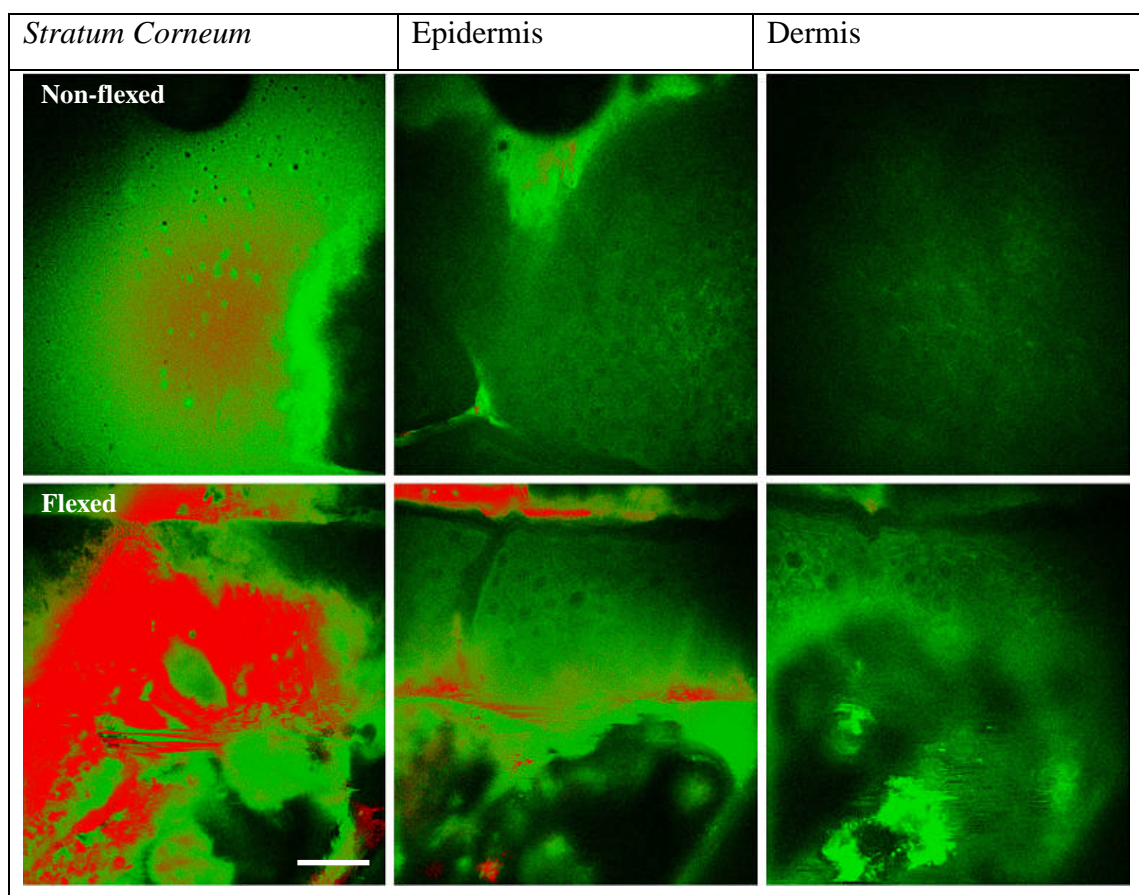


Fig 37. FMM images of ZnO-nano (colour-coded red) distribution in the porcine skin (colour-coded green). Top and bottom rows: porcine skin without and with flexing, respectively. Note the difference in ZnO-nano distribution in the skin epidermis upon physical enhancement of the skin penetrability via flexing. Scale bar 30  $\mu$ m

The axial depth of each image was measured as the average depth from the surface. Even though the depths were shown the same in the imaging software, actually the values were not exactly the same for taken at different skin sites due to skin morphology. From the two images of the first row, one can see that for the porcine skin, ZnO-nano, colour-coded red, stayed on the skin topmost surface, i.e. *stratum corneum*, which is colour-coded green. The images of epidermis show clearly structure of cells, visible as green circular network, with black holes in each circle (cell) that represents the cell nucleus. The cells are visible due to the two-photon excited autofluorescence. The cell nuclei predominantly contain DNA, and hence exhibit much reduced autofluorescence that renders them dark appearance in the images. For the sample without flexing, there was almost no ZnO-nano appearing on the image below *stratum corneum*, while for the flexed skin sample, there was more ZnO-nano staying on *stratum corneum*, even at the depth where epidermis cells appeared (see the image of flexed skin sample in “Epidermis” column). The column “Dermis” presents images of the skin sample “optically sectioned” at a depth of the dermis layer. No trace of ZnO-nano is observable at this depth.

### *TiO<sub>2</sub>-nano/ pyrene*

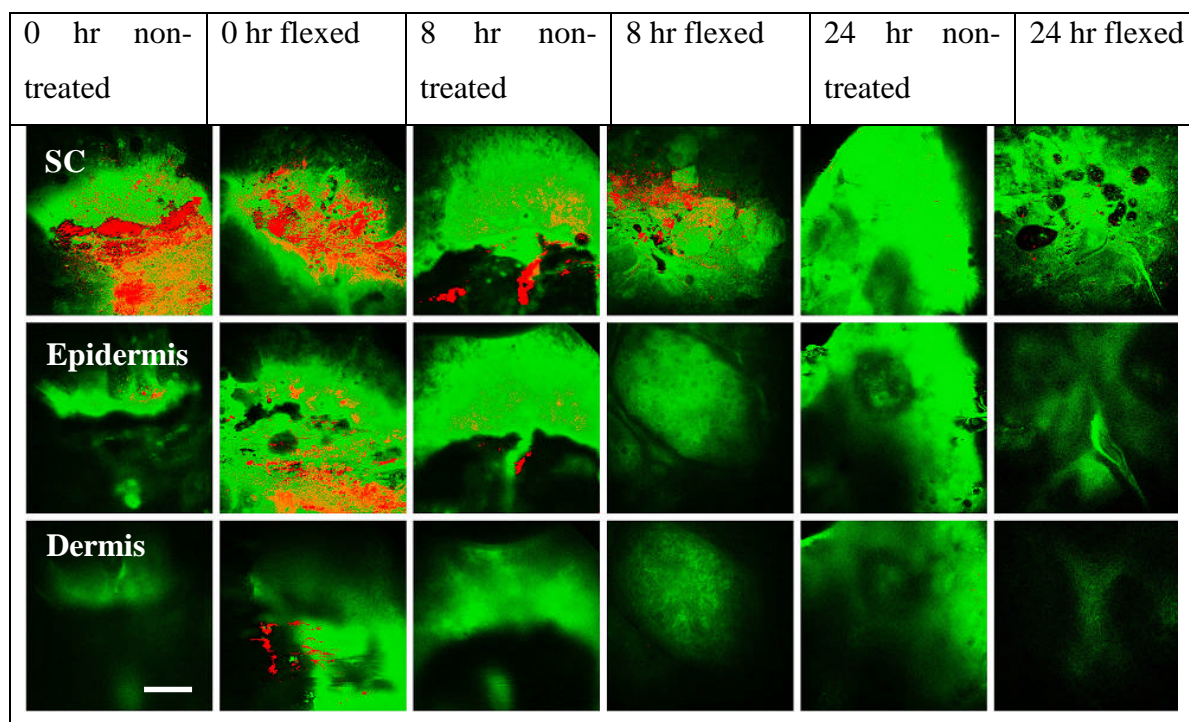


Fig 38. FMM images of TiO<sub>2</sub>-nano pyrene (colour-coded red) distribution in the porcine skin (colour-coded green). Rows: top row, *stratum corneum*; middle row, epidermis, 30  $\mu$ m under the skin surface; bottom row, dermis, 80  $\mu$ m under the skin surface. Columns: 0 hr non-treated, pristine sample imaged immediately after preparation; 0 hr flexed: flexed sample imaged immediately; 8 (24) hr non-treated, pristine sample after an 8 (24) hours 35<sup>0</sup>C water bath; 8 (24) hr flexed, flexed sample after an 8 (24) hours 35<sup>0</sup>C water bath. Scale bar 30  $\mu$ m

TiO<sub>2</sub>-nano distribution image is red-colour-coded. It is evidently stayed on the porcine skin top surface (see “0 hr non-treated”, “8 hr non-treated”, and “8 hr flexed”, Fig 38). Especially, for pristine skin, cells are clearly observable showing no TiO<sub>2</sub>-nano traces in the intra- and extra-cellular space in “8 hr flexed sample”. Images “0 hr flexed”, “24 hr non-treated”, and “24 hr flexed” are not particularly informative, although they show no TiO<sub>2</sub>-nano/pyrene signals.

### *Qdots*

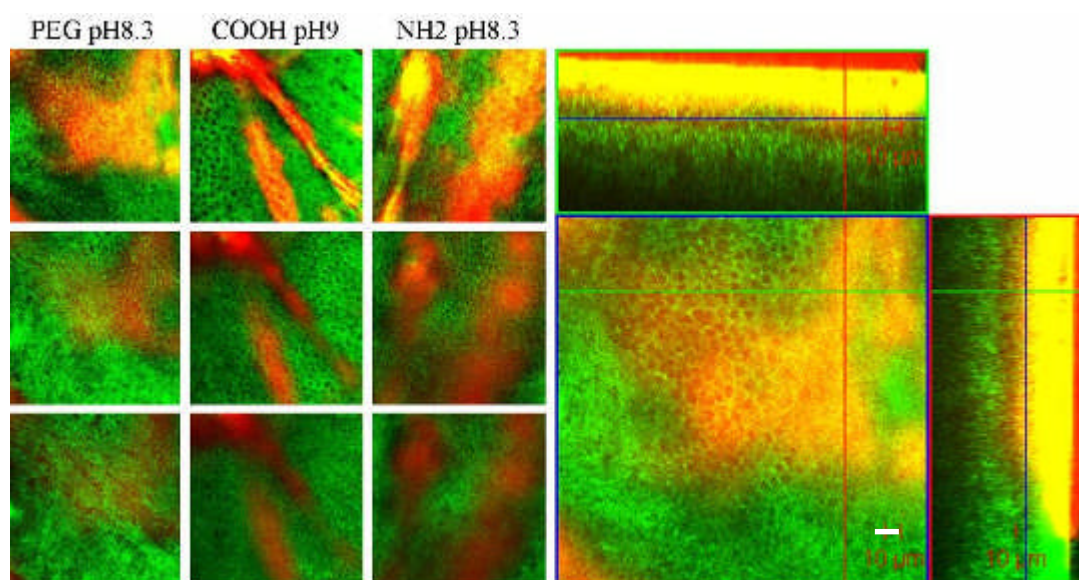


Fig 39. FCSM images of Qdots in the intact porcine skin. Qdots are colour-coded red, skin autofluorescence –green, the overlaid area is yellow-coloured. Cross-section images were realised with the Zeiss AIM software. Left panel of 9 images: Stack images: from top to bottom rows: 0  $\mu\text{m}$ , 40  $\mu\text{m}$ , 80  $\mu\text{m}$ , from the top skin surface, respectively. Columns (from left to right): z-stack image of PEG, carboxylic and amine Qdots. Right panel: zoom-in image of PEG Qdot distribution in skin. Cross-section images are extracted from the stack images acquired at each depth increment of 2  $\mu\text{m}$ . Scale bar 10  $\mu\text{m}$

The results of imaging of Qdots penetration into the porcine skin are presented in Fig 39. As the imaging depth is increased, from top to bottom (left columns), Qdots (red-coded) appeared on skin background (green-coded). The colour intensity is decreased gradually versus depth reflecting the Qdots concentration gradual decrease versus depth. However, Qdots presence in cells and extracellular space is clearly visible in both epidermis and dermis (see column PEG pH8.3 middle and bottom images). Also, from the cross-section image on the right side, it can be further confirmed that Qdots appeared in different skin layers which was presented as an overlaid yellow area of the red-coded Qdots signal and green-coded skin autofluorescence. This was in agreement with the results reported in the literature (Ryman-Rasmussen, 2006).

### 3.3.2 FMM imaging of pristine human skin, *in vivo* ZnO-nano, *in vitro* ZnO-nano, TiO<sub>2</sub>-nano and Qdots

#### *In vivo* study of ZnO-nano penetration in human skin

The results of FMM imaging of ZnO-nano penetration in skin are presented in Fig 40. Rows present FMM skin images of different ethnic origins. Columns are grouped in two subsets: 3 left- and right- hand-side columns present ZnO-nano distribution in *stratum corneum* and epidermis layers of skin, respectively. “0”, “4 hr”, “24 hr” designate time lapse imaging



sessions following topical application of ZnO-nano (procedure is detailed in Sub-Section 3.2.1).

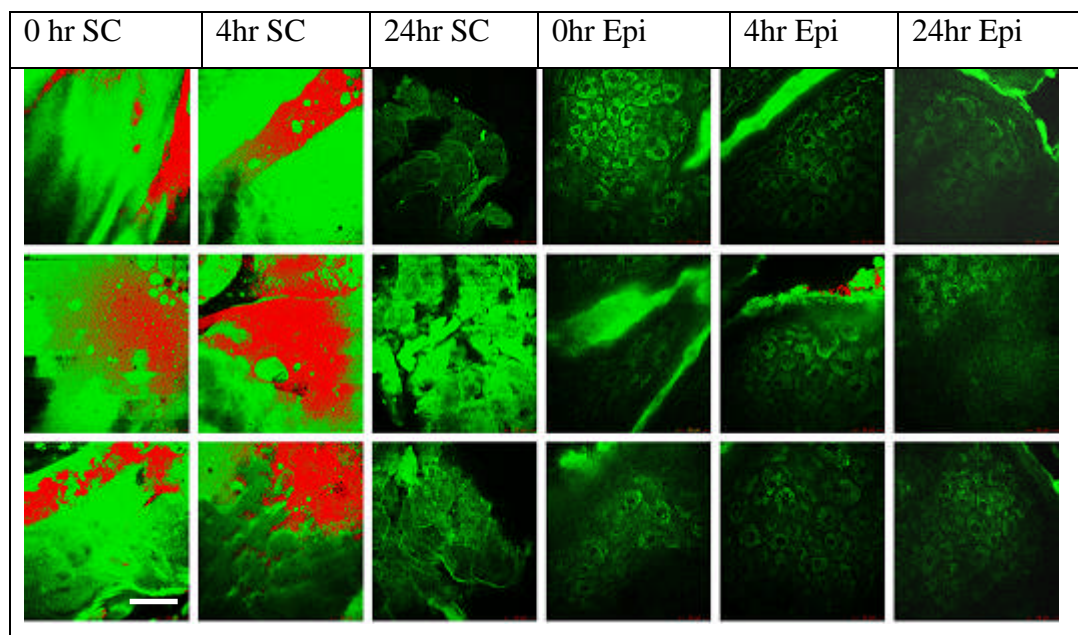


Fig 40. FMM images of ZnO-nano (colour-coded red) distribution in the human forearm skin (colour-coded green) *in vivo*: SC (*Stratum corneum*); Epi (Epidermis). 1st row (Asian female, Chinese, aged below 30); 2nd row (Caucasian male, aged 30 -40); 3rd row (Indian male, aged 40 - 50). 0hr SC: image of *stratum corneum* immediately after the sunscreen application on the forearm; 0hr Epi: image of the epidermis immediately after the sunscreen application on the forearm; 4hr SC: image of *stratum corneum*, 4 hours after the sunscreen application on the forearm. Scale bar 40  $\mu$ m

As Fig 40 shows, ZnO-nano, colour-coded red, evidentially stayed on the human skin surface (*stratum corneum*), which exhibited bright autofluorescence, colour-coded green, especially obvious in “0 hr SC”, “4 hr SC” image columns. The “24 hr SC” column images acquired after the subjects took a shower indicates that ZnO-nano was completely removed from the skin surface, without traces. In “24 hr SC” characteristic hexagonal squamous corneocytes are clearly observable. Note bright fluorescence origin is attributed to keratin abundance in *stratum corneum*. The right-hand-side images show the viable epidermis cellular structure, where characteristic *stratum germinasium* cells are very distinct, with dark nuclei, and bright cytoplasm. The cytoplasm has granular appearance, which is probably due to high visibility of mitochondria that contain considerable amount of NAD[P]H that is known to produce a strong FMM signal in live skin. It is noted that NAD[P]H is quickly oxidized after the skin excision and is no longer fluorescent. Skin folds are imaged as voids overlaid by intense continuum of green colour. As one can see, no ZnO-nano traces are visible in these images, except an image “4 hr Epi” middle row that exhibits minor traces of ZnO-nano (red). However, this ZnO-nano distribution is distinctly localised at the boundary of the skin fold,

and no diffusive spread of this signal is observable. This presented that ZnO-nano only stayed on the surface or skin folds, when applied on the forearm of subjects from a range of ethnic background, Asian, Caucasian and Indian.

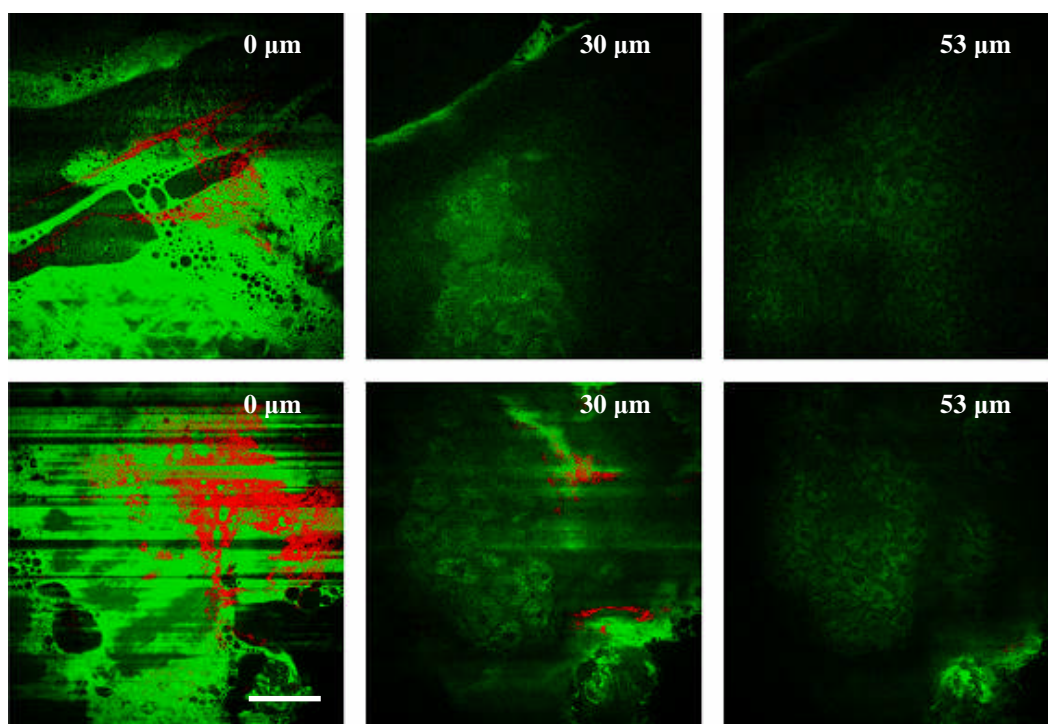


Fig 41. FMM images of ZnO-nano (colour-coded red) distribution in the human skin wrist (colour-coded green) *in vivo* after flexing: 1<sup>st</sup> and 2<sup>nd</sup> rows present images of the ventral and dorsal sides of the wrist, respectively. Numbers on top right side of each image designate depths at which the corresponding image was acquired. Scale bar 30  $\mu\text{m}$

The cell structure and gross architecture of human skin is similar to that observable in Fig 40. In Fig 41, images “0  $\mu\text{m}$ ” and “30  $\mu\text{m}$ ” exhibit streaky appearance. This was likely caused by the sample vibrations due to the heart beating since the instrument was extremely sensitive to movements. The minute movement of the living skin sufficed to introduce the motion artefacts to the images. In most cases, this motion artefact was avoided by tight securing the microscope objective mounting assembly to the skin. The uneven topology of the wrist skin presented greater challenges for secure attachment of the mounting assembly. From these images, ZnO-nano signal is only observable in the “0  $\mu\text{m}$ ” columns, i.e. on the topmost layer of the skin, and dramatically decreased and even disappeared as the imaging depth was increased. Some ZnO-nano signal traces on the “30  $\mu\text{m}$ ” image are due to the local accumulation of the ZnO-nano in a skin fold or dermoglyph. Also, there was no evidence to show that ZnO-nano existing in the intra- and inter-cellular space.

***In vitro* study of ZnO-nano penetration in human skin**

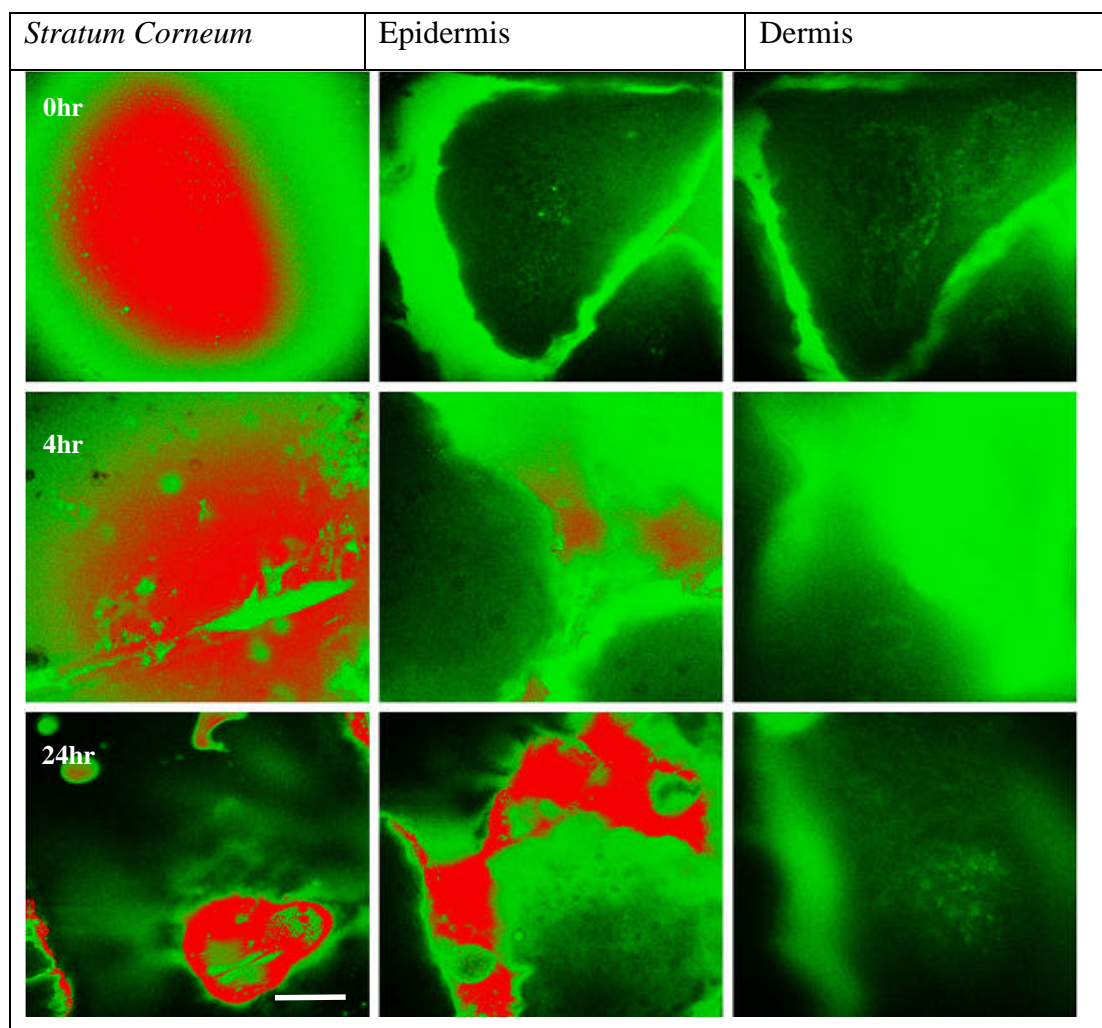


Fig 42. FMM images of ZnO-nano (colour-coded red) distribution in the human skin (colour-coded green) *in vitro*: 1<sup>st</sup>, 2<sup>nd</sup>, 3<sup>rd</sup> rows present results of imaging immediately (0hr), 4 hours (4hr), 24 hours (24hr) after topical application of the sunscreen ZnO-nano formulation. Scale bar 30  $\mu$ m

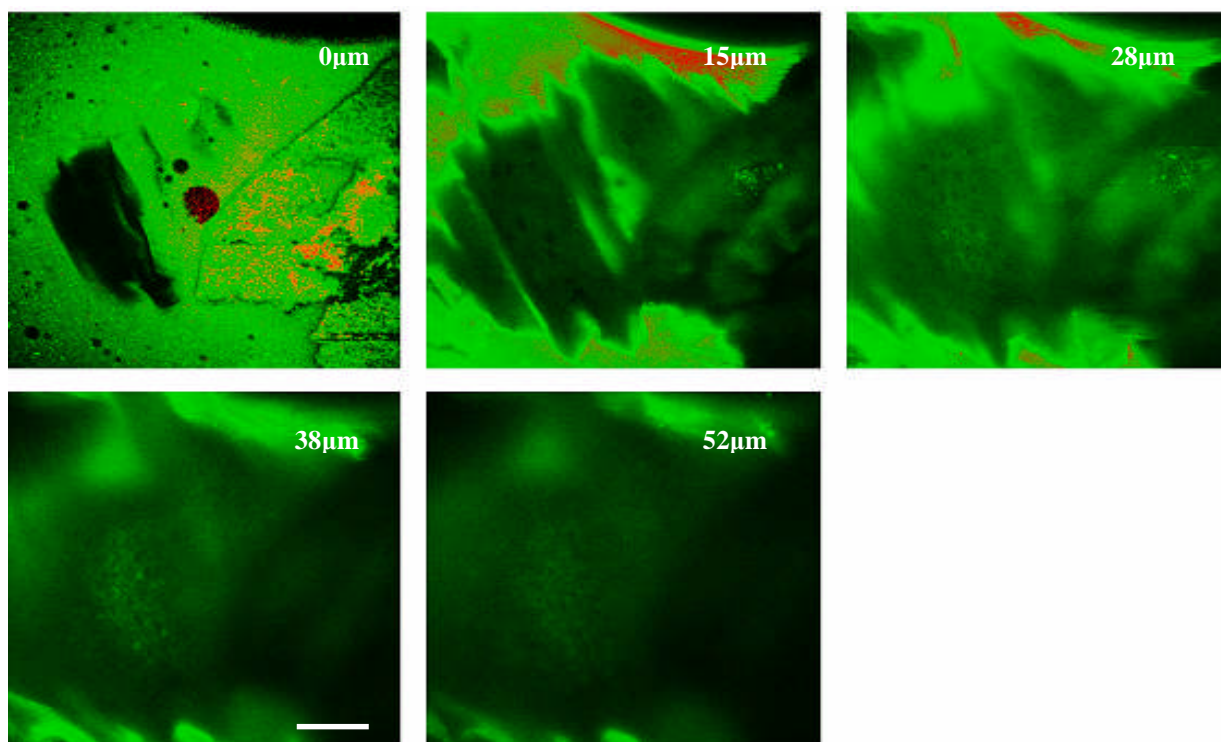


Fig 43. *In vitro* FMM images of ZnO-nano (colour-coded red) distribution in the human skin (colour-coded green) following topical application of ZnO-nano commercial formulation and skin flexing using the setup shown in Fig 36. Numbers in top right corner of each image designates a depth in skin at which each image is acquired. Scale bar 30  $\mu\text{m}$

*In vitro* ZnO-nano transdermal penetrability investigations are presented in Fig 42 and Fig 43. As one can see, ZnO-nano (red-coded) was mainly localised on the surface of human skin, the *stratum corneum*, which presented in saturated green colour. As the image “28  $\mu\text{m}$ ” Fig 43 shows, ZnO-nano is locally distributed in skin folds. The cell population in the central part of the image is not affected by ZnO-nano. No inter- or intra-cellular penetrability is detected (see columns Fig 42 “Epidermis” and “Dermis”), which would be manifested by red or yellow colouration appearing near or between the cell structures. These observations are further confirmed by another experiment whose results are presented in Fig 43, where the excised skin treated topically with ZnO-nano commercial formulation was flexed. It is obvious that ZnO-nano did not pass the topmost skin layer regardless of the skin physical enhancement (via flexing) – no traces of ZnO-nano, except traces with well outlined local boundaries, are seen in deeper skin layers.



### ***In vitro* study of TiO<sub>2</sub>-nano penetration in human skin**

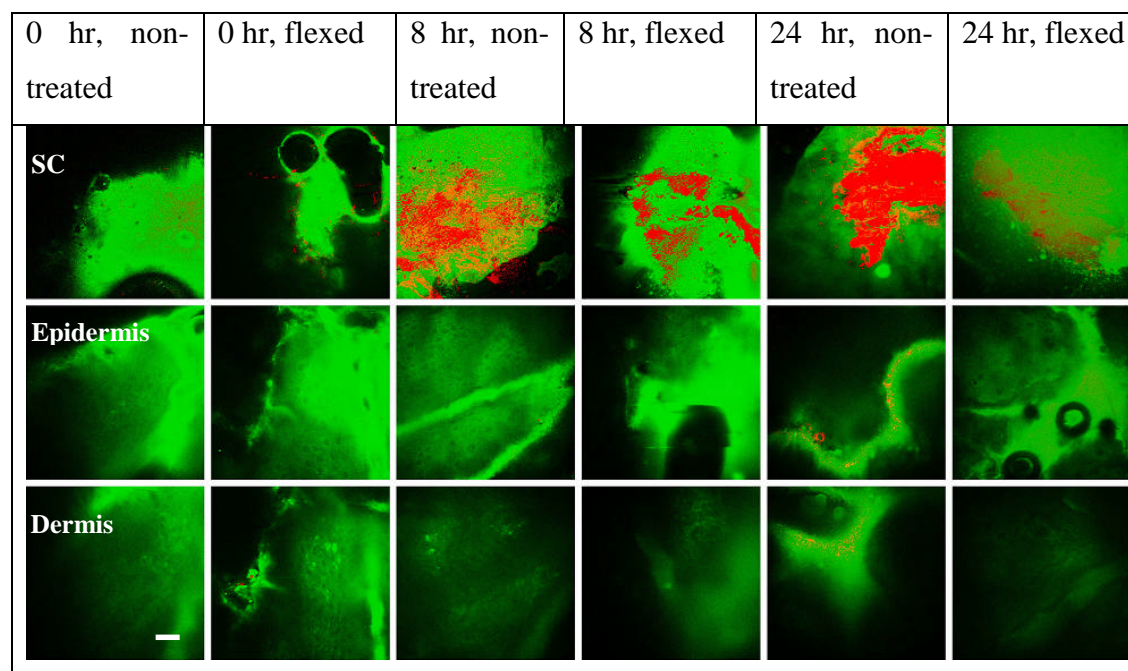


Fig 44. FMM images of TiO<sub>2</sub>-nano/pyrene (colour-coded red) distribution in the human skin (colour-coded green) *in vitro* with or without flexing: 1<sup>st</sup>, 2<sup>nd</sup>, 3<sup>rd</sup> rows represent images of *stratum corneum*, epidermis, and dermis. The column description is given in the text. Scale bar 20  $\mu$ m

In order to prove or disprove the non-penetrability of metal oxide particles of the size range characteristic to typical cosmetic care applications, another type of nanoparticle transdermal penetration, TiO<sub>2</sub>-nano was tested. The TiO<sub>2</sub>-nano/pyrene formulation was applied topically on the excised skin sample, and image immediately ( “0 hr non-treated” ), shortly after flexing using the stretching machine ( “0 hr flexed” ); 8, 24 hours after the formulation application ( “8 hr, non-treated”, “24 hr, non-treated”, respectively), and 8, 24 hours, followed by stretching/flexing ( “8 hr, flexed”, “24 hr, flexed”, respectively). As in case with ZnO-nano treated samples, TiO<sub>2</sub>-nano (red-coded) only appeared on *stratum corneum*, which is color-coded green, and did not depend on the skin physical enhancement treatment, neither it depended on the skin sample exposure to the nanomaterial. Some traces of TiO<sub>2</sub>-nano/pyrene in skin epidermis and dermis after 24 hours of its topical application ( “24 hr, non-treated” ) are well confined to the skin folds that are clearly identified as bright green islands. The bright autofluorescence of these islands are explained by the keratin abundance that is efficiently excited by the ultrashort-pulse laser source. There was no evidence showing that TiO<sub>2</sub>-nano/pyrene appeared in epidermis and dermis cells, or in the extracellular space.



## Qdots

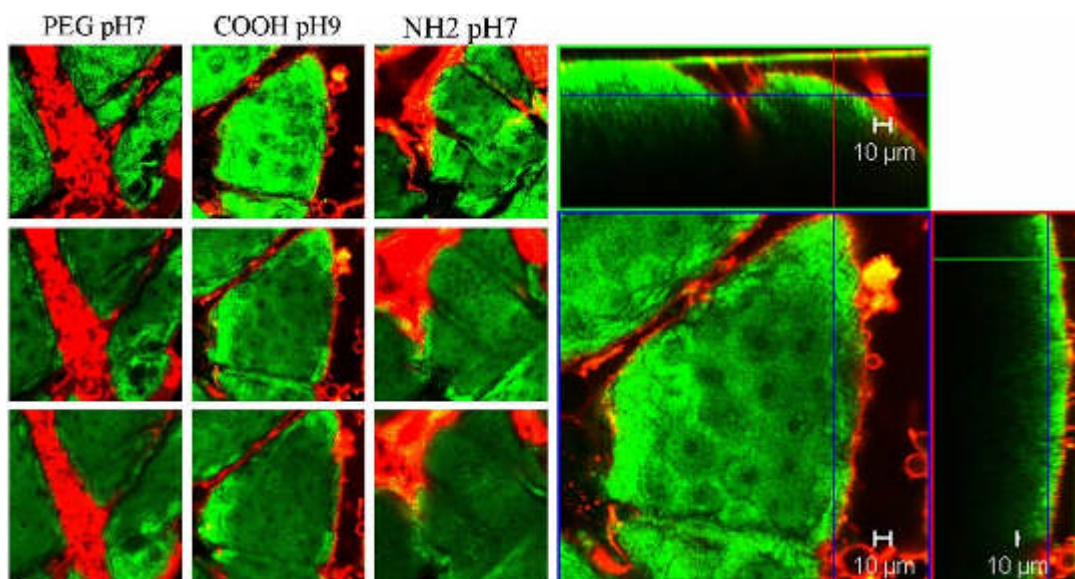


Fig 45. FCSM images Qdots in the intact human skin. Qdots and skin autofluorescence are colour-coded red, and green, respectively. The overlap of these two signals of comparable intensity yields yellow colour. The cross section images have been realized with the Zeiss AIM software. Left: 3D stack images (0µm, 40µm, 80µm) from the first row to the last row. Scale bar 10 µm

Qdots are the brightest of the nanoparticles available in this investigation, and therefore, provided the most stringent and sensitive test of the nanoparticle transdermal penetrability. The results of Qdots imaging using FCSM are presented in Fig 45. It is quite instructive to compare this image panel with that of Fig 39. One can see clearly that Qdots did not appear in the extracellular space (see Fig 39, where they did). The cellular membranes are clearly outlined by bright green boundary converging inwards as dark green having somewhat granular appearance, probably due to colour-dense mitochondria, and converging to dark circles in the middle that are nuclei. Furthermore, the epidermal cells are partitioned into clusters separated by dermaglyphs. This was further confirmed by the cross-section image on the right-hand side, which showed that Qdots micron-thin layer (red-coded) is situated on the human skin surface, but not in the deeper layers of the skin.

The careful observation of the acquired images of skin treated topically with Qdots, allowed us to locate another nanoparticle biological pathway, i.e. transappendageal pathway. Fig 46 shows Qdot nanomaterial in the vicinity of hair follicle canal in skin *in vitro*.

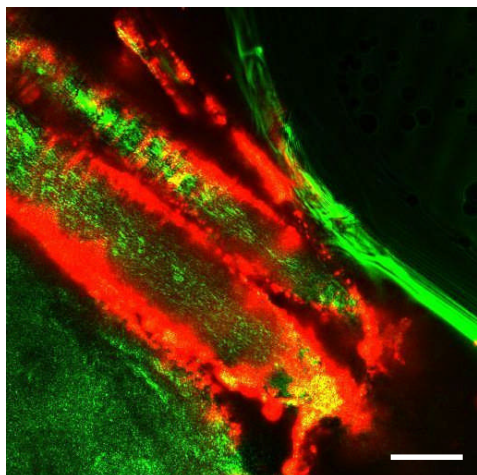


Fig 46. FCSM images of Qdots in the intact human skin. The image was obtained after 24 hours exposure of skin to carboxylic Qdots. Qdots and skin autofluorescence are colour-coded red, and green, respectively. The overlap of these two signals of comparable intensity yields yellow colour. Scale bar 50  $\mu\text{m}$

In Fig 46, a green-colour striated structure (in the diagonal direction) represents an image of the hair follicle. Its outline in red colour is most likely Qdots surface-coated with PEG-COOH that wrapping the hair shaft. Qdots are localized in the hair root forming a pool of the accumulated nanomaterial (the bottom part of the hair shaft, in the “4 o’clock” direction in the image, where the hair shaft is converging to its pencil tip shape). This localisation was observed after 24 hours exposure. It is important to note, however, that Qdots distribution is localised in the vicinity of the hair follicle shaft and no spread into the epidermis space was observed. Epidermis cells are observable in the bottom left corner of the image.

### 3.3.3 Tape-stripped human skin *in vitro*

In human skin, no penetration of the investigated nanomaterial was observed after 8 or 24 hours following its topical application. In order to test the barrier function of the *stratum corneum*, FCSM imaging experiments using skin samples were carried out, where *stratum corneum* layer was removed by the tape stripping method. It can be regarded as physical enhancement of the skin permeability.

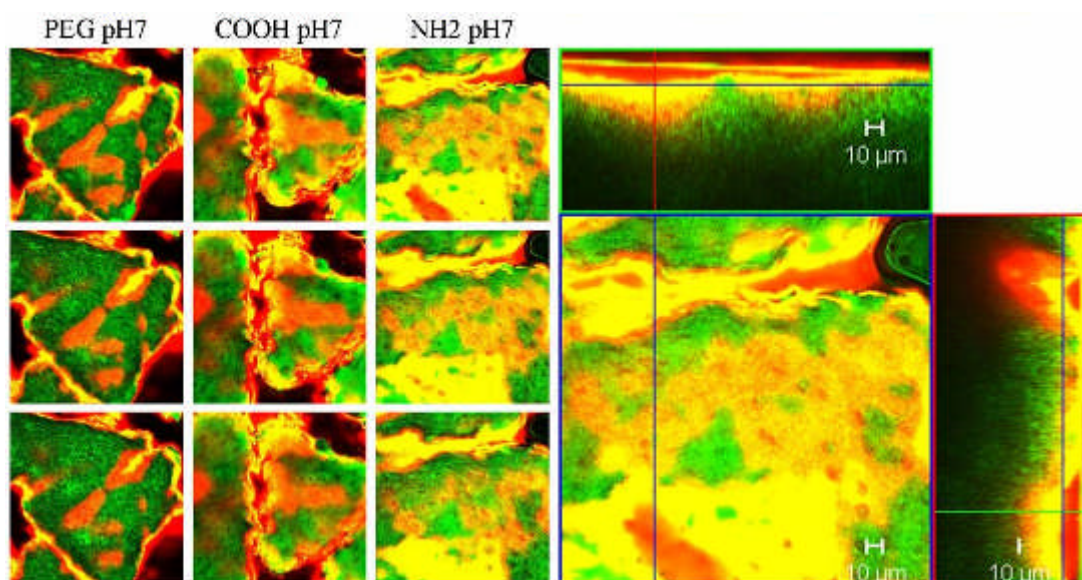


Fig 47. FCSM images of Qdots in tape stripped human skin: Qdots are in red, and skin autofluorescence appears in green, the area where the fluorescence intensity of Qdots and skin autofluorescence are almost the same appears in yellow. Columns (from left to right): z-stack image of PEG, carboxylic and amine Qdots. The cross section images have been realized with the Zeiss AIM software. Left: 3D stack images (0 $\mu$ m, 40 $\mu$ m, 80 $\mu$ m) from the first row to the last row. Scale bar 10  $\mu$ m

Compared with Fig 45, it is clearly observable that the skin images are heavily coloured yellow that indicates the Qdots co-localisation with the skin cellular and extracellular tissue. Firstly, images show the Qdots invasion of the viable layers of skin, i.e. epidermis, and even dermis that took place across the entire exposed area but especially prominent in forms of lobes that advanced in skin depth several tens of  $\mu$ m. Secondly, different responses of the skin treated with three types of Qdots were noted. In particular, amino-surface-activated Qdots reveal vast delocalisation of the Qdots distribution in the skin tissue, whereas this delocalisation effect is quite modest in case of the skin topical treatment with PEG.

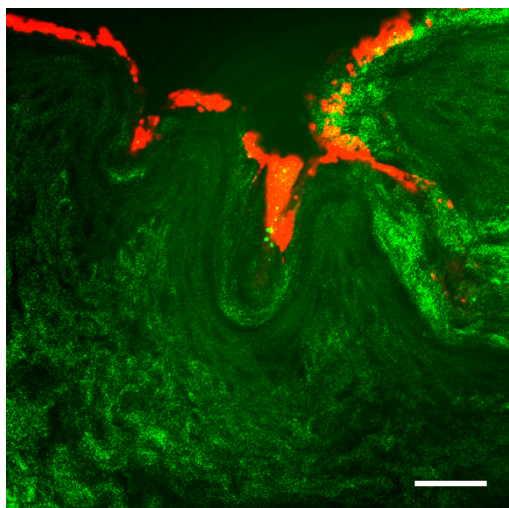
### 3.3.4 Human skin with chemical enhancement *in vitro*

Other than physical enhancement, specialised chemicals are used to ease the nanoparticles transdermal penetration. Some of these chemicals are 1,8-cineol eucalyptol, menthol and limonene (terpene). It has been proved that they are able to change the lipid structure and state (Narishetty and Panchagnula, 2005; Lopez-Cervantes, 2006). Therefore, the *stratum corneum* may be rendered penetrable to nanoparticles of the size range greater than that matching the physical gap of the lipid bilayer (13 nm). In these series of experiments, the hypothesis of the enhanced transdermal penetrability of nanoparticles sized 14-35 nm under test was put. Salicylic carboxylic, 2-ethylhexyl ester is a commonly used sunscreen agent. It has been

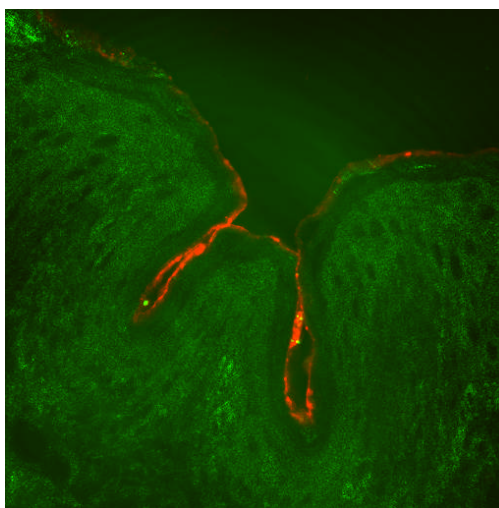
found that it can also function as a chemical skin enhancer (Hayden, 2005). Its enhanced penetrability of nanoparticles to skin also needs to be tested.

In order to establish a negative control sample benchmark, imaging experiments using the non-treated human skin were also carried out. The results are presented in Fig 48.

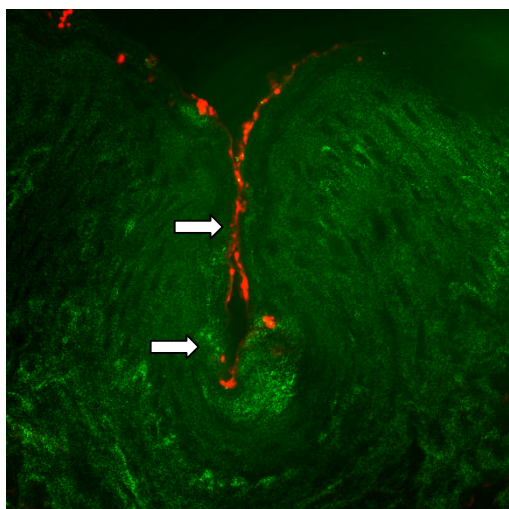
### *Qdots*



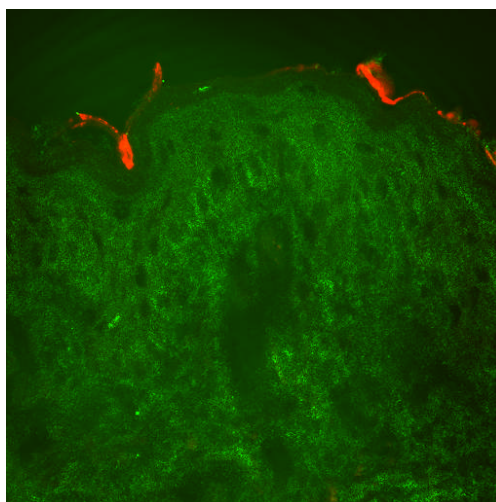
Human skin Amine 8.3, 8 hr



Amine 8.3, 8hours CE

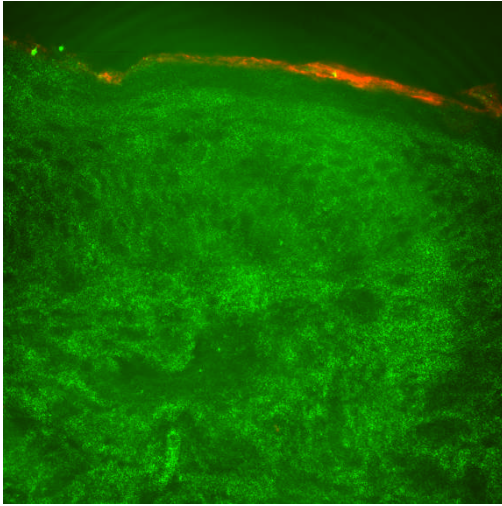


Human skin Amine 8.3, 24 hr  
(hair follicle, pointed by white arrow)

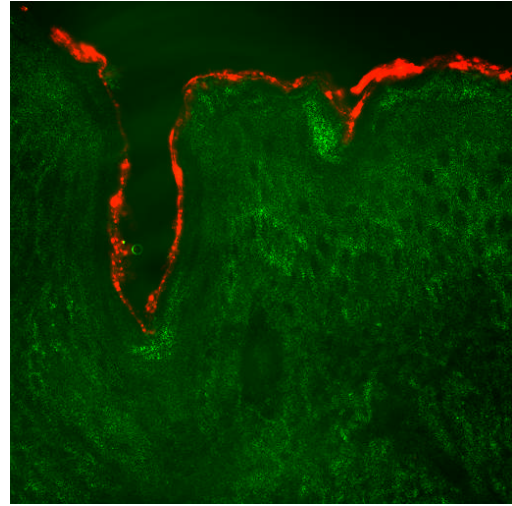


Amine 8.3, 24 hr CE

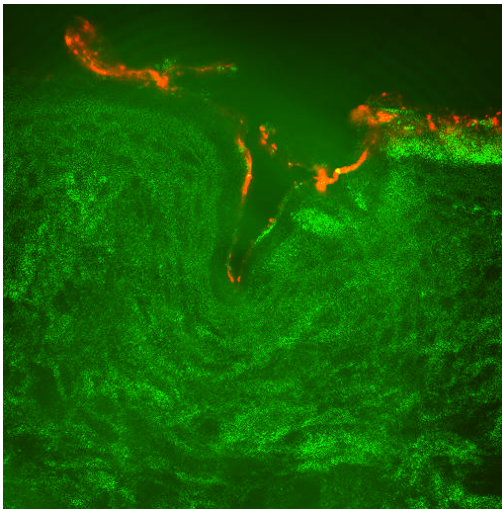




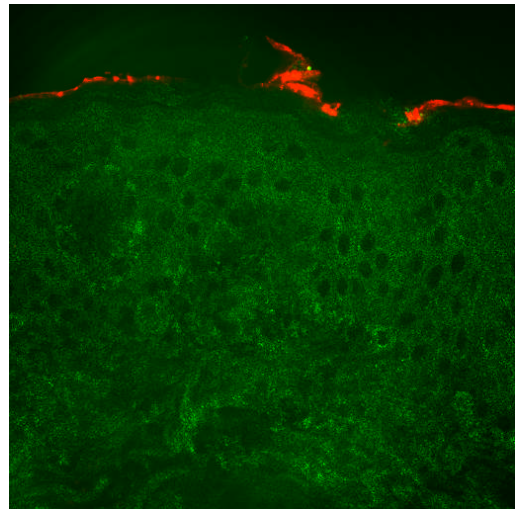
Carboxylic 9, 8 hr



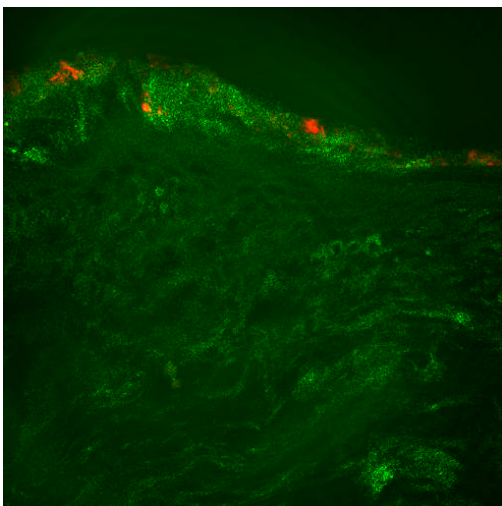
Carboxylic 9, 8 hr CE



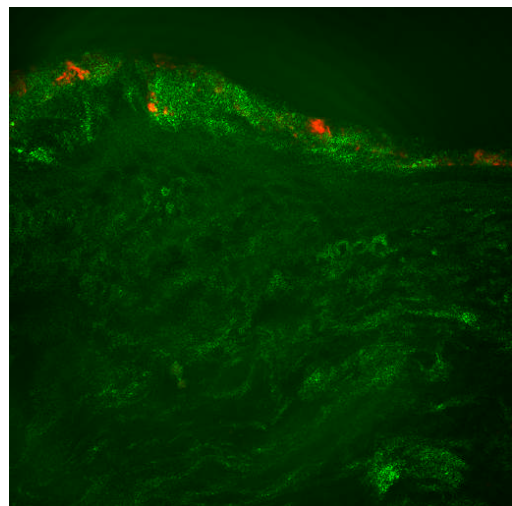
Carboxylic 9, 24 hr



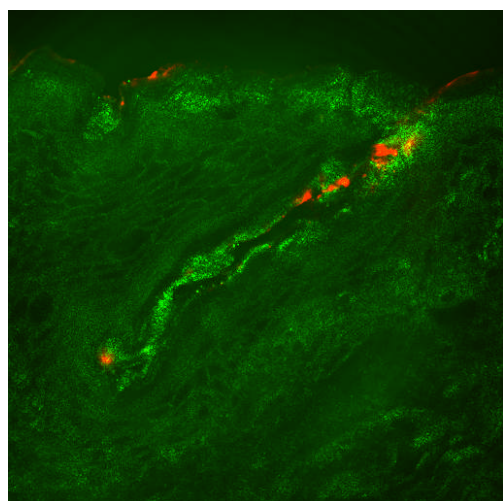
Carboxylic 9, 24 hr CE



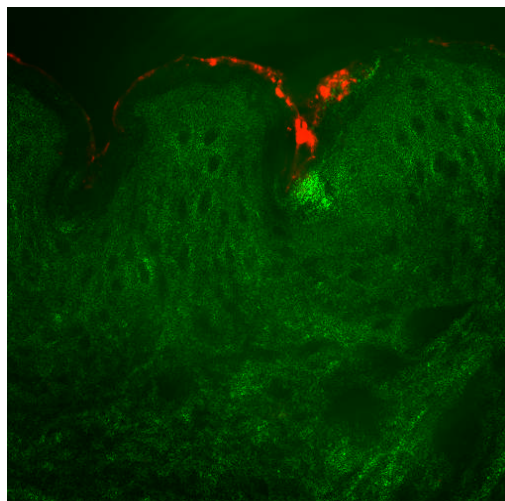
PEG 8.3, 8 hr



PEG 8.3, 8 hr CE



PEG 8.3, 24 hr



PEG 8.3, 24 hr CE

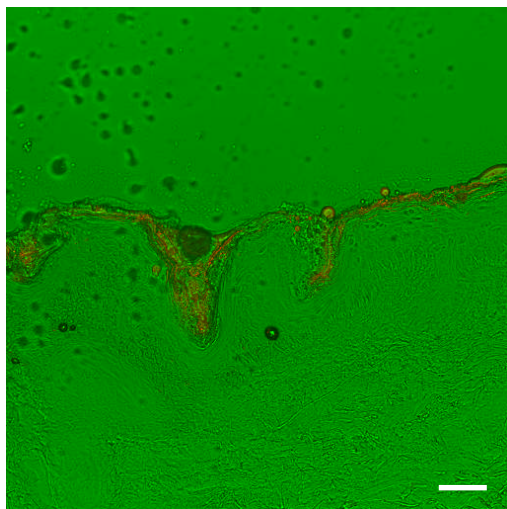
Fig 48. FCSM images of excised human skin cross-sections. Left column, non-treated sample; right column, chemically enhanced sample. Qdots distribution, skin autofluorescence are colour-coded red, green, respectively. Pixels of comparable fluorescence intensity of Qdots and skin autofluorescence yield yellow colour. Each image contains caption, with the following notations: the label designates the type of the Qdot surface functional group; number designates the value of pH of the Qdot topical formulation; number “hr” designates a number of hours imaging session was carried out following the formulation topical application. CE designates skin pre-treated with chemical enhances. Four chemical enhancers showed the same result under FCSM. Scale bar 50  $\mu$ m

In the typical experiment, the skin patch was treated with the one of the four chemical enhances using the protocol, as described in Sub-Section 3.2.5. The sample was topically treated with Qdots surface-functionalised with amino, carboxyl, or PEG (designated as Amine, Carboxyl, or PEG in Fig 48). For example, image caption “Carboxylic 9, 24 hr CE” should read as the sample was first treated with the chemical enhancer (CE) followed by topical application of Qdots surface functionalised with carboxylic acid (Carboxyl), in formulation of pH9 (9), and imaged 24 hours after incubating the skin sample (24hr)

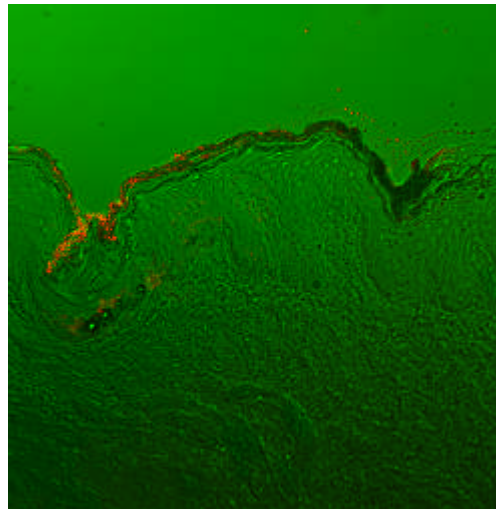
From the images, it is clear that, Qdots stayed on the skin surface in case of the non-treated samples (“Carboxylic 9, 8 hr”, and “PEG 8.3, 8 hr”), or fell into skin folds (a small cavity on the skin surface, as shown in “Human skin Amine 8.3, 8 hr”), or trapped in the hair follicles (large canal piercing the skin from *stratum corneum* to dermis, as shown in “Human skin Amine 8.3, 24 hr”). Importantly, the Qdots that were entrapped in the hair follicles did not spread in the surrounding tissues even after 24 hours. After the treatment with the enhanced chemicals, the four chemicals showed essentially the same Qdot penetration pattern as that of the non-treated skin samples (“Carboxylic 9, 8 hr CE”). Qdot localisation in the hair follicle shaft is evident from the image (“Human skin Amine 8.3, 24 hr”). For example, the amino-surface-functionalised Qdots in formulation of pH8.3, after 8 hours, penetrated into the hair follicle but were localised around the upper half of the hair follicle shaft (“Human skin Amine

8.3, 8 hr”). It is interesting to note that after 24 hours, the Qdots predominantly fell down to the hair root (“Human skin Amine 8.3, 24 hr”).

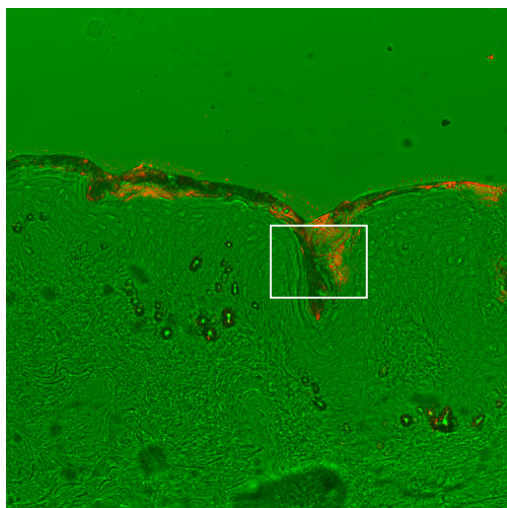
### *ZnO-nano*



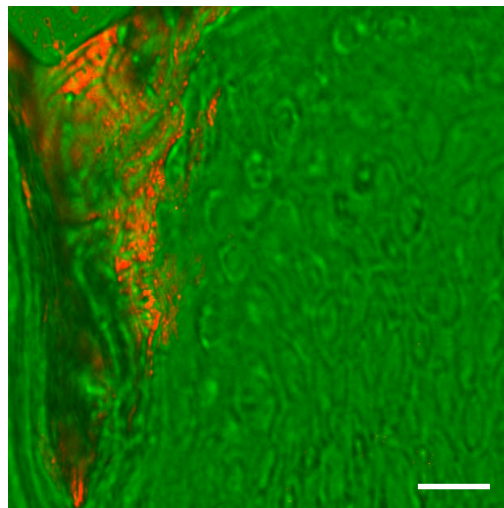
ZnO-nano, 8 hr



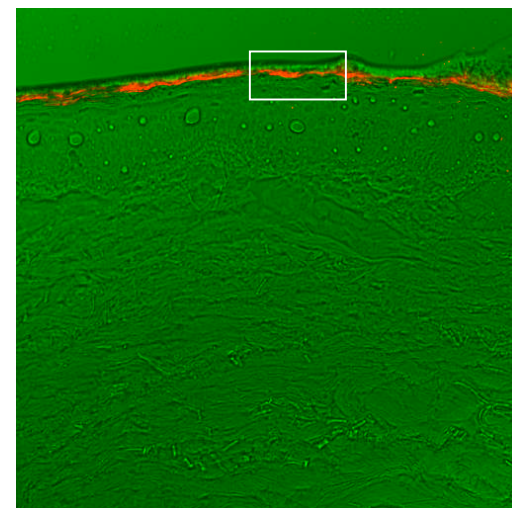
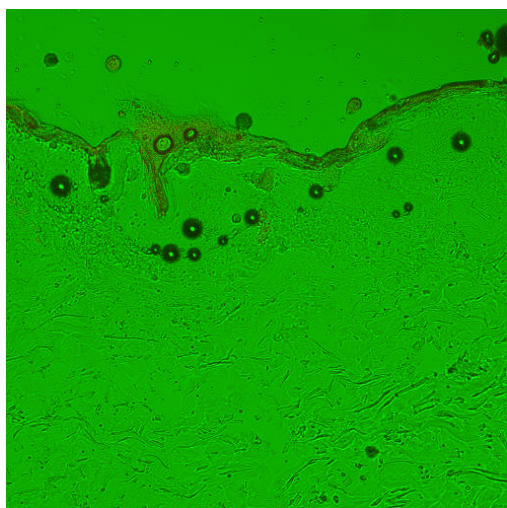
ZnO-nano, Menthol, 8 hr



ZnO-nano, Limonene, 8 hr



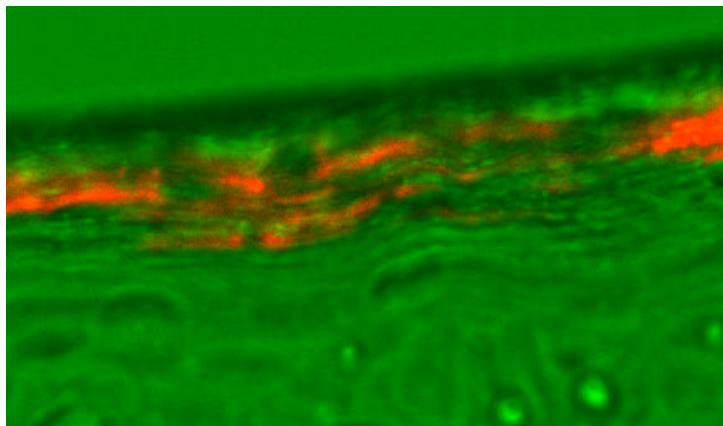
ZnO-nano, Limonene, 8 hr, zoomed-in  
A square area in ‘ZnO-nano, Limonene, 8 hr’



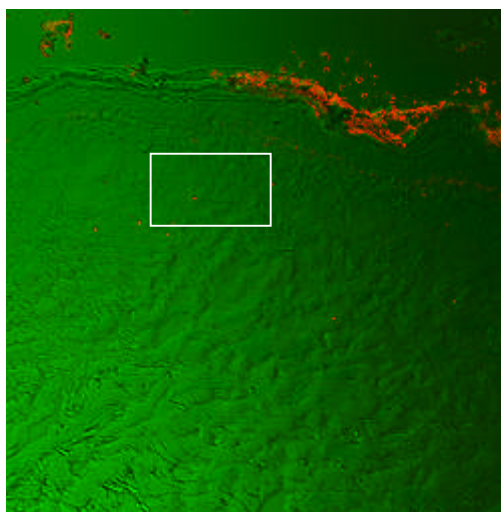


ZnO-nano, 24 hr

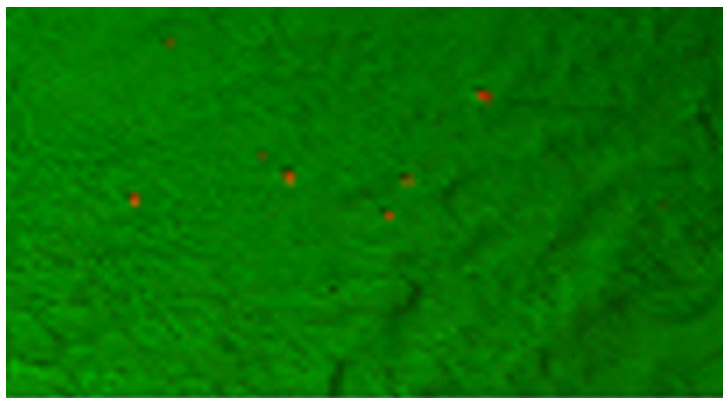
ZnO-nano, Menthol, 24 hr



ZnO-nano, Menthol, 24 hr, zoomed-in, a white square in 'ZnO-nano, Menthol, 24 hr'



ZnO-nano, Limonene, 24 hr



ZnO-nano, Limonene, 24 hr, zoomed-in square in 'ZnO-nano, Limonene, 24 hr'

Fig 49. FMM images of the excised human skin cross-section topically treated with ZnO-nano. ZnO-distribution, skin transmission morphology is colour-coded red, green, respectively. ZnO-nano, 8 hr: non-treated sample after incubation in 35°C water bath for 8 hours; ZnO-nano, Menthol, 8 hr: skin sample pre-treated with the chemical enhancer, menthol, after incubation in 35°C water bath for 8 hours; ZnO-nano, Limonene, 8 hr: skin sample with the chemical enhancer, limonene, after incubation in 35°C water bath for 8 hours. Full-scale images, scale bar 50 µm; zoomed-in images, scale bar 20 µm



It is evident that ZnO-nano stayed on the non-treated skin surface, after 8 and 24 hours of incubation in a room-temperature water bath (see for example, Fig 49 “ZnO-nano, 8 hr”). As a result of the skin pre-treatment with menthol and 2-ethylhexyl ester (these two chemicals gave the same results), ZnO-nano is visualised within the lipid bilayers of *stratum corneum* after 24 hours, as shown in ‘ZnO-nano, Menthol, 24 hours, zoomed-in’. One can see that the upper layers in the epidermis morphology (green) is co-localised with the ZnO-nano distribution (red). As a result of the skin pre-treatment with limonene and 1, 8-cineol (these two chemicals gave the same results), the ZnO-nano distribution is observable in epidermis and even dermis layers of the skin after 24 hours, shown as the spots within the square in ‘ZnO-nano, Limonene, 24 hours’.

### **3.3.5 SEM/EDS results**

#### **JSM6300F**

Qdots surface-functionalised with Amine pH8.3, PEG pH8.3, and Carboxyl pH9 were applied on the excised human skin, and followed the biomicrowave sample preparation protocol, as described in Sub-Section 3.2.6. Tape-stripping was done after 8 hours of Qdots incubation on skin. The purpose of the type-stripping was to isolate Qdots that penetrated through the *stratum corneum* from the Qdots that remained in the superficial layers of the *stratum corneum*. The results were shown in Fig 50. Using samples cut in cross-sections, it can be easily seen the cell structure and where Qdots appear from *stratum corneum* to dermis (see Fig 51).

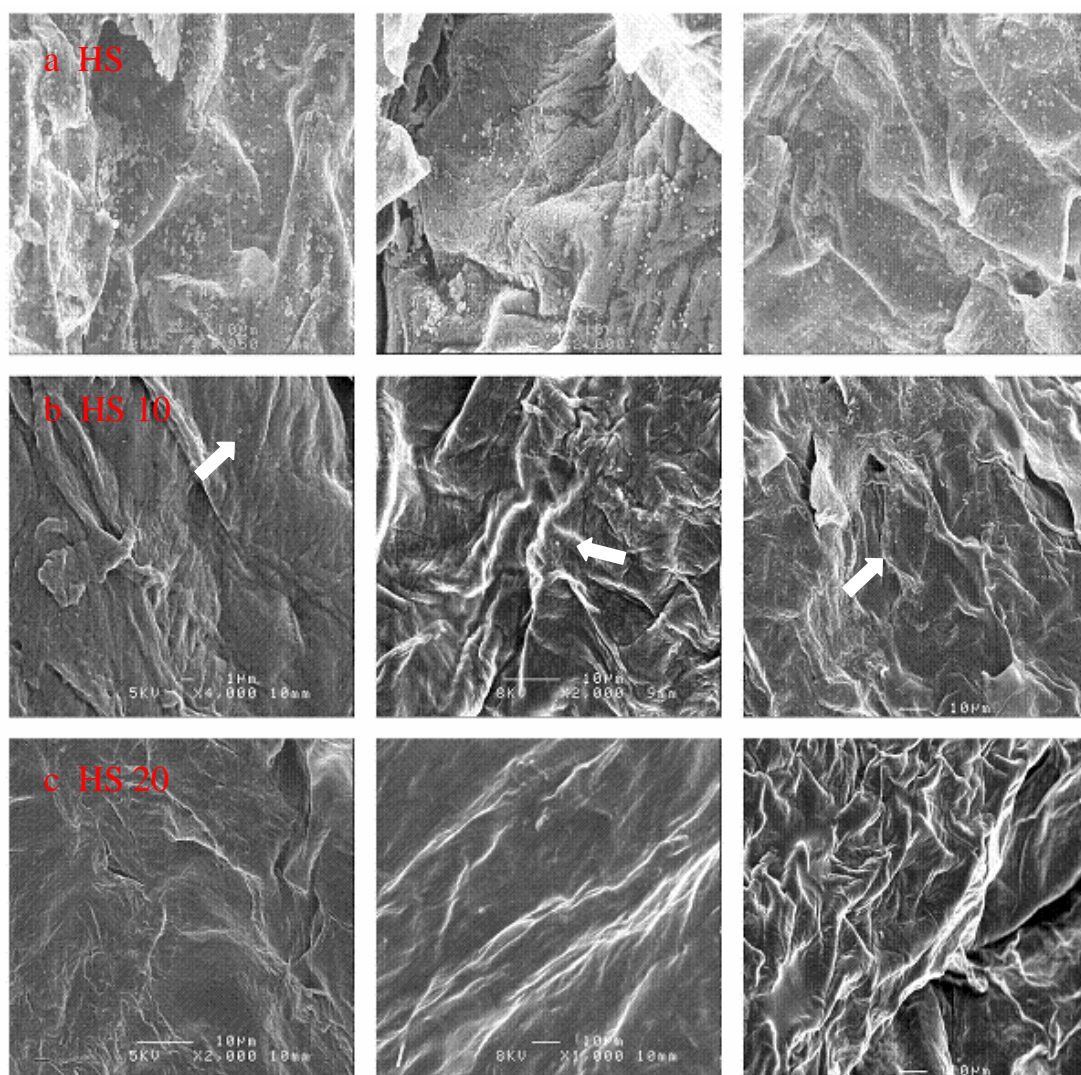


Fig 50. SEM images of the intact and tape-stripped human skin (skin surface topology): 1<sup>st</sup>, 2<sup>nd</sup>, 3<sup>rd</sup> columns present images of the human skin treated with amino-, PEG-, carboxyl- Qdots, respectively. Row (a) HS: Intact human skin; Row (b) HS 10: 10-times tape stripped human skin; Row (c) HS 20: 20-times tape-stripped human skin. Arrows show where the Qdots are on skin surface

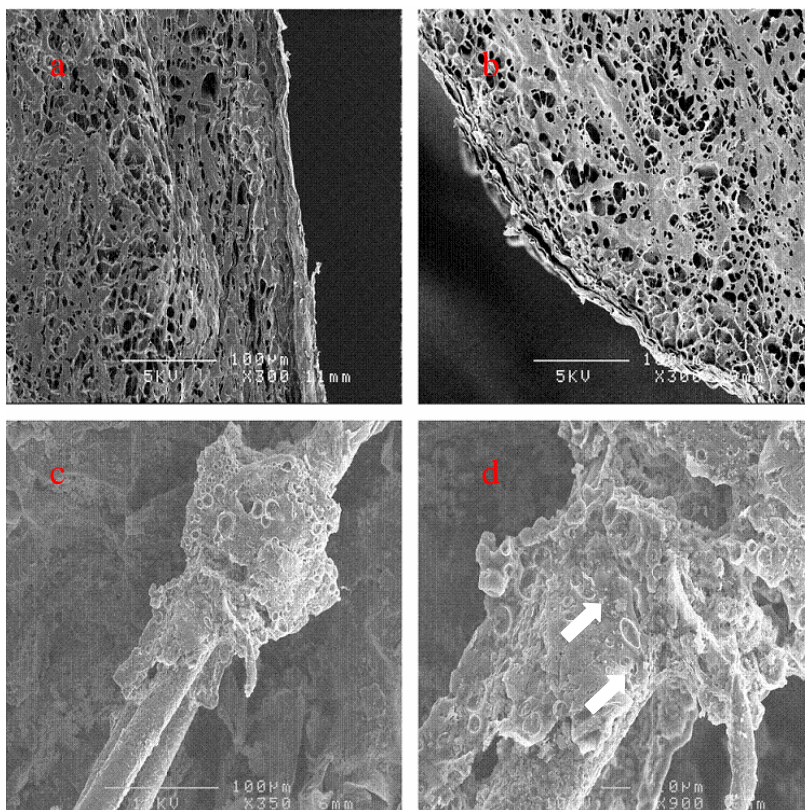


Fig 51. SEM images of the human skin *in vitro* subjected to Qdot topical surface treatments. Cross-sectional view of the human skin topically treated with amino-Qdots (pH8.3) followed by tape-stripping: Image (a): 10 times tape-stripped, Image (b): 20 times tape-stripped. Full-scale image (c) and zoomed-in image (d) of the human skin treated with PEG-Qdots (pH8.3). Note a hair follicle in the image centre

The Qdots existed in skin in aggregated form, with typical size range reaching 200 nm, and individually. The size of the individual Qdots was ascertained by the previous characterisation of individual Qdots (see Sub-Section 2.2.3, table 3). For example, as specified in the Qdots data sheet, amino-, carboxyl-, and PEG-surface functionalised Qdots have mean diameter of 15, 14, and 35 nm, respectively. They are shown as white dots on the dim-grey skin background in image (d) of Fig 51. It is evident that Qdots remained either in the *stratum corneum* or fell in the skin folds, as shown in Fig 50 first row. In the tape stripped skin, the number of Qdots decreased or completely diminished as the number of stripping increased (c.f. images in the first column Fig 50, second row (10 times stripping) and third row (20 times stripping)). Only two aggregation dots are left on the surface, which was pointed by white arrows in the second row image of Fig 50. From the cross-section image (see Fig 51, first row), the skin structure of different layers was clearly presented, wherein no traces of Qdots were observed. The zoomed-in image of the hair follicle showed that Qdots were around the hair root, pointed by a white arrow. This confirmed the earlier observations made based on

FCSM images: Qdots did not pass through the *stratum corneum* but remained on the top skin surface, in skin folds or in hair follicle shafts.

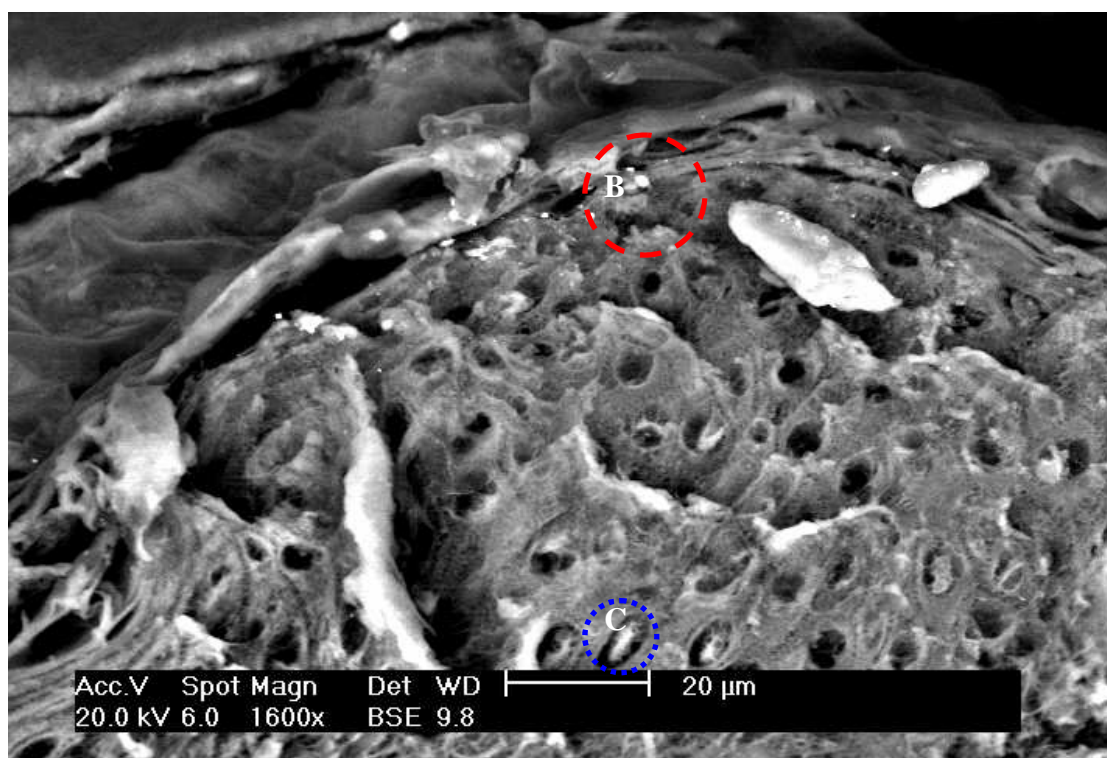
### **Philips XL30 (SEM/EDS)**

As can be appreciated from the presented above SEM images, it was difficult to recognise and identify Qdots against the skin background. In order to solve this problem, the backscattering imaging method was employed. Sample preparation was described in Sub-Section 3.2.6. Using this imaging technology, all the chemical elements of atomic weight greater than that of carbon exhibit positive imaging contrast (brighter than the skin grey background). However, the other ambient elements heavier than carbon should also become bright in a back-scattered image, hence making Qdot recognition difficult. Therefore, SEM/EDS spectrum was used to facilitate the Qdot visualisation in skin.

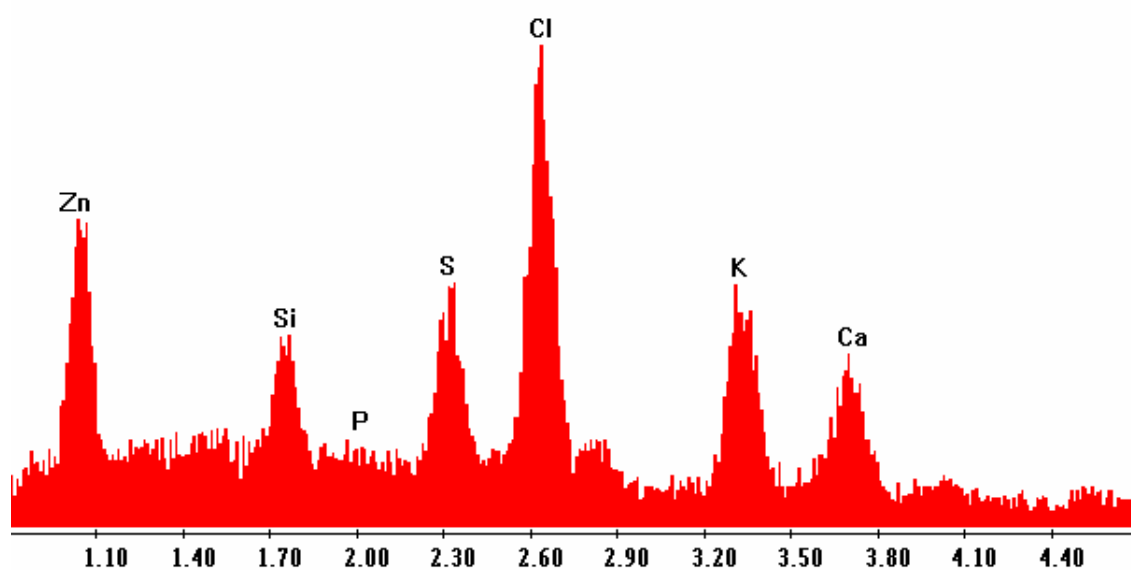
SEM/EDS spectrum shows the characteristic x-ray peaks of all the elements in the selected area in the backscatter image. In order to unambiguously identify ZnO-nano in the sampled area, Zn and O peaks need to be registered in the EDS-spectrum. Similarly, in case of the Qdots featuring a ZnS shell, Zn and S peaks need to be registered in the spectrum.

The samples used in this experiment were the excised human skin patches topically treated with the ZnO-nano and Qdot formulations, where the skin was either pristine or pre-treated with the chemical enhancers.

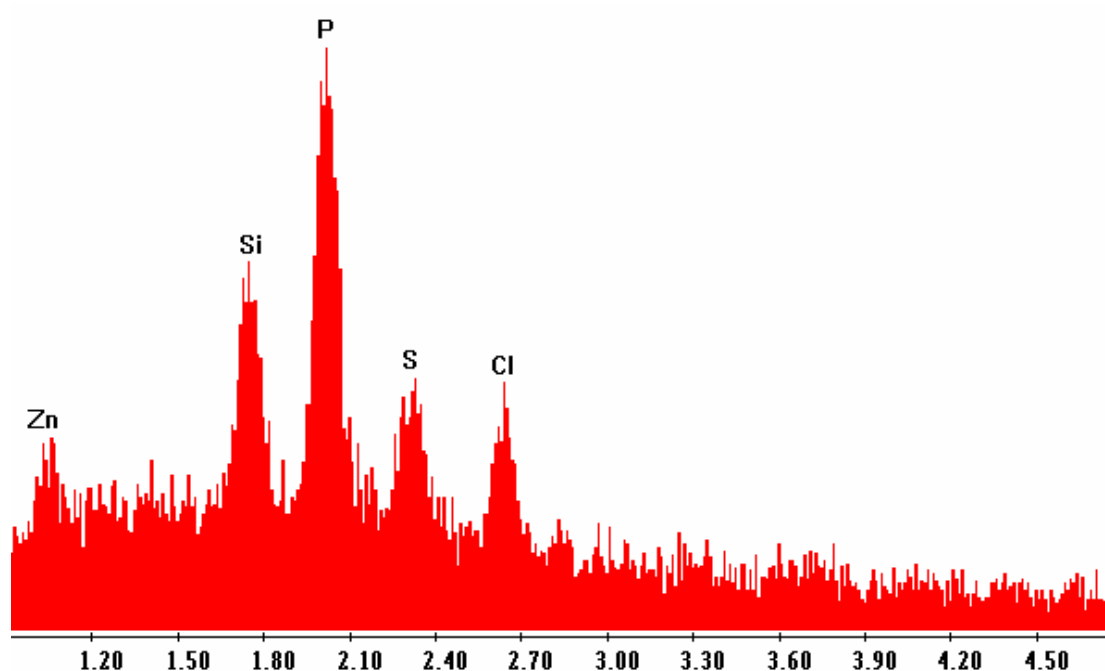




A. Back-scattered image of skin morphology



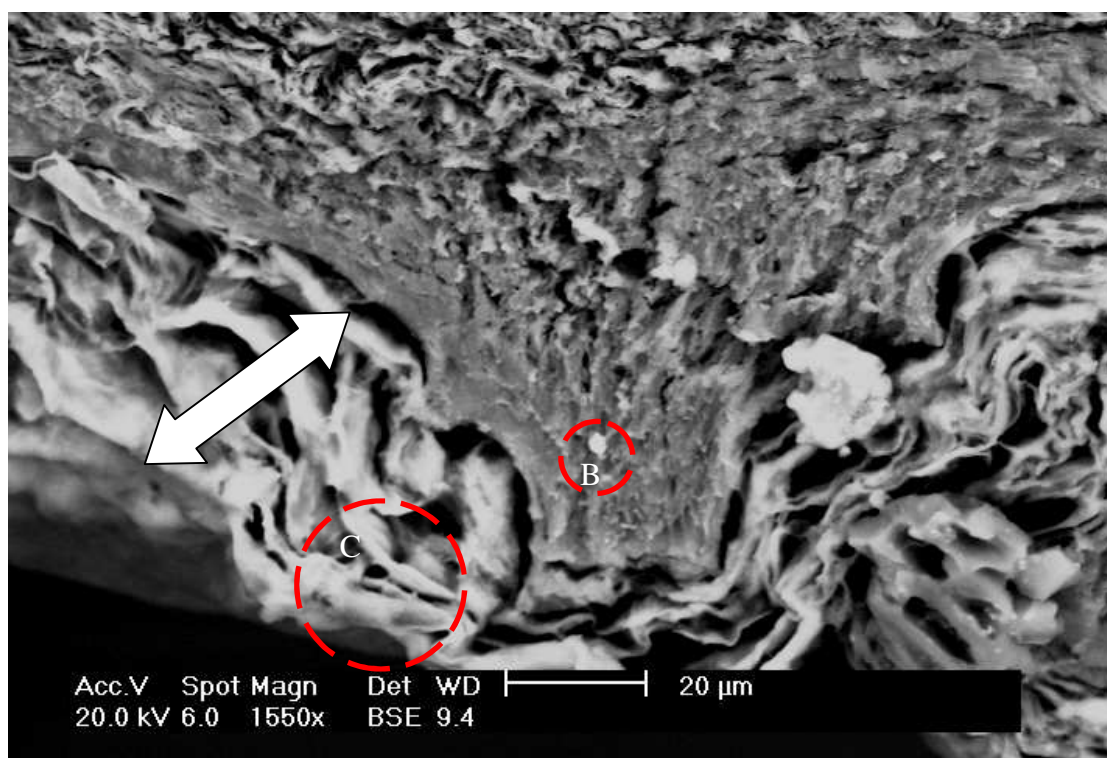
B. EDS spectrum of components in circle B in image A



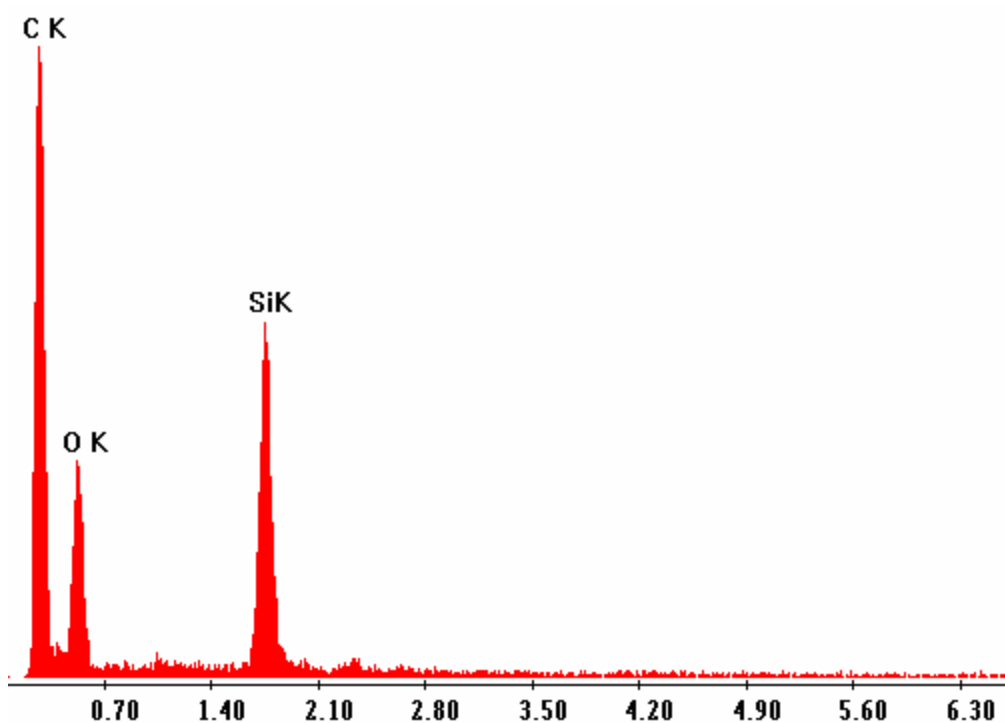
C. EDS spectrum of components in circle C in image A

Fig 52. Back-scattered SEM image and EDS spectra of amino-Qdots (pH8.3) on human skin treated with the chemical enhancer, menthol. EDS spectra B and C were sampled from the areas b and c in the image A. Designation of the chemical elements: Zn, Zinc; Si, silicon; P, phosphorus; S, sulphur; Cl, chlorine; K, potassium; Ca, calcium. The abscissa axis readings are in electron-Volts (eV)

From the EDS spectrums, it can be easily determined that the bright spots on skin surface B and within cells C in the back-scattered image A were Qdots since both Zn and S peaks were shown in the spectrum, which were the components of the Qdot shell. This represents a convincing proof that amino-Qdots passed through *stratum corneum* and were taken up by the cells after the chemical treatment with menthol.



A. Back-scattered image of skin morphology

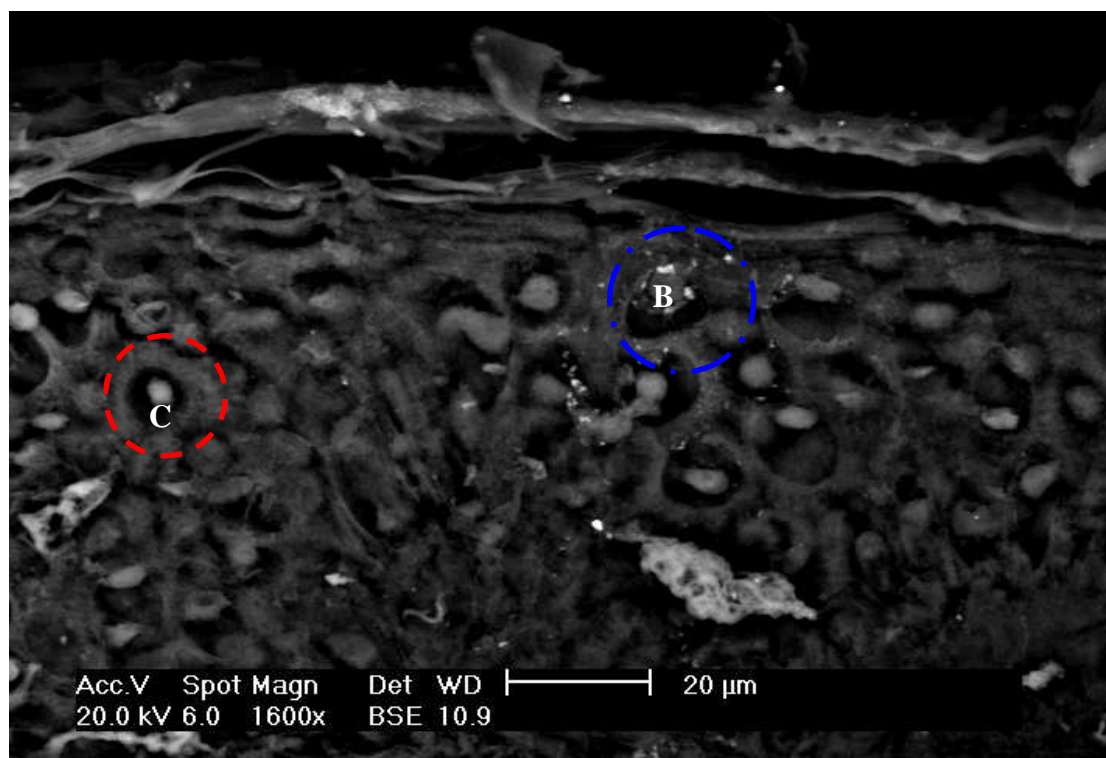


B. EDS spectrum of atomic species sampled in circle B and C in image A

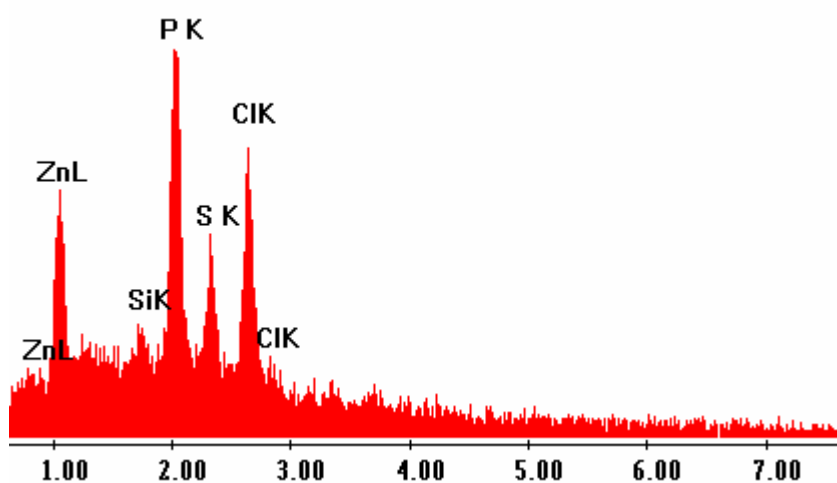
Fig 53. An SEM back-scattered image and an EDS spectrum of carboxyl-Qdots (pH9) in the excised human skin topically treated with the chemical enhancer, menthol. The registered chemical element designation: C, carbon; O, oxygen; Si, silicon. The abscissa axis readings are in electron-Volts (eV)

Image A in Fig 53 presents a low-magnification, cross-sectional view of the excised skin, where several skin layers can be delineated. *Stratum corneum* is presented (pointed by the

arrow in the image) as a uniform layer of densely packed dead cells. Below the *stratum corneum* (upwards in image A) a granulated layer of the viable epidermis is observable. The EDS spectrum shows that the white spots on *stratum corneum* (in circle C) and in the epidermis (in circle B) are characterised by the x-ray characteristic peak of silicon, but not that of zinc or sulphur. In addition, no characteristic Zn and S x-ray peaks were observed in the EDS spectra sampled at the other areas of the epidermis and dermis. This rules out the existence of carboxyl-Qdots in the epidermis topically treated with menthol.

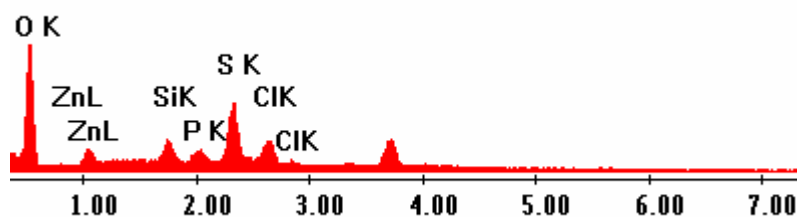


A. Back-scattered image of skin morphology



B. EDS spectrum of components in circle B in image A

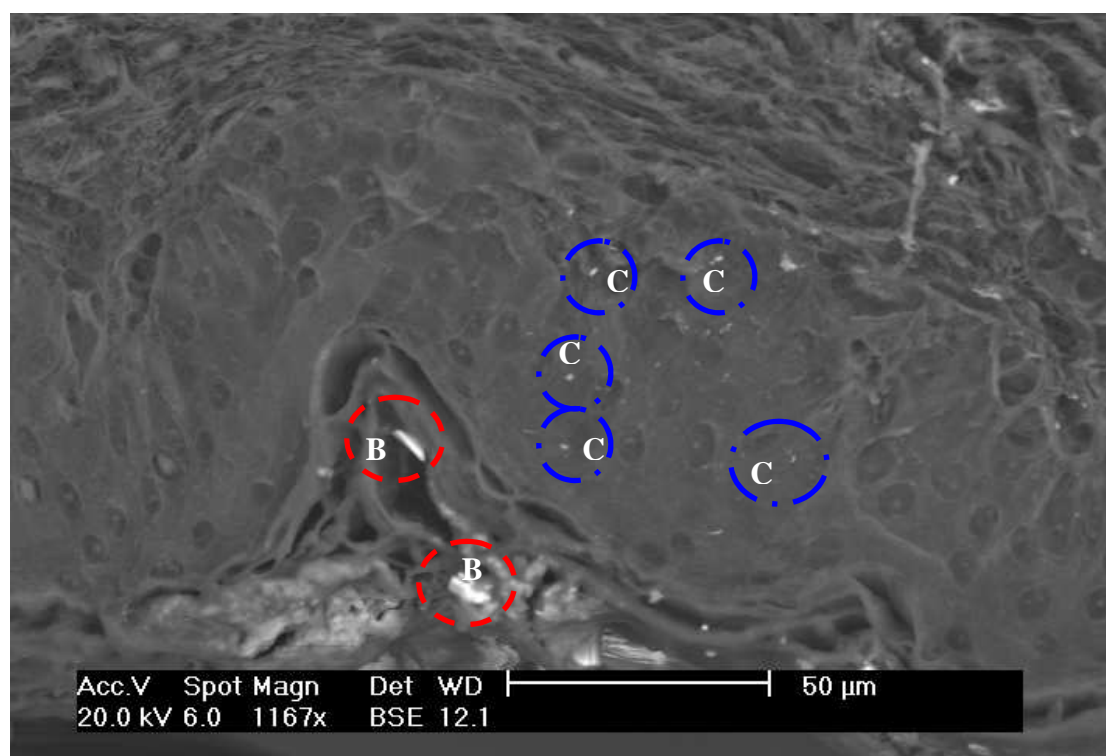




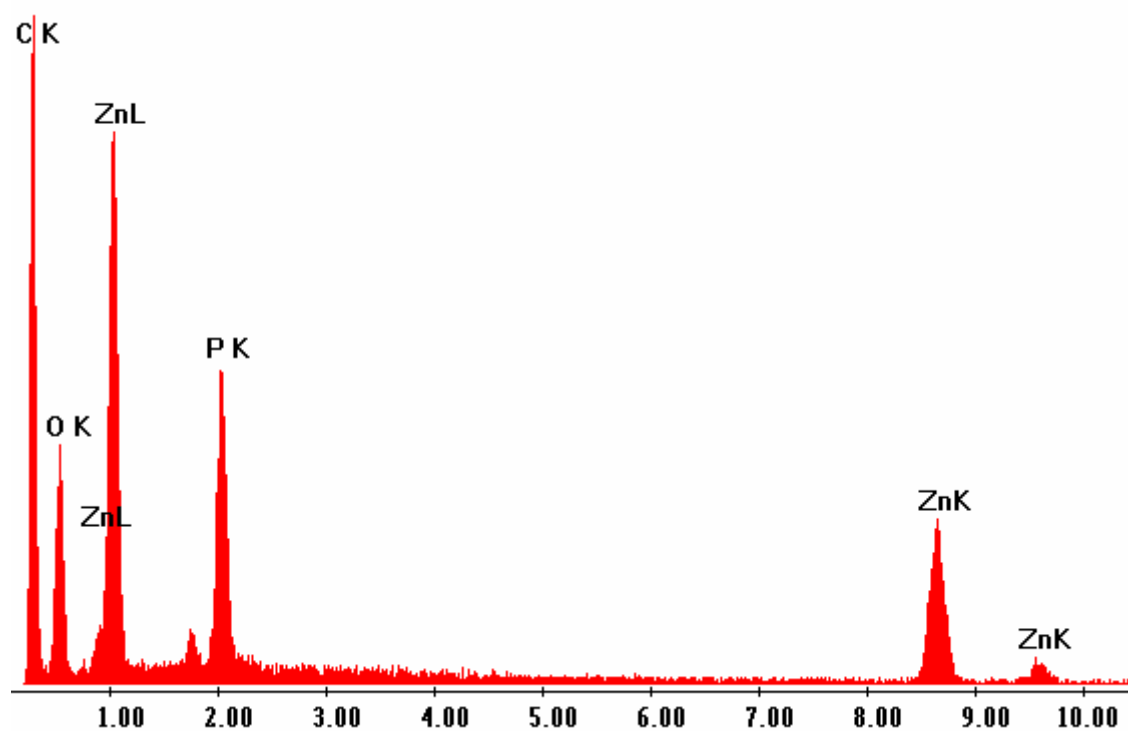
C. EDS spectrum of components in circle C in image A

Fig 54. A back-scattered image and EDS spectra of PEG-Qdots (pH8.3) in the excised human skin topically treated with the chemical enhancer, menthol. The chemical elements designation: C, carbon; O, oxygen; Si, silicon; Zn, Zinc; Si, silicon; P, phosphorus; S, sulphur; Cl, chlorine; K, potassium; Ca, calcium. K, L designate the core electron shells of an atom. The abscissa axis readings are in electron-Volts (eV)

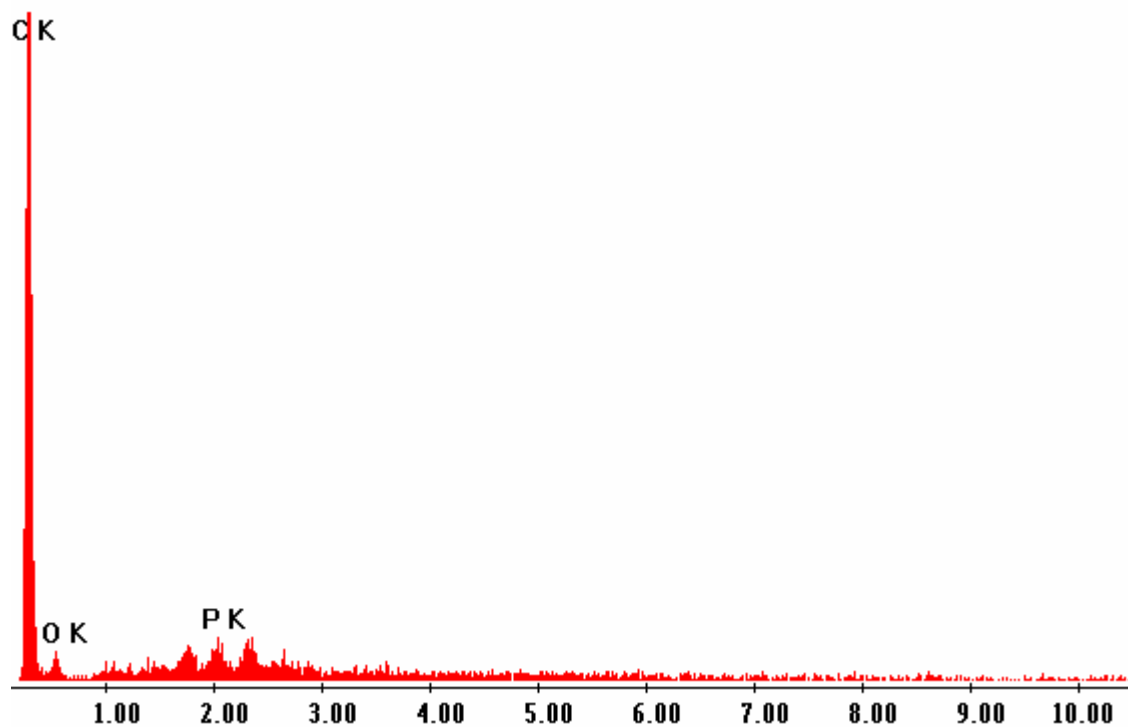
From image A of Fig 54, it can be seen that on the top of the image, is cracked layers of dead cells which is *stratum corneum*. Beneath this layer, epidermis cells are shown as black holes with bright tissue surround. In each cell, there is a round bright spot (see circle C) and also some brighter spots around cells (see circle B). Analysis of the EDS spectra show that the bright intracellular inclusions in circle B and C on the epidermis in image A both contain distinct x-ray peaks of Zn and S. This strongly points to the Qdots origin of these inclusions that are most likely represent Qdots passed taken up the epidermis cells. It shows that the PEG-Qdots passed the skin barrier, *stratum corneum* and internalised in the cells.



A. Back-scattered image of skin morphology



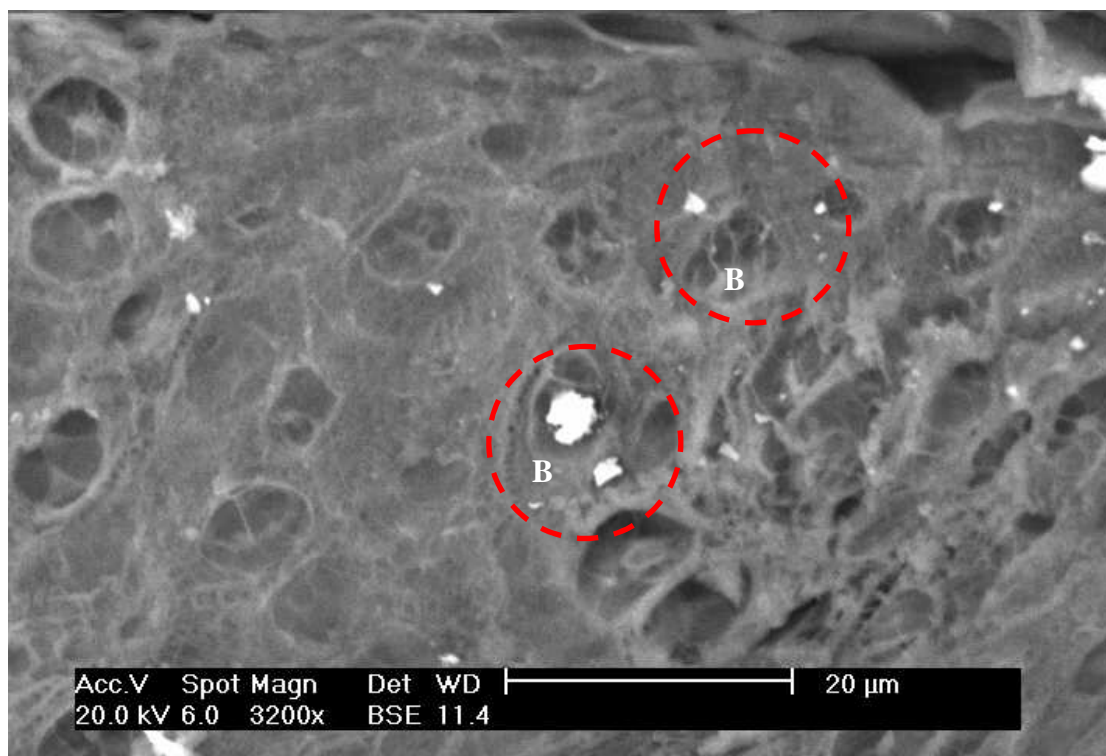
B. EDS spectrum of atomic species in circle B in image A



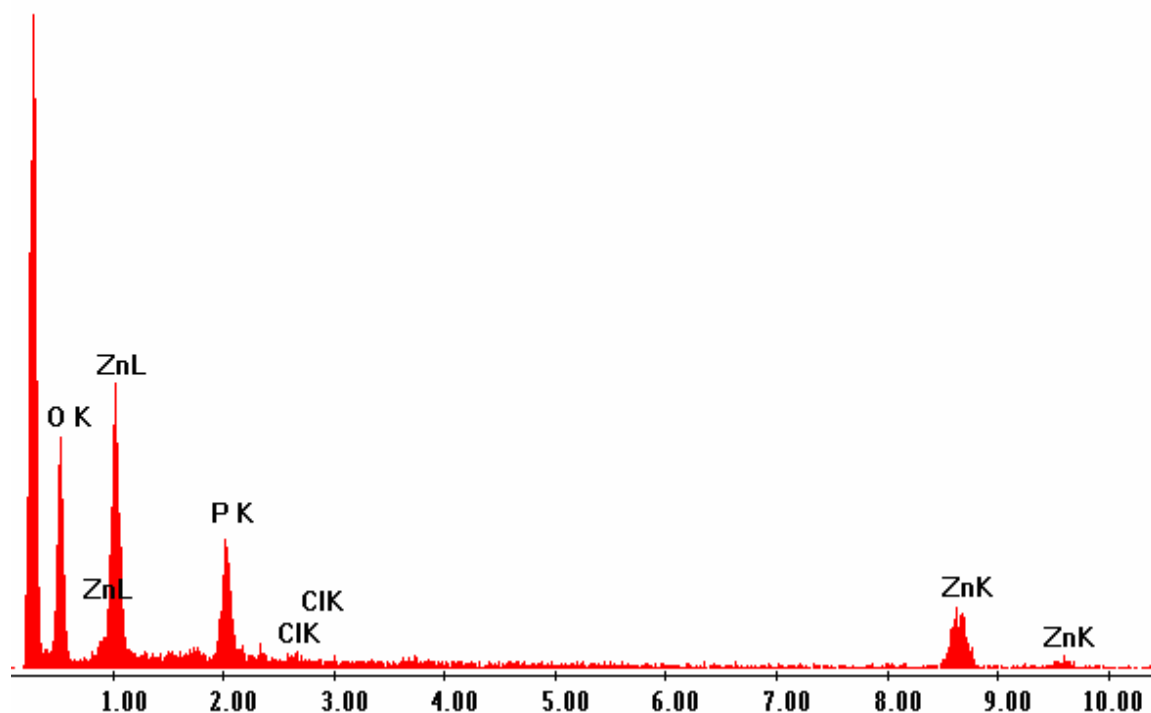
C. EDS spectrum of atomic species in circle C in image A

Fig 55. A back-scattering image and EDS spectra of the pristine excised human skin topically treated with the ZnO-nano formulation; negative control sample. The chemical elements designation: C, carbon; O, oxygen; Zn, Zinc; P, phosphorus; S, sulphur; Cl, chlorine; K, potassium; Ca, calcium. K, L designate the core electron shells of an atom. The abscissa axis readings are in electron-Volts (eV)

In image A, some bright spots were found on the top of *stratum corneum* (circle B) and on epidermis and dermis (circle C). The analysis of the materials in circle B showed that EDS-spectra B revealed Zn L and Zn K x-ray characteristic energy peaks corresponding to the binding energy of the two electron core shells. This meant they were ZnO-nano. At the same time, sampling EDS-spectra C at various sites in the viable epidermis and dermis areas (circle B) did not reveal any inclusions associated with Zn.



A. Back-scattered image of skin morphology



B. EDS spectrum of atomic species in circle B in image A

Fig 56. A back-scattered image and an EDS spectrum of ZnO-nano on the excised human skin topically treated with the chemical enhancer, menthol. The chemical elements designation: C, carbon; O, oxygen; Si, silicon; Zn, Zinc; P, phosphorus; S, sulphur; Cl, chlorine; K, potassium; Ca, calcium. K, L designate the core electron shells of an atom. The abscissa axis readings are in electron-Volts (eV)

Image A of Fig 56 presents a high-magnification cross-sectional image of the excised skin pre-treated with menthol and treated topically with ZnO-nano formulation. In image A, it can be seen clearly the epidermis cells representing as round cavities. Two bright inclusions in this image fragments were analysed using EDS (circled B). From the EDS spectrum, the bright intracellular inclusion featured both Zn L and Zn K characteristic x-ray peaks. This provides strong evidence that ZnO-nano inclusions are most likely ZnO-nano aggregates when passed the *stratum corneum* and were taken up by the cells or remained in around them.

### 3.3.6 FLIM results *in vitro*

The lifetime of ZnO-nano was measured in the lab although it has been referenced. This is for two important reasons: one is that it is a calibration method for the FLIM system and the other is that it is a second confirmation of the claim that ZnO-nano lifetime is indeed around 200 ps so that it can be discriminated from other skin fluorophores. Table 5 shows the excitation wavelength and experimental measured lifetime in four channels of ZnO-nano and human epidermis.

**Table 5. The results of lifetime measurement of ZnO-nano and human skin**

<b>ZnO-nano (experimental measured)</b>				
	<b>Channel 1 ( ps)</b>	<b>Channel 2 ( ps)</b>	<b>Channel 3 ( ps)</b>	<b>Channel 4 ( ps)</b>
Ex 710 nm	264.6	893.8	1048.8	974.1
Ex 800 nm	141.1	191	607.7	0
<b>Human skin, depth 8.2 <math>\mu</math>m</b>				
Ex 800 nm	1080.6	1107.9	1722.3	1598.4
<b>Human skin, depth 40 <math>\mu</math>m</b>				
Ex 800 nm	891.3	900.8	1636.7	1281.8
<b>Human skin top applied with ZnO-nano, depth 6 <math>\mu</math>m</b>				
Ex 740 nm	398.6	786.1	1112.6	0
Ex 800 nm	556.5	1014.6	100	100
<b>Human skin top applied with ZnO-nano, depth 40 <math>\mu</math>m</b>				
Ex 740 nm	348.8	457.8	994.1	0
Ex 800 nm	545.7	100	100	100

Ex, excitation wavelength; ps, picoseconds

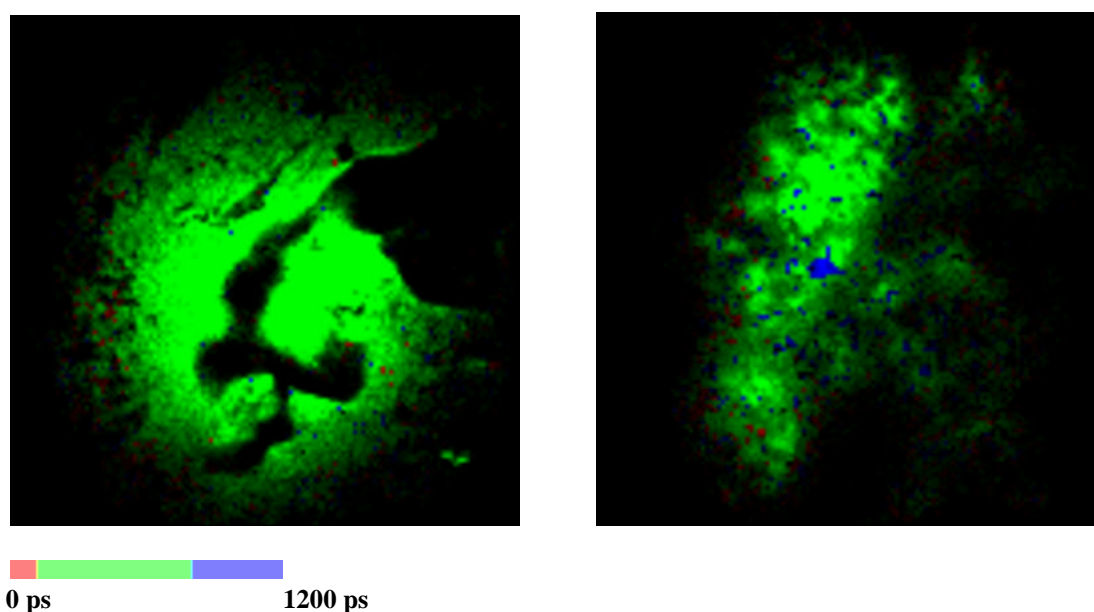


Fig 57. Lifetime map of human skin (*in vitro*), with ZnO-nano topically applied. The lifetime was measured upon two-photon excitation of the ZnO-nano and skin autofluorescence at a 740-nm fundamental wavelength left-, right- hand-side images were acquired at depths of 6  $\mu$ m, 40  $\mu$ m, respectively

From the results of ‘human skin’, one can see that the skin fluorophore dominant lifetime varied versus the depth and different channels. This is because fluorophores emission lights

were separated by four channels at each depth and thus different dominant lifetimes were collected. The ZnO-nano signal in channel one was only considered (detail in Sub-Section 2.3.4 FLIM setup). ZnO-nano dominant lifetime was measured to be ~200 ps. From the lifetime values of skin with top application of ZnO-nano, it showed that there was no ZnO-nano at depth 6  $\mu\text{m}$  and 40  $\mu\text{m}$  since the dominant lifetime values were all above 300 ps in channel one. A comprehensive study of FLIM application to delineate ZnO-nano and skin autofluorescence signals was not carried out. However, it showed the potential of this technique to the application of luminescent nanoparticle characterised by  $\tau$  distinctly different from that of the skin intrinsic fluorophores for penetration to the transdermal research.

### 3.3.7 Summary of results

**Table 6. Summary of the optical and scanning electron microscopes results on nanoparticle penetration in the human and porcine skin *in vivo* and *in vitro***

	<b>ZnO-nano 26-30 nm</b>	<b>TiO<sub>2</sub>- nano 14 nm</b>	<b>Qdots-COOH (carboxyl) 14 nm</b>	<b>Qdots-NH<sub>2</sub> (amine) 15 nm</b>	<b>Qdots- PEG 35 nm</b>
<b>Pristine porcine</b>	<b>FMM(-)</b>	<b>FMM(-)</b>	<b>FCSM(+)</b>	<b>FCSM(+)</b>	<b>FCSM(+)</b>
<b>Pristine Human</b>	<b>FMM(-) FLIM(-)</b>	<b>FMM(-)</b>	<b>FCSM(-)</b>	<b>FCSM(-)</b>	<b>FCSM(-)</b>
<b>Tape- stripped Human</b>			<b>FCSM(+)</b>	<b>FCSM(+)</b>	<b>FCSM(+)</b>
<b>Chemical enhancers Human</b>	<b>FMM(+) SEM(+)</b>		<b>FCSM(-) SEM(-)</b>	<b>FCSM(-) SEM(+)</b>	<b>FCSM(-) SEM(+)</b>

FMM: Fluorescence multiphoton microscope; FCSM: Fluorescence confocal microscope; FLIM: Fluorescence lifetime imaging; SEM: Scanning electron microscope; (+): penetration observed; (-): penetration not observed

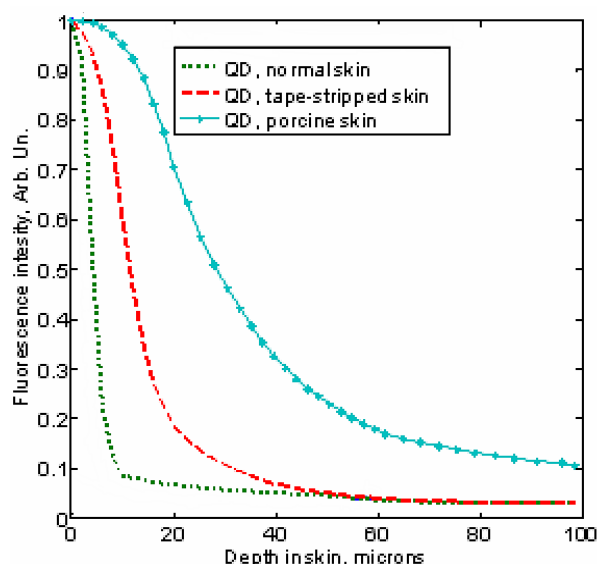


Fig 58. A plot of Qdot fluorescence intensity decay versus the depth in skin; Penetration of Qdots after 24 hours in different types of skin; Depth ranges of 0 - 20  $\mu\text{m}$ , 20 - 80  $\mu\text{m}$ , and 80 to 100  $\mu\text{m}$  demarcates *stratum corneum* , epidermis, and dermis, respectively

Fig 58 shows that fluorescence intensity of Qdots verse depth. It is assumed that the Qdot integral signal intensity depends linearly on the Qdot concentration in skin. The fluorescence intensity decayed rapidly in the intact human skin. It is considerably diminished well within *stratum corneum* layer. In contrast, in tape stripped and/or porcine skin, fluorescence intensity is detected in the epidermis; the effect is especially profound in the porcine skin. The read-out z-values were corrected by considering refractive index of skin that was assumed of mean value of 1.4.

### 3.4 Discussion

In the research team, a comprehensive study of nanoparticle penetration in skin *in vivo* and *in vitro* using the advanced optical microscopy and electron microscopy techniques has been carried out.

First of all, the results of the previous observations have been confirmed which reported the Qdots penetrability in the porcine skin. (Ryman-Rasmussen, 2007). They used Qdots in commercial formulation at pH8.3 and pH9 applied to porcine skin mounted in perfused Franz cells. The penetration was observed using FCSM. They have found that, although the porcine skin is generally penetrable to Qdots, there was a difference in extent of the penetration depending on the surface coating. The penetration was the most extensive for amino-Qdots, rather than for carboxyl- and PEG- Qdots. In this work, however, it had not found a preferential epidermal uptake of the amino-Qdots, rather the finding suggest that Qdot surface

fictionalisation had little and random effect on the Qdot uptake in the skin cellular tissue.

Establishing nanoparticle transdermal penetrability benchmark using the porcine skin, human skin penetrability was investigated. It was found that the principle difference between the human and porcine skin penetrability to nanoparticle of 14-35 nm size range. The results are consistent with these published for ZnO-nano by Roberts (Roberts 2006): ZnO-nano penetrability through human skin (Cross, 2007) was at least 20 times less than through porcine skin (Gamer, 2006). The importance of this finding was that observation of penetration of Qdots through porcine skin, such as for fullerenes (Rouse, 2007), may not necessarily take place through human skin. On the other hand, many studies suggesting a similarity between human and porcine skin. However, they have been based on either skin morphology (Jacobi, 2005; Jacobi, 2007) or penetration of small drug molecules (Schmook, 2001; Dalton, 2006). The study strongly suggests that porcine skin represent a poor model of human skin penetrability to nanoparticle in the size range of 15 – 40 nm.

The application of Qdots (Qdots) with different surface coating and environment pH helped us to understand more about Qdots penetration mechanism. Qdots used in this study were in the size range characterised by mean diameters of 14 nm, 15 nm and 35 nm, for their respectively surface fictionalisation with PEG-COOH, PEG-NH<sub>2</sub> and PEG. This work is to the knowledge the first that shows Qdots, applied on human skin and evaluated in FCSM did not penetrate into the viable epidermis.

As alkaline pH are known to impair skin permeability (Thune, 1988; Sznitowska, 2001), studies were repeated at neutral pH, in which Qdots remained stable, i.e. non-agglomerated. All three Qdots penetrated similarly at neutral pH into human and porcine skin as was found for original pH (8.3 or 9). It was just in porcine skin, the penetration rate was slowed down a little bit.

The hypothesis that human *stratum corneum* has been also tested provided an efficient barrier to the nanoparticle transdermal penetration. *Stratum corneum* of human skin removed by tape-stripping enabled Qdots penetration in the top layers of epidermis after 8 hours, and to a greater extent after 24 hours. A number of studies have shown that breaching *stratum corneum* by skin stripping or by skin tears, can promote nanoparticles absorption. Tinkle has shown that 0.5- and 1- $\mu$ m-diameter fluorescein isothiocyanate (FITC) conjugated dextran beads penetrated through the tear human skin (Tinkle, 2003). That damage has been evaluated,



such as mild abrasion or cleansing products may impair the *stratum corneum* and facilitate nanoparticles penetration into skin.

Also, tape stripping technique was used to confirm the results of intact human skin. In Fig 50, tape stripping (10 and 20 times) after several hours of Qdots application on top of skin was done, the number of Qdots decreased or became zero as the number of stripping increased. It meant that the Qdots did not penetrate into deeper skin layers but just stayed on the *stratum corneum* or maybe penetrated a little bit into the *stratum corneum* layer (only for the separated Qdots). Some aggregation still existing after tape stripping was because the tape stripping could not take them away.

Secondly, it was necessary to broaden the range of nanoparticles that tested for the skin penetrability. It has been tested that the size range of the metal oxide nanoparticles is similar to that of Qdots, i.e. 14 – 35 nm. The *in vitro* ZnO-nano results showed that there was no penetration occurred in human skin or porcine skin after 8 hours or even 24 hours. The nanoparticle penetration was not influenced by physical treatment in human skin, although slightly influenced in case of the porcine skin. The results on the TiO<sub>2</sub>-nano transdermal penetrability showed no this nanoparticle penetration through human and porcine *stratum corneum* after 8 or 24 hours, without physical enhancement. The results were confirmed by Gamer (Gamer, 2006). These authors used 80-nm ZnO-nano and 30-60 nm long, 10 nm wide needle-like TiO<sub>2</sub>-nano, and found no penetration occurred beyond the *stratum corneum* of porcine skin. Other studies also have shown that TiO<sub>2</sub>-nano are retained on the outermost layer of human skin 6 hours after the topical application on human skin *in vivo* (Pflucker, 2001; Schulz, 2002). After physical enhancement, there was some penetration occurring of ZnO-nano in porcine skin, but not in the case of TiO<sub>2</sub>-nano. This may be due to the weak fluorescence signal of pyrene, the dye grafted onto the TiO<sub>2</sub>-nano. It might also be because of the suboptimal wavelength-selective filter settings that did not allow detecting the pyrene emission efficiently. The optimised chemistry of TiO<sub>2</sub>-nano/pyrene and/or fluorescence microscopy filter choice will improve the system sensitivity.

However, nanoparticles may fall in hair follicles. Indeed, Lademann *et al.* have suggested that hair follicle might be an alternative pathway for ZnO-nano, bypassing the *stratum corneum* (Thune, 1988; Sznitowska, 2001). Nanoparticles with the diameter of 300 to 400 nm were pushed into hair follicles by the movement of the hairs *in vivo* and stored there for 10 days (Lademann, 2006). Smaller nanoparticles (40 nm) are preferentially absorbed in the skin via

hair follicles *in vivo* and *in vitro* than 130 nm particles (Shim, 2004). Multiphoton images were also used to show ZnO-nano and 10 nm cerium oxide were retained in follicle opening and around desquaming corneocytes (Roberts, 2006).

The results for hair follicle found in top view and cross section images showed the same thing, Qdots tend to penetrate through hair shaft and located in the hair root. Similar things have been found for ZnO-nano and TiO<sub>2</sub>-nano (Nohynek, 2007). Alvarez-Roman and colleagues also have shown that 5 µm PLGA fluorescent microspheres penetrated inside hair follicles and sebaceous glands in human skin 35 minutes after application (Alvarez-Roman, 2004).

It will be interesting to know depth verse nanoparticles' sizes, where they localise in hair shaft and whether they diffuse into surrounding tissue in other circumstances. Using ICG (Indocyanine Green) as a hair follicle dye will be helpful to locate nanoparticles (Genina, 2002).

Thirdly, it has been carried the first, to the best to the knowledge, that the study of ZnO-nano penetration into human skin *in vivo*. The results showed that the ZnO-nano contained in the commercial sunscreen, topically applied to skin *in vivo* did not penetrate into the viable epidermis, as observed using the FMM. Stretching and flexing the live human skin showed little effect, if any, of the physical enhancement on the nanoparticle penetration in skin. The results are at odds with these reported by Tinkle *et al.*, who observed that 0.5 and 1-µm-diameter fluorescein isothiocyanate (FITC) conjugated dextran beads reached the epidermis after 30 minutes of the skin flexing, and the dermis – after 60 minutes (Tinkle, 2003). In the study, much smaller particles of 26 - 30 nm ZnO-nano did not penetrate through the wrist skin after 60 minutes of daily motions simulating flexing and stretching.

Fourthly, the effects of chemical enhancers on the skin penetrability have been tested, using excised skin models. The penetration of ZnO-nano was influenced by the use of four chemicals: limonene, 1, 8-cineol, menthol and 2-ethylhexyl ester. These results were consistent with the results of Haygen and Narishetty (Hayden, 2005; Narishetty and Panchagnula, 2005). It clearly showed that the ZnO-nano penetrated through skin followed the excised skin pre-treatment with chemical enhancers, such as menthol. Due to the vanishing of the skin autofluorescence, imaging configuration was preferred over the fluorescence confocal configuration, typically used in the experiments. The ZnO-nano photoluminescence excitation required high energy of the ultrashort-pulse laser source that

occasionally resulted in burning or generating bubbles in the fixed skin sample.

The confocal images for Qdots on human skin after chemical treatments showed that the penetration was the same, as in the negative controls. No Qdots were found in the deeper skin layers but just on the surface or into hair follicles. The reason can be thought of was the machine sensitivity, since for FCSM the resolution is 200 nm. Therefore, individual particles or aggregated Qdots under FCSM cannot be seen.

The cell structures in some of the *in vitro* images of skin were blurring in the experiments testing penetrability of ZnO-nano and TiO<sub>2</sub>-nano applied on skin topically. It was believed that this was due to the degraded skin autofluorescence signal. The main skin autofluorescence signal contrast is originated from the main intrinsic fluorophores, including NAD[P]H, FAD, keratin, melanin, and collagen (Palero, 2007), where the first fluorophore contributes 60% to the total autofluorescence signal of skin. When the skin sample is excised, NAD[P]H is oxidised rapidly, and is rendered non-fluorescent. FAD, the second principle fluorophore in skin undergoes similar oxidation process, resulting to quenching its flavin-mediated fluorescence properties. Therefore, it is not surprising, that the skin autofluorescence is considerably diminished after prolong treatment. The excised skin preparation takes much time. The skin samples had to be preserved in a refrigerator for several days before they are imaged. It is suggestive to perform imaging sessions as quickly as possible, several hours after excision, if the aim is to observe the skin autofluorescence.

There is ample room to improve the quality of the experimental results. In particular, the microscope settings and image processing methods are subject to further refinements. In a forthcoming research, two problems need to be solved. Other physical and chemical enhancement methods need to be tested. Also, small-size ZnO-nano (3 nm) should be tested in the future study in order to determine the skin penetrability threshold. The effects that nanoparticles can induce if they penetrate into deeper layer of human skin should be also studied.

Fifthly, SEM technique is another technique to detect nanoparticle distribution and localisation in the skin surface. The traditional way of preparing the samples is the biomicrowave protocol. However, it has many disadvantages (see Sub-Section 3.2.6). In order to solve these problems, a freeze-dry technique was used. The sample quick immersion in 2.5% glutaraldehyde was helpful to decrease artefacts associated with the chemical processing,

as e.g. in the biomicrowave protocol. Also, the sample was freeze dried by nitrogen in a very short time, around ten seconds. The water in skin tissue vaporized extremely quickly and thus left a better skin morphology and cell structure. Also, the Qdots aggregation was well controlled. In order to determine the localisation of Qdots, back scattering with EDS spectrum was used. The samples were coated with 50 nm carbon and painted with a conductive path. Therefore, the conductivity increased dramatically and thus charging was decreased. In this way, high quality SEM images were obtained and more correct judgements were made.

Although a better protocol to prepare the samples has been figured out, it still may results in some artefacts. Unwanted impurities containing silicon and iron have been observed. They are the artefacts from skin and skin cutting (the knife). Therefore, the protocol needs to be refined to remove these impurities.

The results of SEM/EDS analysis demonstrated confirmed the results of intact non-treated skin which obtained from FMM and FCSM. After skin was treated with chemical enhancers, FCSM and SEM/EDS showed different results. In FCSM, no penetration evidence was found for skin applied on Qdots with chemical treatments, which it was opposite in SEM/EDS. The Qdots were found to penetrate into the epidermis and even taken up by the cells in SEM/EDS except the carboxylic ones. However, the SEM/EDS results supported the FMM observation of the ZnO-nano penetration through *stratum corneum* on application of the chemical enhancers. One reason is that SEM/EDS had higher sensitivity than that of the FCSM. The other reason might be the Qdots leaching out of the samples prepared for the FCSM due to the specificity of the sample processing. In any case, SEM/EDS proved to be superior for detecting Qdots and ZnO-nano using fixed skin sample slices.

Finally, a brief feasibility study of application of FLIM technique to discriminate ZnO-nano on the skin autofluorescence background was carried out. ZnO-nano has a lifetime of 322 ps in a bulk state (Zhang, 2006). The lifetime is measured to range from 375 ps to 260 ps depending on the different crystal state of ZnO-nano (Brauer, 2007). The results of determination of  $\tau$  are in agreement with the previous published results. The measurement of  $\tau$  was inferior to the tabulated values due to low SNR associated with the photons counting method. A limited number of photons resulted in poor data for the lifetime curve fitting, resulting in a limited accuracy of FLIM. Increase of the FLIM integration time will ameliorate this problem, although at the expense of a longer image acquisition.

Skin has many fluorophores and mainly in epidermis they are NAD[P]H and keratin. The lifetimes of them are 0.3/2.2 ns and 1.4 ns separately. The lifetimes in the skin layers have been presented in the literature: *stratum corneum* 1.9 ns; *stratum spinosum* 2.3 ns; *stratum basale* 1.9 ns; dermis <200 ps (König, Ehlers *et al.* 2006). The results somewhat underestimate these values, and warrant further study. Also, the use of the low excitation fluorescence is preferable to avoid the possible skin photo-bleaching effects.

Only preliminary research was carried out to test the FLIM feasibility for nanoparticle penetration study. The photon counting process and lifetime exponential curve fitting need to be understood more. In later research, this technique can be a very efficient tool for nanoparticles and skin imaging.

### 3.5 Conclusion

The results of *in vivo* ZnO-nano and *in vitro* TiO<sub>2</sub>-nano, Qdots penetration through human skin, showed that the human *stratum corneum* is the main barrier of skin preventing most nanoparticles sized 15 – 40 nm from penetration into the viable epidermis. No evidence of efficiency of the physical enhancements to nanoparticle penetration was found. The ZnO-nano and Qdots turned out to be providing more sensitive nanoparticle toolkit to test the transdermal penetration of the chemically enhanced human skin. Also, comparing with the results obtained from human skin and porcine skin, it indicated that porcine skin could not be a suitable model for human skin to nanoparticle in the size range of 15 – 40 nm.

The role of the hair follicle pathway to nanoparticle penetration in skin was investigated. From the results, a conclusion can be drawn that despite localisation of nanoparticles in the hair follicle root has been observed, no spread of the nanoparticles material into the surrounding viable epidermis has been detected.

SEM/EDS imaging is an effective tool to determine the location of nanoparticles in cross section back scattering skin images. Lifetime imaging is an alternative way of direct microscope imaging. The results have shown that ZnO-nano did not appear on epidermis or in deeper skin layers.

